A&A 663, A70 (2022)
https://doi.org/10.1051/0004-6361/202141038

Astronomy & Astrophysics

Correlations of *r*-process elements in very metal-poor stars as clues to their nucleosynthesis sites

K. Farouqi[1], F.-K. Thielemann[2,3], S. Rosswog[4], and K.-L. Kratz[5,6]

[1] ZAH, Landessternwarte, University of Heidelberg, Königstuhl 12, 69117 Heidelberg, Germany
e-mail: kfarouqi@lsw.uni-heidelberg.de
[2] University of Basel, Department of Physics, Klingelbergstrasse 82, 4056 Basel, Switzerland
[3] GSI Helmholtz Center for Heavy Ion Research, Planckstraße 1, 64291 Darmstadt, Germany
[4] The Oskar Klein Centre, Department of Astronomy, Stockholm University, Stockholm, Sweden
[5] University of Mainz, Department of Chemistry, Pharmacy & Geosciences, 55126 Mainz, Germany
[6] Max-Planck Institut für Chemie (Otto-Hahn Institut), 55128 Mainz, Germany

Received 9 April 2021 / Accepted 28 January 2022

ABSTRACT

Aims. Various nucleosynthesis studies have pointed out that the *r*-process elements in very metal-poor (VMP) halo stars might have different origins. By means of familiar concepts from statistics (correlations, cluster analysis, and rank tests of elemental abundances), we look for causally correlated elemental abundance patterns and attempt to link them to astrophysical events. Some of these events produce the *r*-process elements jointly with iron, while others do not have any significant iron contribution. We try to (a) characterize these different types of events by their abundance patterns and (b) identify them among the existing set of suggested *r*-process sites.
Methods. The Pearson and Spearman correlation coefficients were used in order to investigate correlations among *r*-process elements (X,Y) as well as their relation to iron (Fe) in VMP halo stars. We gradually tracked the evolution of those coefficients in terms of the element enrichments [X/Fe] or [X/Y] and the metallicity [Fe/H]. This approach, aided by cluster analysis to find different structures of abundance patterns and rank tests to identify whether several events contributed to the observed pattern, is new and provides deeper insights into the abundances of VMP stars.
Results. In the early stage of our Galaxy, at least three *r*-process nucleosynthesis sites have been active. The first two produce and eject iron and the majority of the lighter *r*-process elements. We assign them to two different types of core-collapse events, not identical to regular core-collapse supernovae (CCSNe), which produce only light trans-Fe elements. The third category is characterized by a strong *r*-process and is responsible for the major fraction of the heavy main *r*-process elements without a significant coproduction of Fe. It does not appear to be connected to CCSNe, in fact most of the Fe found in the related *r*-process enriched stars must come from previously occurring CCSNe. The existence of actinide boost stars indicates a further division among strong *r*-process sites. We assign these two strong *r*-process sites to neutron star mergers without fast black hole formation and to events where the ejecta are dominated by black hole accretion disk outflows. Indications from the lowest-metallicity stars hint at a connection with massive single stars (collapsars) forming black holes in the early Galaxy.

Key words. nuclear reactions, nucleosynthesis, abundances – stars: abundances – supernovae: general – Galaxy: halo – methods: statistical

1. Introduction

The origin of the heavy elements beyond iron and up to the actinides is still one of the not clearly answered questions of modern physics. Since the early geochemical abundance determinations of Suess & Urey (1956), the seminal works of Burbidge et al. (1957) and Cameron (1957), and the neutron shell-structure investigations of the nuclear chemistry community (Coryell 1953, 1961), much effort has been made to understand the mechanisms and the sites that forge the chemical elements. Much progress has been made since then for the light and intermediate mass elements (e.g., Matteucci & Greggio 1986; Timmes et al. 1995; Kobayashi et al. 2006, 2020; Nomoto et al. 2013). While the pioneering papers of Burbidge et al. (1957) and Cameron (1957) laid out the underlying nuclear physics of the rapid neutron capture *r*-process responsible for the heaviest elements in the Universe, the site was still unclear. Many years of improving nuclear input, astrophysical modeling, observational efforts, and interpreting the isotopic composition of meteoritic grains followed (see e.g., Seeger et al. 1965; Hillebrandt 1978; Kratz 1988; Cowan et al. 1991, 1999, 2021; Kratz et al. 1993, 2007; Hoffman et al. 1997; Freiburghaus et al. 1999a; Pellin et al. 1999, 2006; Pfeiffer et al. 2001; Arnould et al. 2007; Möller et al. 2003; Qian & Wasserburg 2007; Farouqi et al. 2010; Roederer et al. 2010; Thielemann et al. 2011; Kratz et al. 2014; Hill et al. 2017; Ott 2017). Only in recent years have a number of concrete proposals for producing the heaviest nuclei in nature come forward. These include neutron star mergers (e.g., Freiburghaus et al. 1999b; Rosswog et al. 1999, 2018; Just et al. 2015; Bauswein et al. 2017; Thielemann et al. 2017), magneto-rotational and other jet supernovae (e.g., Winteler et al. 2012; Mösta et al. 2015, 2018; Nishimura et al. 2017; Reichert et al. 2021; Grichener et al. 2022), and collapsars (e.g., Siegel et al. 2019; Siegel 2019). The first site is related to stellar evolution (and explosions) in binary systems[1], while the latter two options are both related to the final collapse of massive stars. The original

[1] Compact binaries can also be assembled dynamically (Benacquista & Downing 2013), but recent studies (Ye et al. 2020) conclude that the contribution to the overall merger rate is very small.

idea was that regular core collapse supernovae could be responsible for a strong *r*-process, that is to say reproducing solar *r*-process abundances (e.g., Woosley et al. 1994; Takahashi et al. 1994), also up to the heaviest nuclei, within a high-entropy wind (e.g., Farouqi et al. 2010). Recent supernova simulations, however, do not support such high entropies and it seems that, if at all, supernovae could only lead to a weak *r*-process, not producing the heavy *r*-process nuclei in solar proportions (Roberts et al. 2012; Martínez-Pinedo et al. 2012, 2014; Wu et al. 2014; Mirizzi et al. 2015; Fischer et al. 2020a). Other options for a weak *r*-process include so-called electron capture (EC) supernovae (Wanajo et al. 2011) that originate from progenitor stars in the mass range from $8-10\,M_{\odot}$ (but see recent investigations arguing for their possible nonexistence, e.g., Jones et al. 2016; Kirsebom et al. 2019a). Very recently, quark-deconfinement (QD) supernovae have been suggested (Fischer et al. 2020b) as another weak *r*-process scenario.

While most of the suggested sites are based on modeling alone (possibly permitting indirect identifications in low metallicity stars), only neutron star mergers are robustly, and by direct observations of the event itself, connected to *r*-process production. The follow-up of the gravitational wave event GW170817 (Abbott et al. 2017) revealed strong electromagnetic emission in the aftermath of the merger (Kasliwal et al. 2017; Evans et al. 2017; Villar et al. 2017; Kilpatrick et al. 2017) and showed, in particular, the expected signatures of an *r*-process powered kilonova. The decay of its bolometric light curve agreed well with the expectations for radioactive heating rates from a broad range of *r*-process elements (e.g., Metzger et al. 2010; Rosswog et al. 2018; Zhu et al. 2018; Metzger 2019); therefore, there cannot be a reasonable doubt that neutron star mergers are indeed a major *r*-process source. The blue emission, which was observed after one day, points to the production of a light (lanthanide-free) *r*-process (Evans et al. 2017), while the late ($\sim$1 week) red emission is the natural expectation for heavy (lanthanides and beyond) *r*-process ejecta. This heavy *r*-process is the unavoidable result of decompressing neutron star matter from its initial, very low ($Y_{\rm e} < 0.1$) β-equilibrium electron fraction (Lattimer et al. 1977; Freiburghaus et al. 1999b; Korobkin et al. 2012) and it is also supported by observational evidence from late-time near-infrared observations (Wu et al. 2019; Kasliwal et al. 2022). The early blue emission, in turn, shows that a substantial fraction of the ejecta has been reprocessed via weak interactions to larger $Y_{\rm e}$ values, which resulted in a light, lanthanide-free *r*-process (for the variation in nucleosynthesis conditions, see e.g., Wanajo et al. 2014; Just et al. 2015; Martin et al. 2015; Wu et al. 2016; Bauswein et al. 2017; Miller et al. 2019). This is also supported by the identification of the light *r*-process element strontium (Watson et al. 2019). In summary, there is strong evidence that this neutron star merger event has produced at least a broad, and maybe the whole, *r*-process range. However, based on the observed lanthanide fraction $X_{\rm La}$, Ji et al. (2019) found that, at least for the neutron star merger GW170817, this does not represent a typical solar *r*-process pattern.

Observations of low metallicity stars indicate the existence of a weak *r*-process site (see e.g., Honda et al. 2006, 2007; Hansen et al. 2012), while most *r*-process enhanced stars show a solar *r*-process pattern (e.g., Sneden et al. 2008; Hansen et al. 2018). This goes together with a variation in the Sr/Eu ratio, for example, ranging from about 1120 down to 0.5 (Hansen et al. 2018), and indicating the different decline in the abundance curve as a function of *A*. (This led to suggestions for the contribution from different *r*-process sites, explaining abundance features of light *r*-process elements such as Sr, Y, Zr, Mo, Ru, Ag, and Pd, see e.g., Cowan et al. 1999; Kratz et al. 2007; Montes et al. 2007; Qian & Wasserburg 2007; Farouqi et al. 2009; Hansen & Primas 2011; Hansen et al. 2014a,b; Mishenina et al. 2019.) Some of the *r*-process enriched stars show an "actinide boost", that is their Th or U to Eu ratio is supersolar (e.g., Roederer et al. 2010; Holmbeck et al. 2018, 2019). If interpreted as having been born with a solar-type *r*-process pattern, their age determination would lead to absurd results (Cowan et al. 1999; Schatz et al. 2002; Hill et al. 2002, 2017; Kratz et al. 2004; Roederer et al. 2009; Hayek et al. 2009; Mashonkina et al. 2014; Holmbeck et al. 2019). Another result from the observation of low metallicity stars is that especially Eu, with reasonably easy to detect spectroscopic features, shows a large scatter in comparison to Fe, which is much larger than the alpha elements (from O to Ti) which go back to core-collapse supernova nucleosynthesis (e.g., Hansen et al. 2018). This points to the strong *r*-process being a very rare event, occurring with a frequency smaller than that of supernovae by a factor of 100 to 1000. This is also underlined by the detection and nondetection of ^{244}Pu in deep-sea sediments (e.g., Wallner et al. 2015; Hotokezaka et al. 2015).

Summarizing the discussion above: we have a number of suggested *r*-process sites, but only one of them is proven by a direct observation of the explosive event. Observations of low metallicity stars show essentially three types of patterns, a weak or limited *r*-process, a strong solar-type *r*-process, and an actinide-boosted *r*-process (in some publications, this is also referred to as a weak, main, and strong *r*-process). Whether the latter two types are produced in different sites or a result of variations within the same site (e.g., neutron star mergers) is still debated. The question is now how such observations can point back to the *r*-process sites, and whether it is possible to identify features which can provide additional insight. A promising approach is to look for correlations among different elements, which might directly identify the nucleosynthesis of a specific site (see e.g., Barklem et al. 2005; François et al. 2007; Mashonkina et al. 2007; Kratz et al. 2008). Cowan et al. (2005) compared the abundances of Fe, Ge, Zr, and *r*-process Eu in low metallicity stars. They found a strong correlation of Ge with Fe, indicating the same nucleosynthesis origin (core-collapse supernovae), a weak correlation of Zr with Fe – indicating that other sites than regular core-collapse supernovae (without or low Fe-ejection) contribute as well –, and no correlation between Eu and Fe, essentially pointing to a pure *r*-process origin with negligible Fe-ejection. More recent data from the SAGA and JINA databases (Suda et al. 2008; Abohalima & Frebel 2018) permit a correlation between Eu and Fe for [Eu/Fe] < 0.3, that is for stars with lower than average *r*-process enrichment. If interpreted in a straightforward way, this would point to a negligible Fe/Eu ratio (in comparison to solar ratios) in the major *r*-process sources, while a noticeable coproduction of Fe with Eu is possible in less strong *r*-process sources, for example with a weak *r*-process. Such cases could again be identified with the limited-r entry in observations (Hansen et al. 2018).

In the upcoming sections, we concentrate on studying correlations among different *r*-process elements, as well as the relation to Fe (a supernova product), with the aim to obtain additional indicators for the responsible *r*-process sites. In the Appendices A–C, we briefly summarize basic statistical concepts, such as the Pearson and Spearman correlation coefficients, the coefficients of determination of a linear regressions, the effects of superpositions of data sources via rank tests that we use to analyze such correlations, and tests for a clustering

of correlations. Sections 2–5 apply these tools to low metallicity star observations from light trans-Fe elements via the lanthanides to elements of the third *r*-process peak and up to actinides. In Sect. 6 we summarize these findings and attempt to link the observational features to the suggested sites via their predicted abundance features from existing models. We further use statistical tools to estimate the frequencies of these individual event sites, before presenting our conclusions in Sect. 7. Appendix D presents an analysis on how the galactic evolution of alpha elements, often addressed in chemical evolution studies, differs from the behavior of *r*-process elements in low metallicity stars.

2. Observed *r*-process abundance patterns in very metal-poor halo stars and the use of statistical methods to test for correlations

2.1. The early evolution of galaxies

Before starting to analyze abundance patterns in very low-metallicity (VMP) stars, we would like to provide a rough overview of galactic evolution, especially whether one has to look at different phases (in time and metallicity) in order to interpret observed features correctly (see Fig. 1). The production of Fe in the early Galaxy goes back to the explosions of fast evolving massive stars, dominated by core-collapse supernovae (CCSNe). Signs of Fe can be found already in the metallicity range [Fe/H] down to $-5\cdots-4$ and below. At higher metallicities, closer to -1, also explosions of thermonuclear supernovae (SNe Ia) start to contribute with a delay due to the longer evolution of low and intermediate mass stars, potentially combined with effects from mass transfer in binary systems once a white dwarf has formed (Matteucci & Greggio 1986; Dan et al. 2011, 2012; Matteucci 2012; Timmes et al. 1995; Kobayashi et al. 2006, 2020; Nomoto et al. 2013; Seitenzahl et al. 2014; Maoz et al. 2014). Many of these analyses were obtained with classical chemical evolution methods, often utilizing the instantaneous mixing approximation (IMA). In such a well mixed interstellar medium the metallicity evolution [Fe/H] is a clear function of time, that is a direct mapping between [Fe/H] and time exists. This, however, is very likely not an appropriate description in the very early evolution of galaxies when only pockets of the ISM are polluted by explosions (of possibly different types of events). The early evolution of the Galaxy has been discussed since the 1990s by a number of authors (see e.g., Audouze & Silk 1995; McWilliam et al. 1995a,b), pointing to the breakdown of the instantaneous mixing approximation IMA below [Fe/H] ≈ -2.5 when the imprint of individual explosive events can be seen.

The well established field of inhomogeneous galactic evolution simulations, developed for these very early phases, draws a clear picture how to follow the evolution of element abundances in the Galaxy (see e.g., Wehmeyer et al. 2015; Cescutti et al. 2015; van de Voort et al. 2020; Kobayashi 2016; Kobayashi et al. 2020), generalized, for example, by Ishimaru et al. (2015) and Ojima et al. (2018) for faint dwarf galaxies as building blocks of galactic evolution with varying star formation histories and outflows due to weak gravity (see for latest improvements also van de Voort et al. 2022). After a pristine gaseous medium in galaxies is inherited from the big bang, the first explosive events from stellar sources contribute in polluting the gas. This is different from simplified IMA galactic evolution approaches, that assume the immediate mixing of the ejecta with the whole galaxy. The paper by Ryan et al. (1996) suggests that a supernova blast wave mixes with the surrounding medium until the ram pressure stops the shock wave. For typical ISM densities, an explosion energy of a supernova of 1 Bethe (10^{51} erg), and 0.2 $M_\odot$ of Fe ejecta this led to [Fe/H] $= -2.7$ in the mixed supernova remnant (of about 7×10^4 $M_\odot$), for 0.1 $M_\odot$ of Fe this comes close to -3. This is the metallicity in the supernova remnant and can of course vary somewhat with the local environment conditions. Assuming that such events trigger new star formation, these newly born stars come with a pollution. The remnant value (i.e., a star born completely out of remnant matter) would be the extreme (highest) metallicity case with which the next generation of stars would be born, a 10% pollution would lead to [Fe/H] $= -4$ and a 1% pollution to -5. This general picture led to the interpretation of such low metallicity stars as pointing back to the abundance pattern of the specific event that polluted the related protostellar cloud. This is also the approach that we initially follow in our analysis, similar to many other efforts (see e.g., Norris et al. 2007, 2012; Frebel & Norris 2015; Frebel 2018; Yong et al. 2021). Of course, not only supernovae take place in galaxies, after SN explosions in a binary system neutron star mergers can occur, ejecting their *r*-process material. Montes et al. (2016) came to the conclusion that the neutron star merger ejecta are mixed with similar amounts of the ISM as in the case for CCSNe. The question which remains is whether the merger ejection takes place in the region where the previous SNe took place (i.e., inheriting already Fe from these SNe) or neutron star kicks from the SN explosion pushed the system into a pristine place (excellently analyzed by van de Voort et al. (2022); see also Fig. 23 below). Macias & Ramirez-Ruiz (2019) analyzed collapsars in this respect. There has been a debate when (in terms of metallicity) the impact of neutron star mergers shows up. In general, the above mentioned early literature for inhomogeneous galactic evolution models saw their imprint only at metallicities of about -2.5. The inclusion of faint dwarf galaxies as building blocks with varying star formation rates and outflows (of for instance Fe) in low gravity environments could also push their imprint back to about -3 (see Ishimaru et al. 2015; Ojima et al. 2018; van de Voort et al. 2022).

But to make a long story short, one will first have pockets in the ISM (involving also new star formation) polluted by specific events. If all these events would be of the same type, one would find different levels of pollution (admixtures) in newly formed stars by only one category of events with a specific abundance pattern, leading to the same element ratios in all of these pockets (within the relatively small variations for each event type). This causes strong correlations, that is linear relations between the different elements. If one has (more realistically) different types of events, there would be different "clusters" of element abundance patterns, which, however, individually could be analyzed in a similar way by correlations. This behavior will experience a transition to an averaging over all types of events when (a) the total number of all different types of events in a given region permits an overall averaging or (b) this averaging is caused by gas mixing or (c) a combination of both cases (a) and (b). In between there will be a transition region where several events contributed, but no complete mixing or averaging has taken place yet. Rank tests for the observed element abundances permit to analyze whether one or more categories of events have contributed to the individual elements.

In the case that a well mixed phase has been approached, constant ratios among element abundances, even for those stemming from different types of events, will be obtained and look like a correlation. However, these are spurious correlations which should not be confused with real correlations as found in abundances patterns originating from the coproduction of elements in one type of events. As already pointed out in the last

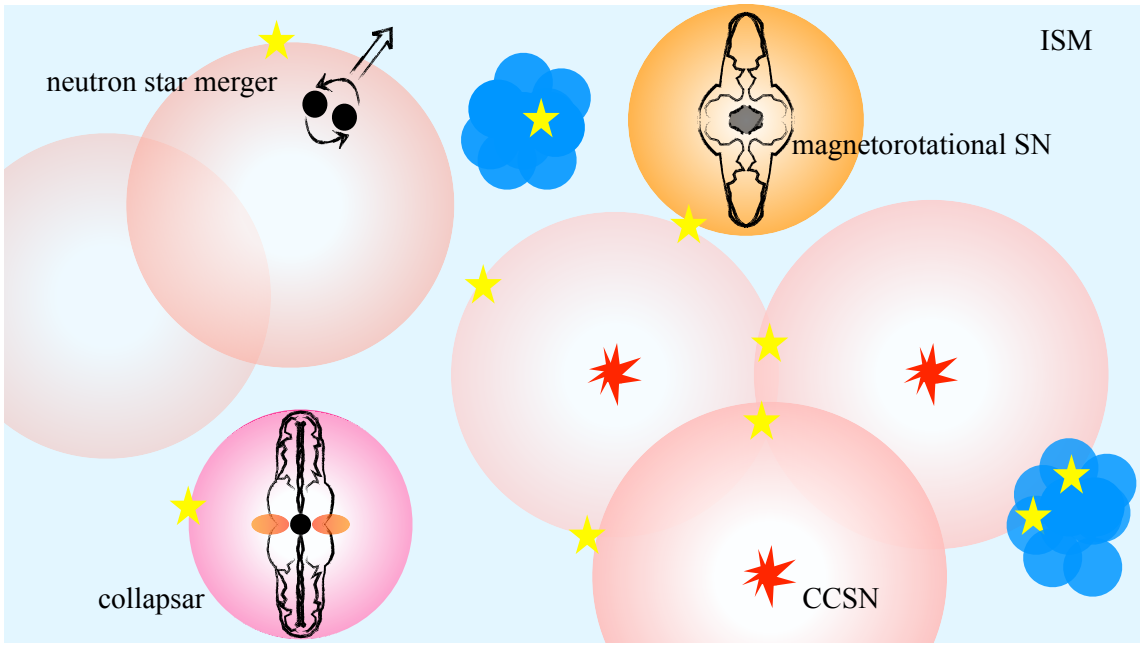

Fig. 1. Nucleosynthesis at very low metallicities. Sketch of various nucleosynthesis and potential *r*-process sources within the early galactic interstellar medium, when only a few of such events have occurred. New star formation sites, inheriting the local interstellar medium composition, which is polluted to varying degrees by the remnant sites, are displayed as yellow stars. The figure also takes into account that neutron stars, produced in CCSN explosions, are in many cases kicked out of their supernova remnants (see also our Fig. 23).

paragraph of the introduction, the Appendices A–C summarize the basic statistical concepts which we utilize with respect to correlations, cluster analysis, and rank test, to identify the behavior discussed above during different phases of galactic evolution. After we discuss the statistical analysis of many *r*-process elements up to Sect. 5, the implementation of the related findings with existing model predictions for ejecta are the focus of Sect. 6. We also present in Appendix D an analysis how the galactic evolution of alpha elements, often addressed in chemical evolution studies, differs from the behavior of *r*-process elements in low-metallicity stars.

2.2. The variety of *r*-process abundance patterns in low-metallicity stars

In this paper, we want to investigate whether and how the abundances of different elements in very metal-poor (VMP) and extremely metal-poor (EMP) halo stars can point back toward their originating astrophysical site. Here, we compare abundance patterns, similar attempts with the aim to identify key components and nucleosynthesis sites contributing to galactic evolution have been undertaken before with different methods (e.g., Ting et al. 2012). In addition, we want to use correlations between elements to interpret whether they originate from identical or different sources. But before addressing these questions with statistical methods we want to first have a look at these patterns and identify elemental features which can help in these investigations. Over the past decades, thousands of VMP (and EMP) halo stars with [Fe/H] ≤ -2 have been detected in the galactic halo and several dwarf galaxies by a number of large-scale surveys, for example, a series of papers resulting from the HK survey (Bonifacio et al. 2000; Roederer et al. 2014, and references therein), the Hamburg-ESO survey (Hill et al. 2017, and references therein), up to the *r*-process Alliance surveys (Hansen et al. 2018; Sakari et al. 2018; Ezzeddine et al. 2020; Holmbeck et al. 2020). For the further discussion it is important to consider that the so-called solar *r*-process abundances, obtained by subtracting solar *s*-process abundances from solar abundances (see e.g., Arlandini et al. 1999; Käppeler et al. 2011; Prantzos et al. 2020), might combine a number of different contributions. Especially the light trans-Fe elements such as Sr, Y, Zr, and possibly beyond seem to have also other origins aside from the typical *r*-process (Travaglio et al. 2004; Fröhlich et al. 2006; Farouqi et al. 2009; Hansen et al. 2012, 2014a; Eichler et al. 2018; Akram et al. 2020) which might be attributed to regular core-collapse supernovae. When looking at the SAGA database (only for Milky Way stars) in this metallicity window, one recognizes that one finds Fe and Sr detections in 1264 of them, but Fe and Eu detections only in 520 stars (combined with a strong scatter in the Eu abundances). While this is not a proof that Eu could not have been detected in all stars, it is an indication that an *r*-process, producing the typical *r*-process element Eu in detectable quantities, is less frequent than the majority of light trans-Fe element producing events (including Sr). However, from GW170817 we know that strong *r*-process events such as neutron star mergers produce light *r*-process elements such as Sr as well (Watson et al. 2019).

For stars with a clear *r*-process contribution the [Eu/Fe] ratio is an important indicator. Hansen et al. (2018) and Roederer et al. (2014) introduced different ranges, [Eu/Fe] < 0.3 for so-called incomplete or limited-r stars, which show apparently a weak *r*-process (we discuss this below, also whether an upper limit close to [Eu/Fe] $= 0-0.1$ is more appropriate). Furthermore so-called complete *r*-process stars (also called r-rich) with subdivisions in r-I ($0.3 <$ [Eu/Fe] < 1) and r-II ([Eu/Fe] > 1) were introduced with these different *r*-process enrichments. One very striking aspect of the incomplete stars is the nonobservation (among existing data) of the third *r*-process peak elements ($Z > 72$), including also Pb and the actinides such as Th and U. Another feature of those stars is the gradual depletion of the elements beyond Zr ($Z = 40$). The ratio of Sr and Eu in those stars is at least ten times higher than in the complete stars, whereas

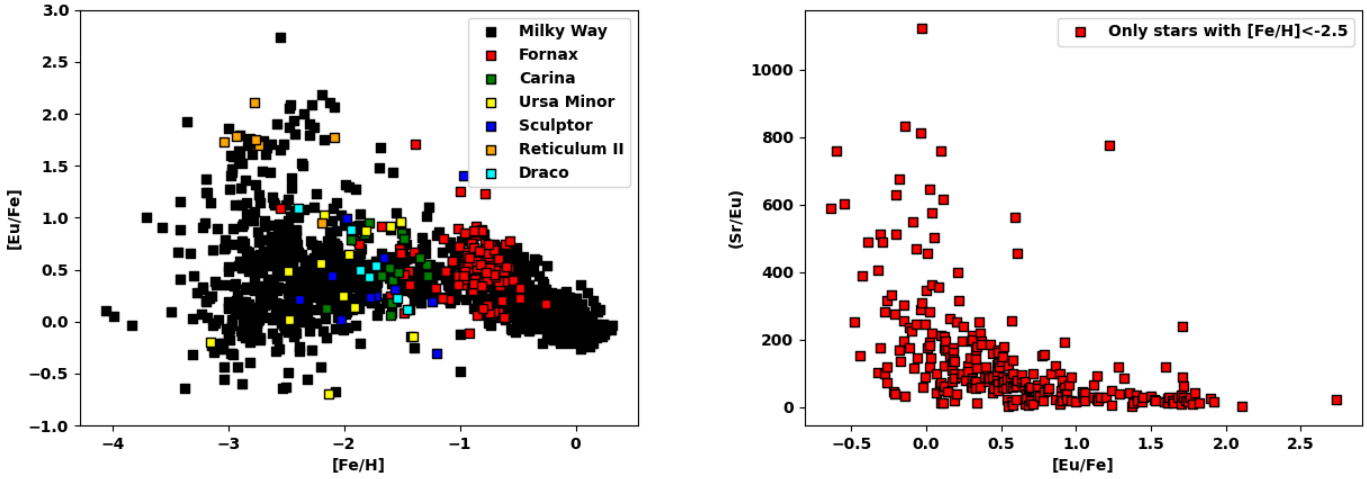

Fig. 2. Abundance ratio scatter with metallicity and *r*-process enrichment. *Left panel*: [Eu/Fe] ratios of all Milky Way and several dwarf galaxy stars with Eu detections from the SAGA Database as a function of metallicity [Fe/H]. An enormous scatter of more than two orders of magnitude exists for [Fe/H] < -2. *Right panel*: individual linear Sr/Eu ratios for all stars with [Fe/H] < -2.5 as a function of [Eu/Fe], which represents the *r*-process enrichment. A drastic reduction is seen for [Eu/Fe] $> 0-0.3$.

the ratio of Sr, Y and Zr among each other is roughly the same in both categories (Mashonkina et al. 2007; Kratz et al. 2008). This behavior will later be discussed in more detail in comparison to the complete *r*-process stars.

The whole sample of observed [Eu/Fe] values is plotted in Fig. 2 (left panel) based on the SAGA database (Suda et al. 2008). We see at low metallicities a huge scatter before at about [Fe/H] ≈ -2 an averaging over possibly many different events sets in. This has been discussed widely as an indication for a rare *r*-process site (e.g., Wehmeyer et al. 2015; Cescutti et al. 2015; Haynes & Kobayashi 2019; van de Voort et al. 2020) with a highly efficient ejection of *r*-process matter in order to reproduce in total the overall solar *r*-process abundances, which determine the product of ejected mass and event frequency (e.g., Hotokezaka et al. 2015; Rosswog et al. 2017). We see below that this argument applies surely for the strong or complete *r*-process stars (r-I and r-II), while the limited-r stars could go back to more frequent and less efficient events (for a detailed discussion of these considerations see e.g., Hansen et al. 2012; Cowan et al. 2021). However, the situation is likely more complex than just a division in limited-r and rare complete *r*-process events.

Based on the discussion in the previous subsection, in the further analysis, we concentrate on the low-metallicity stars with [Fe/H] < -2.5, with the initial hypothesis that they experienced probably only one prior *r*-process pollution. If only one event contributed to the heavy *r*-process pattern, one can thus identify correlations as coproduction of the observed elements in the same site. Whether this hypothesis can be kept throughout our analysis will be tested in a continuous fashion. What can be realized is that in addition to the observed scatter at low metallicities, there seems to exist also a change of abundance patterns as a function of [Eu/Fe], as seen in Table 1 which provides the average Sr/Eu ratio as a function of observed [Eu/Fe]. From limited-r stars to complete *r*-process stars there exists a drastic change in the Sr/Eu ratio, indicating a real change in the *r*-process strength.

This important indicator for the strength of the *r*-process is also shown in Fig. 2 (right panel) for individual stars (with metallicity [Fe/H] < -2.5). Table 1 shows a strong division between limited-r stars and complete *r*-process stars, a ratio of Sr/Eu ≥ 300 is found in stars with [Eu/Fe] up to $0-0.1$, a ratio >150 up to 0.3 (coinciding with early definitions of the above mentioned division between limited-r and r-I stars), a ratio of >100 up to 0.6, and a ratio >60 up to 0.8 (close to the previously mentioned division between r-I and r-II-stars). These changes in Sr/Eu as a function of [Eu/Fe] (but also for Y, Zr, and with some indications also for Pd and Ag) have been reported previously in Montes et al. (2007). The linear scale of Fig. 2, right panel, shows a decline by almost three orders of magnitude. Given this strong change of Sr/Eu from limited-r to complete *r*-process stars and the additional fact that in the limited-r stars no elements from the third *r*-process peak as well as no actinides have been detected, that is to say, if existing, their abundances are below the detection limit, this underlines that the weak *r*-process pattern requires different processing conditions. This argues for a different stellar site in comparison to the pattern in complete *r*-process stars. We return to the issue later as to why an apparently continuous decline across limited-r, r-I, and r-II stars, if plotted as an logarithm of [Sr/Eu], is found in Montes et al. (2007). That for the lowest metallicities in Fig. 2 (left panel) one finds low [Eu/Fe] < 0.1, that is weak *r*-process stars could also indicate that these events might already occur earlier or more frequently in galactic evolution. When taking a careful look at

Table 1. Trend of Sr/Eu with *r*-process enrichment [Eu/Fe].

[Eu/Fe] from	-Range to	#Stars	Mean (Sr/Eu)
−0.64	−0.44	4	550
−0.43	−0.23	13	291
−0.22	−0.02	24	331
−0.01	0.19	45	212
0.20	0.40	34	144
0.41	0.61	42	114
0.62	0.82	28	124
0.83	1.03	18	59
1.04	1.24	17	79
1.25	1.45	10	40
1.46	1.66	11	29
1.67	1.92	11	34

Notes. Available star data from the SAGA database in selected [Eu/Fe]-ranges and their mean of the corresponding (Sr/Eu)-ratios.

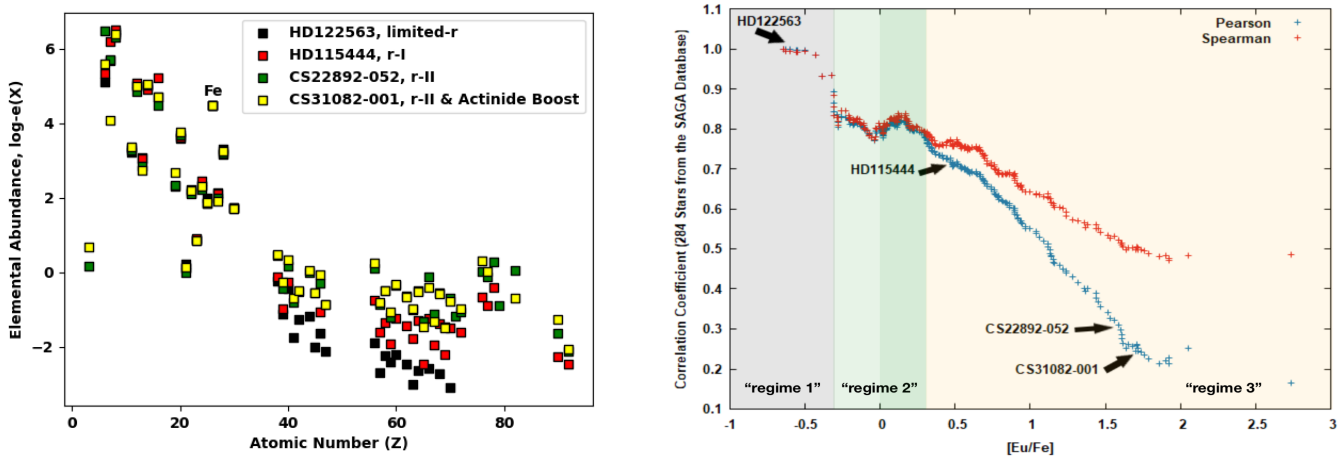

Fig. 3. Comparison of different star types and correlation methods. *Left panel*: abundances of the four standard stars: HD 122563 ([Eu/Fe] ≃ −0.64), HD 11544 ([Eu/Fe] ≃ 0.68), CS22892−052 ([Eu/Fe] ≃ 1.53) and CS31082−001 ([Eu/Fe] ≃ 1.62), from the JINA database and normalized to the absolute abundance of Fe from CS22892−052. logϵ of element X is defined via its ratio with respect to the hydrogen abundance (log ϵ(X) = log(N_X/N_H) + 12). *Right panel*: Pearson and Spearman correlation coefficients of Fe and Eu in stars with [Fe/H] < −2.5 as a function of the upper limit for the [Eu/Fe] interval utilized. At [Eu/Fe] ≃ 0.3 the Pearson and Spearman coefficients start diverging from each other. The position of the four typical stars HD 122563, HD 115444, CS22892−052 and CS31082−001 are indicated.

Fig. 2 (right panel) even two subgroups of limited-r stars could possibly be identified. For the complete *r*-process stars only a gradual decline can be observed. It indicates a continuous, but not that drastic, change in *r*-process strength, and whether the division in r-I and r-II stars is actually related to different sites or only a range of possible conditions in the same site seems not that clear.

Before going into further details about the variations observed in elemental *r*-process abundances in very metal-poor stars, we present an overview plot in Fig. 3 (left panel), showing the abundance pattern of four typical stars: an incomplete (also termed r-poor or limited-r) star, and three r-enriched stars of different magnitude (with the above definitions including one r-I and two r-II stars, the second also with an actinide boost). The figure is normalized to Fe. It is interesting to see that, with the exception of the lighter elements up to N, they show a very similar abundance pattern up to Fe and Ge, before diverging strongly for the heavy elements. While the different behavior of the limited-r star in comparison to the complete stars is striking, we can also recognize variations in the *r*-process strength for the three complete *r*-process stars. In the remainder of the paper, we discuss the possible origins of the observed abundance patterns. In the following subsection, we first examine statistical correlations and concentrate on the correlations of Fe with Eu before extending this analysis across the nuclear chart.

2.3. A first look at correlations

In order to understand the difference between the variety of observed abundance patterns, we tracked the linear correlations between two arbitrarily chosen chemical elements, X and Y. Appendix A describes how to determine Pearson and Spearman correlation coefficients (PCCs and SCCs). They both range from (a) negative values (−1), over (b) 0, to (c) positive values (+1). Case (a) describes a strong anticorrelation, that is, decreasing values combined with increasing values of either X or Y, (c) stands for a strong correlation, that is, changes with the same sign for variables X and Y, and a value of (close to) 0 indicates that there is (essentially) no correlation (case b). A PCC tests a linear relationship of both elements, that is, a positive value indicates that a straight line with positive slope can be plotted through the data points. A negative value indicates a negative slope. A small absolute value indicates a large scatter of the data points around this straight line, an absolute value of 1 indicates that all data points are located on this line, that is, a perfect linear relationship. This means that for +1 the ratio for the two element abundances X and Y is constant, arguing for the pollution by a nucleosynthesis site with these fixed abundance ratios. An overall variation, scaling X and Y, however keeping the same ratio, would just indicate a different amount of pollution by that specific site. The SCC tests only if there is a monotonic change (increase or decrease) among both elements, which does not have to be linear. It is also based on ranks (the integer numbers in the sequence of increasing values), which judges absolute distances of a data point from a fit in a milder fashion. Therefore, SCCs appear typically to indicate a better correlation than PCCs. Such correlation tests can provide a deeper insight, in general or within selected metallicity ranges [Fe/H] or element enrichment intervals [X/Fe], if one wants to analyze, for example, the relation of element X with Fe at different metallicities. For the reasons discussed in Sect. 2.1 it is most helpful to analyze such correlations at very low metallicities, where we expect that the nucleosynthesis additions to protostellar clouds, out of which the next stellar generation is born, go only back to one or very few events. As an example we choose Fe and Eu and calculate the PCCs for different [Fe/H] and [Eu/Fe] ranges. Selected results are given in Tables 2–4 (see also Fig. 3, right panel), which also indicate the strengths and weaknesses of utilizing correlations and how to apply them intelligently.

In Table 2 we analyze the (Pearson) correlation between Fe and Eu for all stars with low metallicities ([Fe/H] < −2.5), dependent on intervals of [Eu/Fe] bounded by a given upper value but open to low values. It seems that we first see a very high correlation which decreases continuously down to a value of 0.14, that is, a very weak or negligible (or essentially no) correlation. This behavior can be easily explained. If we have a look at Fig. 2 (left panel) one can see that choosing initially quite low upper limits for the [Eu/Fe] interval means that only a small range of Eu/Fe ratios is considered, as there exist essentially no stars with [Eu/Fe] < −0.65. This results in a narrow range of Eu/Fe ratios

Table 2. Trend of Pearson correlation coefficients with *r*-process enrichment.

[Eu/Fe] <	PCC	Assoc. strength	#Stars
−0.50	0.99	Very strong	7
0.00	0.88	Very strong	52
0.30	0.81	Strong	116
1.00	0.55	Moderate	230
1.50	0.35	Weak	258
2.70	0.14	Very weak	282

Notes. Selected PCCs for Fe and Eu in different [Eu/Fe] ranges for stars with [Fe/H] < −2.5.

Table 3. Trend of Pearson correlation coefficients within given star regimes.

Star type	PCC	Assoc. strength	#Stars
lim.-r [Eu/Fe] < 0.0	0.88	Very strong	52
lim.-r [Eu/Fe] < 0.3	0.81	Very strong	116
r-I	0.65	Moderate	115
r-II	0.34	Weak	51
r-I & r-II	0.15	Very weak	166
All stars	0.14	Very weak	282

Notes. Selected PCCs for Fe and Eu in different [Eu/Fe] ranges for stars with [Fe/H] < 2.5.

for stars in this selected [Eu/Fe] interval and therefore an almost linear relationship between these two elemental abundances. If one increases the upper [Eu/Fe]-limit, the interval considered becomes continuously larger, up to the point where the full scatter of more than three orders of magnitude is covered (for the same [Fe/H]-range <−2.5). This means that essentially no correlation is found, consistent with the old finding that Eu and Fe are not correlated and the main *r*-process site produces *r*-process elements efficiently but no or only negligible amounts of Fe.

Only if we have a reasonable argument that different subgroups can be considered separately could we treat these individually. This is, for example, the case for limited-r stars ([Eu/Fe] < 0) with the very high and quite different Sr/Eu ratios as well as nondetected third *r*-process peak elements. This behavior points to a distinct astrophysical site and we can analyze their Eu and Fe correlations separately. Table 3 indicates a strong correlation of Eu and Fe, that is, a coproduction of Eu and Fe in limited-r stars (and when considering Fig. 2, right panel, one can even argue for a subdivision among stars below and above [Eu/Fe] = −0.3). We also provide correlation values for the [Eu/Fe]-intervals of r-I, r-II, and r-I & r-II stars. However, beyond the kind of schematic interval division for r-I, r-II stars, it is not yet clear whether there exist convincing arguments that they are related to separate sites, rather than being variations of *r*-process strength in a typical strong *r*-process site. Thus, for the moment, we regard the separate table entries for r-I and r-II as not conclusive and treat the whole set of *r*-process enriched stars as a site that is essentially not correlated with Fe production.

Table 4 and also Fig. 2 (left panel) highlight a different aspect of interpreting low-metallicity star observations. The window in [Fe/H], where we can analyze the abundance patterns (and their correlations) of individual (*r*-process) polluters or nucleosynthesis sites, is probably limited to the interval <−2.8 or at most −2.5 (see our discussion of inhomogeneous galactic chemical evolution in Sect. 2.1). For larger [Fe/H] values we see the averaging contributions of many nucleosynthesis sites with a decreasing scatter of Eu/Fe, while Fe/H is enriched mainly by supernovae (early on by massive stars resulting in CCSNe, later on also by type Ia supernovae originating from binary systems). In the metallicity ranges [Fe/H] > −2, the metallicity starts to become a measure of the time over which galactic evolution has taken place. In parallel to the enhancing [Fe/H] ratios, due to supernovae contributing to galactic evolution, also *r*-process sites contribute heavy elements, for example Eu, as a function of time. In a well mixed interstellar medium, occurring after a while due to many different contributors as well as mixing mechanisms in the Galaxy, an averaged Eu/Fe ratio (with decreasing scatter) emerges, which is close to constant for metallicities ranging from [Fe/H] = −2 up to −1 (see e.g., Cowan & Thielemann 2004; Hansen et al. 2018). This constant Eu/Fe ratio is not due to coproduction in one specific site with that ratio, it is just a mean measure of what different sources contribute during galactic evolution. Therefore, Eu increases linearly with Fe (and galactic evolution time) under these circumstances, and we see an apparently stronger correlation emerging with increasing metallicity. For [Fe/H] > −1 type Ia supernovae start to contribute strongly to the Fe production (and with less coproduced alpha elements than in CCSNe). This has in chemical evolution the effect that [α/Fe] decreases by about a factor of three with increasing [Fe/H]. The same effect causes decreasing [Eu/Fe] observations in that metallicity interval. But while Eu/Fe is decreasing, because type Ia supernovae lead to a stronger Fe-production, Eu is still also increasing as a function of time or metallicity. The relation between Eu and Fe has a different gradient, but is almost perfectly linear. In principle, this different gradient in the Eu/Fe ratio above [Fe/H] = −1 would lead to a worse linear fit over the whole metallicity range [Fe/H] < 0 when data points would be equally distributed. But as can be seen from the last entry in Table 4, two thirds of the data points are located in the range −1 < [Fe/H] < 0, where a strong linear relation exists. For this reason we see also here a continuing increase in linear correlations, which are, however, spurious correlations, not indicating at all the coproduction in a specific site with a constant abundance ratio, but rather an overall constant abundance ratio averaged over many contributing sites.

Table 4. Trend of Pearson correlation coefficients within metallicity regimes.

[Fe/H] <	PCC	Assoc. strength	#Stars
−2.8	0.17	Very weak	109
−2.5	0.22	Weak	213
−2.0	0.22	Weak	362
−1.0	0.57	Moderate	552
0.0	0.84	Very strong	1549

Notes. Selected PCCs of Fe and Eu in different [Fe/H] ranges (for all [Eu/Fe]-values).

Figure 4 provides an additional examination of the [Eu/Fe] observations in terms of correlation clusters (see Appendix C), which leads to a further understanding of the results of Tables 2–4. This method includes the possibility to look at correlations as a function of [Fe/H] (as in Table 4) as well as a function of [Eu/Fe] (see Tables 2 and 3) in a combined way. It can be noticed that the 3-cluster correlation provides an identical analysis as discussed in Table 4, the 7-cluster correlation also exhibits the division into limited-r, r-I, and r-II stars, combined with showing

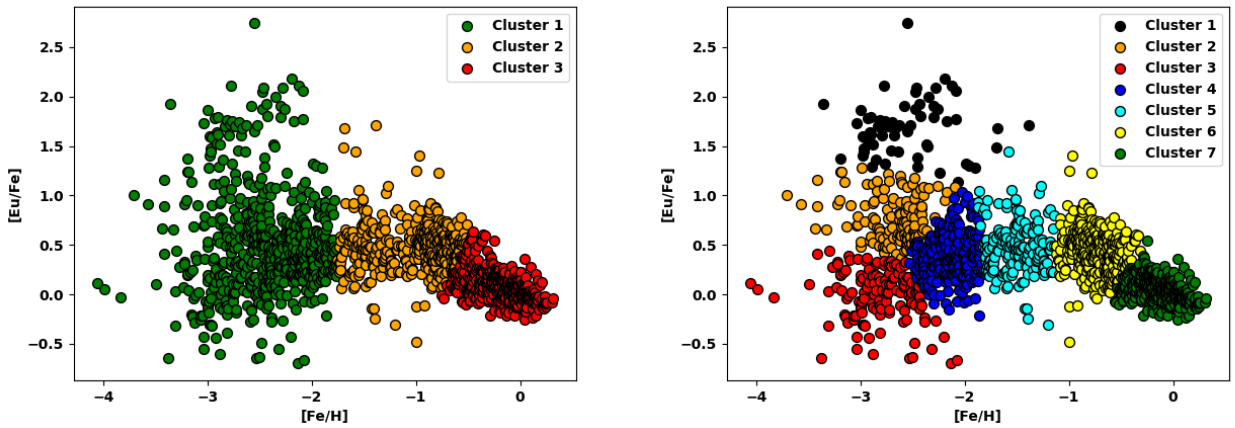

Fig. 4. Clustering of star abundances. *Left panel*: [Eu/Fe] ratios as in Fig. 2 (*left panel*), but divided into three k-means clusters, coinciding with increasing correlation strengths in Table 4 and the appearance of spurious correlations. *Right panel*: if we choose to divide into seven clusters, intermediate transition clusters appear in the interval $-2.5 < [Fe/H] < -1$, where an increasingly higher number of different r-process events tends to result in a change to an average [Eu/Fe] value, before around the kink at [Fe/H] = −1 the domination of core-collapse supernovae turns over to a type Ia supernova domination. For [Fe/H] < −2.5 we see the division in limited-r, r-I, and r-II stars, showing that they indicate different abundance behaviors.

transition regions for the values in Table 4. This supports the view that not only limited-r stars point to an independent weak r-process source, but also that r-I and r-II stars seem to point to different astrophysical origins of their abundance patterns. We discuss these issues in more detail and with more elements in the next sections. It is worth keeping in mind that a correlation does not necessarily – in general – imply causality between two entities, as was already outlined in the discussion of Table 4 and the discussion at the end of the last paragraph, when looking at Eu and Fe at higher metallicities. In a similar way Tables 2 and 3 have to be treated with care when only arbitrarily small [Eu/Fe] ranges are considered. But with additional means, such as the cluster analysis, convincing reasons can be obtained to relate them to a category of stars with pronounced features, supporting to treat them separately. While the dominant astrophysical origin of Fe is well-understood, the origin of r-process elements such as Eu is still a matter of debate. This paper attempts to bring more clarity to this issue. Table 4 and the discussion in Sect. 2.1 made clear that the method of trying to link correlations to coproduction of elements only works at lowest metallicities, where we can look at patterns originating from only one (or at most a few) site(s). With this constraint, the method outlined above clearly enables the analysis of correlated abundance patterns, pointing back to the nucleosynthesis processes of the contributing or polluting site.

3. Correlations between Fe, Ni, Eu, and Th in very metal-poor halo stars

In the following subsections, we first concentrate on the origin(s) of Fe and Eu in the observed low-metallicity stars where both elements are detected. This includes tests for correlations among these elements, before analyzing a different behavior of the Fe-group element Ni, and finally having a look at Th, a representative of the heaviest elements.

3.1. The degree of Eu correlation with Fe for the variety of limited-r, r-I as well as r-II stars

As discussed in Sect. 2, we utilize statistical correlation coefficients to understand the origin of the different observed stellar abundance patterns with known Fe and Eu abundances. The linear elemental abundances of X and Y track linear correlations such as the Pearson correlations better than $\log \epsilon(X)$ and $\log \epsilon(Y)$, because the logarithm intrinsically distorts a true linear relationship. Similar to Table 2, when analyzing correlations among Eu and Fe, we pass through the list of stars from the smallest to the largest [Eu/Fe] values, plotting the correlation values versus the upper bounds of the corresponding [Eu/Fe]-intervals (which have no lower bounds). Only stars with [Fe/H] < −2.5 are considered, in order to (a) discard the Fe originating from type Ia supernovae, to (b) avoid significant s-process contamination, and (c) preferentially select stars which, according to the utilized hypothesis outlined in Sect. 2.1, were born with the contamination from only a single (or at most very few) nucleosynthesis site(s). The abundances are taken from the Stellar Abundances for Galactic Archaeology (SAGA[2]) database compilation of stars in the Milky Way (Suda et al. 2008) or JINAbase[3] of the Joint Institute for Nuclear Astrophysics (Abohalima & Frebel 2018). In each plot, wherever possible, we indicate the positions of the following standard incomplete and complete stars (HD 122563, HD 115444, CS22892−052, and CS31082−001). These were already shown with their abundance patterns in Fig. 3 and cover the range from limited-r to r-enriched stars, via the r-I and r-II ranges, up to an actinide boost.

The SAGA as well as JINA database contain more than 200 stars with [Fe/H] < −2.5 where Eu has been measured (avoiding cases where only upper limits are given). Figure 3 (right panel) shows the PCC and SCC curves for the correlation of the elements Fe and Eu in those stars, being equivalent to the entries in Table 2, which, however, contained only the Pearson correlation. As discussed already before, the correlation coefficients obtained in such a way can include the danger of misinterpretations, because starting with small [Eu/Fe]-intervals (resulting therefore in a close to constant Eu/Fe ratio) leads naturally to high linear correlations, while utilizing the whole [Eu/Fe] range points clearly to vanishing correlations. Only clear knowledge that a certain subgroup, such as the limited-r stars with their high Sr/Eu ratios (see Fig. 2, right panel) must have a different stellar origin than complete r-process stars, permits one to employ

[2] http://sagadatabase.jp
[3] http://jinabase.pythonanywhere.com

Table 5. Regression analysis of star data.

Regime	Fe_{max}/Fe_{min}	Eu_{max}/Eu_{min}	$(Eu/Fe)_{min}$	$(Eu/Fe)_{max}$	Growth rate	r^2	# of stars
1	18	13	2.4×10^{-8}	5.01×10^{-8}	2.1	96%	9
2	36	46	5.1×10^{-8}	2×10^{-7}	3.9	70%	107
3	16	240	2.1×10^{-7}	1.4×10^{-5}	65	3%	170

Notes. Linear ratios, the growth rates, and the coefficients of determination (r^2) of the linear regression of Eu and Fe within the three regimes defined above.

a PCC analysis in the corresponding [Eu/Fe]-interval. Having this precaution in mind, we utilize this method also for detecting groupings or clusters among the higher [Eu/Fe] values. For low, but increasing, [Eu/Fe]-values the correlation coefficients remain initially at a high level in the limited-r stars regime. In fact, we see very high PCCs (≃0.98) until [Eu/Fe] ≃ −0.32. This regime corresponds to the first subgroup already noticed in Fig. 2 (right panel) with high Sr/Eu abundance ratios, and the relation between Fe and Eu is still almost perfectly linear. Both curves (PCCs and SCCs) are essentially identical and remain approximately also constant at a high level close to 0.8 for the second subgroup up to [Eu/Fe] = 0.0 (or even 0.3), with a slight change in the trend around [Eu/Fe] = 0. However, beyond that limit they start to diverge. Both coefficients show clearly that the correlation between Fe and Eu decreases with increasing upper [Eu/Fe] limits. Thus, generally three distinct regimes can be deduced from Fig. 3 (right panel):

- The first regime with [Eu/Fe] ≤ −0.32 exhibits a constant high correlation at roughly 1.
- The second regime with [Eu/Fe] between −0.3 and 0.3 (with slight change in slope around 0) exhibits also a relatively constant and still quite high correlation at roughly 0.80. In regime 1 and regime 2 PCCs and SCCs coincide very well with each other.
- The third regime with [Eu/Fe] > 0.3 is characterized by steadily decreasing and diverging PCC and SCC values.

For all stars in the limited-r regime (i.e., for regimes 1 and 2) Eu is increasing in a linear fashion with increasing Fe, while for the complete stars Eu becomes (with strongly decreasing correlations) not related to the Fe abundance, that is to say for that regime 3 Eu and Fe seem to come from different sources which both contributed already at these low metallicites of [Fe/H] < −2.5. We want to address in more detail this striking decrease of the PCC curve in the third regime at [Eu/Fe] ≥ 0.3. In order to better understand the strong decrease of the (linear correlations measuring) PCCs in the third regime, we show in Table 5 the ratios of maximum and minimum values within the boundaries of the three regimes in [Eu/Fe], that is, Fe_{max} and Fe_{min}, Eu_{max} and Eu_{min}, the minimum and maximum of (Eu/Fe), the growth rates, and the coefficients of determination (r^2, the square of of the PCCs) of the linear regression (see Appendix A.2 for a brief summary) for both elements within the three regimes defined above.

The growth rate stands for the ratio of the maximum and minimum value of the ratio of Eu and Fe, and r^2 quantifies the quality of the linear fit of Eu as a function of Fe. It can also be explained as the proportion of the variation of Eu that can be explained by the variation of Fe in %. While in the first and second regime (containing limited-r stars) the growth rate is moderate with factors of 2.1 and 3.9 respectively (i.e., changing the linear slope only slightly), it is very pronounced in the third regime and forces the correlation coefficients to dramatically fall from 0.8 to below 0.2. The corresponding r^2 is only 3%, which means that the relationship of both elements in that regime is barely linear. Furthermore, the ratio of Eu_{max} and Eu_{min} is more than one order of magnitude higher than in the first two regimes, whereas that of Fe_{max} and Fe_{min} is similar throughout the three regimes. In summary, while for the limited-r stars of regimes 1 and 2 a high correlation between Eu and Fe exists, pointing to a coproduction of both elements in the same event with a close to constant ratio, it seems that an additional and very productive source of Eu is contributing in the third regime, which produces huge amounts of Eu and negligible amounts of Fe.

3.2. A correlation test related to Fe and Ni abundances for all limited-r, r-I, and r-II stars

Similar to our analysis of Fe and Eu abundances we have also calculated the PCC and SCC curves of Fe and Ni, with the result shown in Fig. 5 (left panel). The relationship of Fe and Ni is very different from that of Fe and Eu. Firstly, both correlation coefficients remain at a high level (≥0.8), and secondly the divergence of PCCs and SCCs for higher [Ni/Fe] values is very small in comparison to the case of Fe and Eu. The linear relationship of Fe and Ni is quite strong for all (i.e., the incomplete as well as the complete) stars. Thus, for all stars at these low metallicities we find in the SAGA Database an average [Ni/Fe] ratio of 0 (with a scatter of up to a factor of three in comparison to three orders of magnitude in [Eu/Fe]). This means that Ni increases close to linearly with Fe. This different behavior of Eu/Fe versus Ni/Fe requires an understanding.

The ratio Ni/Fe, displayed in Fig. 5 (right panel), shows a variation or scatter of about a factor of three around the solar value. This means that it does not reflect a perfectly linear relation with a constant ratio (as also indicated by the PCC of 0.8 over the whole range). But for both elements we expect at low metallicities a dominant origin from explosive Si-burning in core-collapse events, while for the high Eu/Fe values one requires additional highly productive *r*-process sources with no or negligible Fe production. This is underlined by the *k*-means three cluster plot, which realizes for stars with [Fe/H] < −2.5 three clusters within the observed [Eu/Fe] variations, limited-r, r-I, and r-II stars, similar to the 7-cluster analysis of Fig. 4 (right panel) for the same metallicity range. This points once more to different sites for Eu production, while the observed variations in Ni/Fe for all these clusters need to be explained by variations in the ejecta of core-collapse events of a similar nature. Based on recent predictions by Curtis et al. (2019) and Ebinger et al. (2020) (see their Fig. 9), for example, we expect such variations within a factor of 2.65 around the solar value for CCSNe, if we take into account that elemental Fe is essentially determined by ^{56}Fe (decay product of ^{56}Ni) and Ni is dominated by ^{58}Ni. The amount of ^{56}Ni varies directly with the supernovae

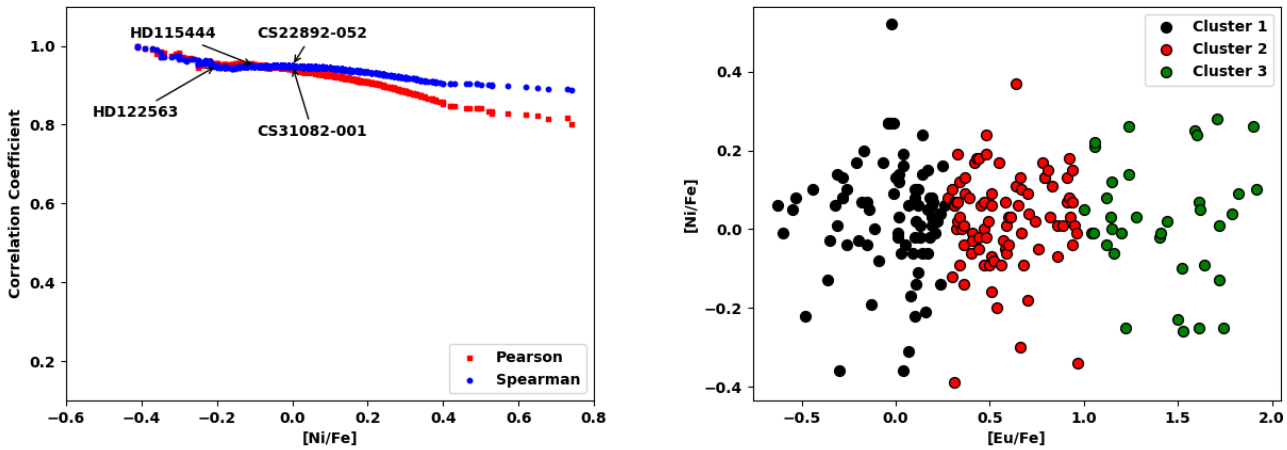

Fig. 5. Correlation methods against clustering. *Left panel*: PCCs and SCCs of Fe and Ni in stars with [Fe/H] < −2.5. We see a high correlation for the whole Ni/Fe range, including limited-r as well a r-I and r-II stars, as indicated by the four sample stars. *Right panel*: Eu/Fe, ranging over three orders of magnitude for all Milky Way stars with [Fe/H] < −2.5. While we see the [Eu/Fe] values grouped in three clusters in a (*k*-means) three cluster plot, divided in limited-r stars, r-I, and r-II stars, the Ni/Fe ratios display no correlation with [Eu/Fe].

explosion energy. The whole Fe-group, that is, also stable Ni isotopes, should vary in sync with the explosion energy and therefore also with ^{56}Ni, causing a correlation between Ni and Fe. However, ^{58}Ni shows a slightly erratic behavior and is also varying with the metallicity of the progenitor and might also reflect slightly varying Y_e values, due to weak interaction in the innermost ejecta. Thus, overall we expect the observed variation of Ni/Fe as a result of the range of possible core-collapse progenitors with varying initial mass (which determines the explosion mechanism) and metallicity. The relatively high values of the PCCs and SCCs across the observed [Ni/Fe] range, underline that for all stars a close to linear relation exists between the Ni and Fe abundances, which is, however, not perfect, as the production sites (core-collapse events) come with (although relatively small) variations in the Ni/Fe ratio.

3.3. Strong and weak Eu contributions

The left panel of Fig. 6 shows the behavior of the Fe abundance, when being plotted against [Eu/Fe]. The Fe abundances come with a scatter between 10 and 100, apparently due to the linear scatter in Fe/H for the observed stars in the metallicity range −4 < [Fe/H] < −2.5. They do not show a measurable trend with [Eu/Fe], being almost equally distributed throughout the three regimes or equivalently limited-r, r-I, and r-II stars. Thus, the abundance scatter in Fe covers the metallicity range of the sample stars, while the large variations in [Eu/Fe] exist for all values of the Fe abundance in the still quite inhomogeneous early galactic environment at low metallicities.

The right panel of Fig. 6 shows the behavior of the Eu abundances when being plotted against [Eu/Fe] (see also Fig. 2, left panel). The Eu abundances exhibit an increasing trend with [Eu/Fe], especially strong for the third regime. While for the first and second regime we notice a small, but varying Eu abundance, Eu increases very strongly as a function of [Eu/Fe] in the third regime. This indicates a strong Eu source with a negligible correlation of Eu and Fe in this regime (see the discussion related to Fig. 3, right panel). The scatter at each [Eu/Fe] value is partially due to the fact that we look at all stars with metallicities smaller than −2.5. If Fe abundances change independently of Eu in the interval −3.5 < [Fe/H] < −2.5, this would already explain up to a factor of 10 for a constant [Eu/Fe]-ratio, but in addition Eu from the independent strong *r*-process source causes strong variations, dependent on the level of mixed in contributions from the related production sites and their relative locations with respect to the stellar progenitor clouds.

So far we found a remarkable decrease of the correlation coefficients for Eu and Fe in regime 3 (r-enriched stars with [Eu/Fe] > 0−0.3, as shown in Fig. 3, right panel), consistent with the overall r-I & r-II entry for regime 3 in Table 3. This can be attributed to a very productive Eu source, producing itself no significant amounts of Fe. In order to support this claim of an additional strong Eu source, we plot the observed Eu abundances versus their corresponding rank, see Appendix B. This tool provides the opportunity to analyze abundance patterns also for stars which have, even at low metallicities, already experienced the pollution from different nucleosynthesis events. As discussed in the appendix, a linear relationship between an abundance X and its rank means, that the production of X is uniform and happens in the same manner by a single type of astrophysical source. If this uniformity is disturbed by a superposition of another source, the linear relationship between the abundances and their ranks are destroyed. This behavior is shown in its generality in Fig. B.1 for a superposition of two random variables. Figure 7 (left panel) displays such a plot of the Eu abundance versus its rank, providing with the strong nonlinear trend for high ranks a further indication for an additional contribution from a strong Eu source in regime 3, that is, for [Eu/Fe] > 0−0.3, after an initial close to linear relation for small ranks points to a single weak *r*-process source.

Opposite to the behavior of Eu versus its rank, Fig. 7 (right panel) gives an almost linear relation between the observed Fe abundances and their ranks, supporting a dominating unique source of Fe, supposedly related to core-collapse supernovae. The small offset, visible at low ranks, could suggest a superposition of another Fe source, contributing only insignificant amounts of Fe (possibly magneto-rotational supernovae). The deviation at high ranks could point to an additional source with higher Fe production than in regular CCSNe (possibly hypernovae). In general, these rank tests provide an additional unique tool to investigate whether several types of events have already contributed also at the lowest metallicities. This could include the fact, as mentioned in Sect. 2.1, that several pockets of different abundance patterns exist, still all of them due to only one

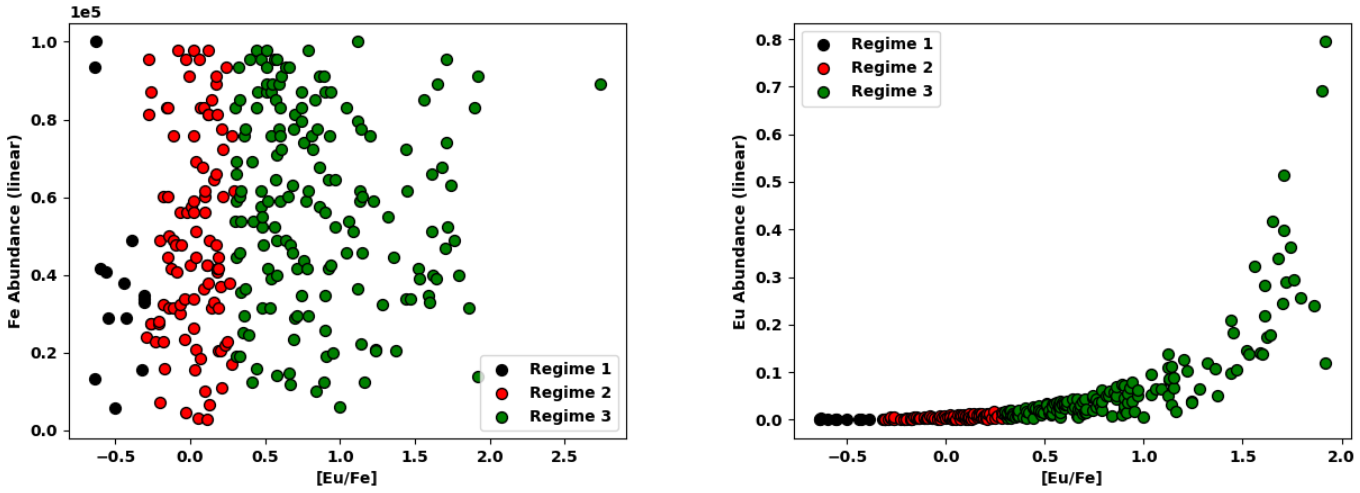

Fig. 6. Fe and Eu abundance trends with *r*-process enrichment. *Left panel*: linear Fe abundance versus [Eu/Fe] in stars with [Fe/H] < −2.5. *Right panel*: linear Eu abundance versus [Eu/Fe] in the same stars. In both cases the regimes 1, 2, and 3 stand for the [Eu/Fe] ranges <−0.3, <0.3, and >0.3.

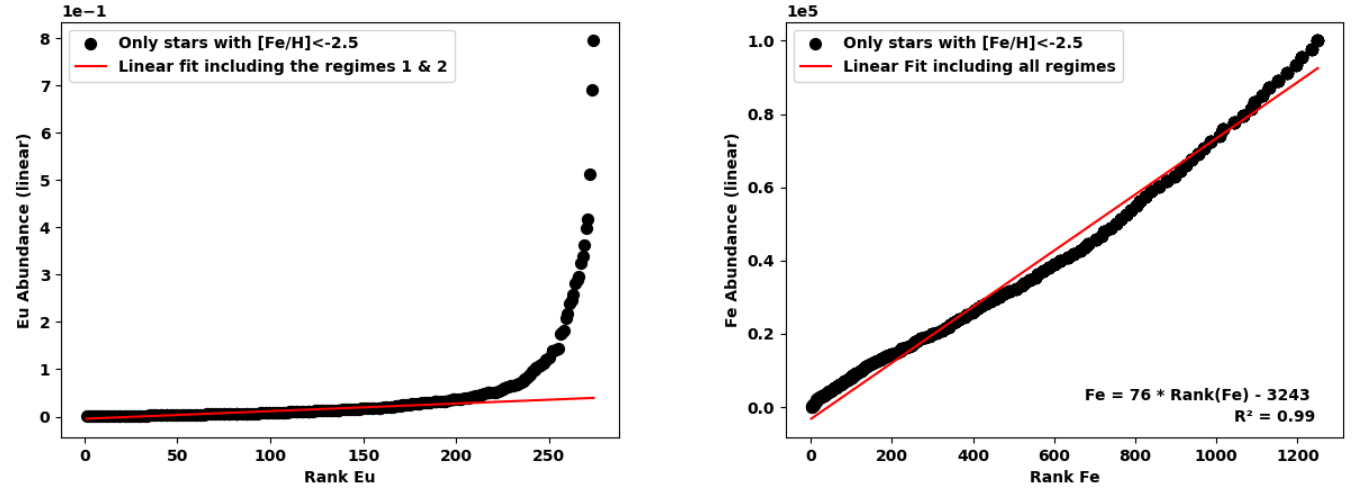

Fig. 7. Eu and Fe abundance trends with ranks. *Left panel*: Eu abundances versus their corresponding ranks. The integer rank passes, with increasing Eu abundances, through all observational points from the smallest to the highest abundance. The trend deviates strongly from a linear behavior at high Eu ranks, indicating a second highly productive Eu source. *Right panel*: Fe abundances versus their corresponding ranks (including all stars with Fe detection, independent of the fact whether they also contain Eu or not). The figure shows a close to linear relation with deviations at low and high Fe ranks.

– but possibly different – event type. But this can also cover cases where already several polluters contributed to individual stars. The different behavior of Eu and Fe, when both are already detected, seems to point to this type of scenario, and needs to be investigated further together with the possible sources characterized by the mentioned properties.

When restricting the analysis of Fig. 7 (left panel) only to regimes 1 and 2 (limited r-stars with [Eu/Fe] < 0−0.3), Fig. 8 shows initially a close to linear Eu abundance increase with its rank, but develops a slight quadratic modification. This points to similar types of Eu sources for these stars, but indicates also a superposition of two sources with similar, but slightly different, correlations between regime 1 and 2. Thus, this subsection underlined that while Fe has a dominating astrophysical source (core-collapse events, where possibly a second version – hypernovae – contributes higher Fe ejecta), Eu has clearly quite different sources. The latter is based on the fact that Fe and Eu change at highly different rates in regime 3, while in regimes 1 and 2 they change with similar but also slightly different rates.

3.4. The weak Eu contribution in limited-r stars and its origin in more than one source

The previous subsections came to the main conclusion that the complete stars (regime 3) require a highly productive Eu source with negligible Fe production, while for the limited-r stars (in regime 1 and 2) the Eu production source is correlated with Fe. However, a more detailed look showed already a slightly changing correlation behavior between regimes 1 and 2 (see also Fig. 3, right panel). This leads to the question whether limited-r stars go back to a single type of source or whether further events of a different type might contribute.

Figure 8 seemed to indicate a close to linear relation between Eu abundances and their ranks for regimes 1 and 2 (with slight quadratic modifications when extending regime 2 up to [Eu/Fe] < 0.3). This is in line with the occurrence of the two plateaus in regimes 1 and 2 as seen in Fig. 3 (right panel). Both SCC and PCC curves are identical for the two plateaus and indicate similar changing rates of Fe and Eu. The SCC and PCC

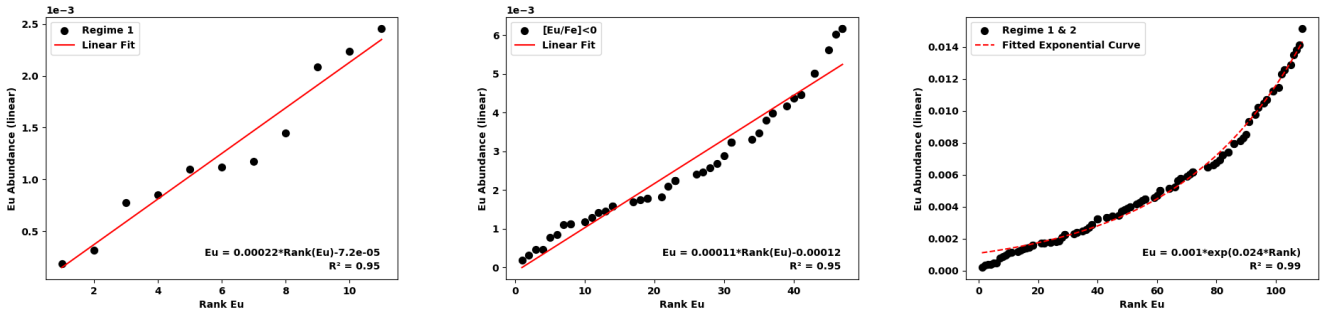

Fig. 8. Eu abundance trends with ranks for different regimes. (*a*) Eu abundances versus their corresponding ranks in regime 1, (*b*) regimes 1 and 2 with an upper limit of [Eu/Fe] < 0 and (*c*) with an upper limit of [Eu/Fe] < 0.3. The fit in (*a*) is clearly linear, in (*b*) close to linear and in (*c*) shows a nonlinear behavior.

values are roughly 1 in the first plateau and the r^2 is 96%. This means, both elements are in a virtually perfect linear relationship. As was shown in Table 5, the growth rate is about 2 and the number of the considered stars is nine. Therefore, in regime 1 the same astrophysical type of event contributes Fe and Eu with the same ratio. We refer to this source as category I in the following. In regime 2, the SCC and PCC curves are also identical and their value is about 0.8. The growth rate is about four, which is twice as high as in the first regime. Fe and Eu change at similar rates but the coproduction is not perfectly linear as shown in Fig. 8, indicating a superposition.

For this reason we plot the abundances of Eu versus Fe in Fig. 9 for the first two regimes separately (left and right panel). While stars of regime 1 are perfectly aligned, the stars of regime 2 exhibit a larger scatter, already indicated by the smaller correlation coefficients of approximately 0.8. This can be interpreted as a superposition of a second source, as suggested already above in the discussion of Fig. 8. If we also apply a linear fit, the slope of the fit in the second regime is five times higher than in the first regime, leading to the conclusion that the production of Eu is more efficient in the second regime. This suggests that we are dealing with a second astrophysical event, which similar to the first one produces Fe, but is more efficient in coproducing Eu. In the following we refer to it as a category II event.

3.5. Th, a strong *r*-process element and the question of a very early source in the galactic evolution

The production of Fe in the Universe goes back to the early evolution of galaxies via the explosion of massive stars. Signs of Fe produced by CCSNe can already be found at low metallicites, even for the [Fe/H] range below −5 to −4, possibly due to an only 1% to 10% admixture of a nearby CCSN remnant (see the discussion in Sect. 2.1). At higher metallicities, closer to −1, also thermonuclear SNe Ia start to contribute. At solar metallicity, the fraction of Fe that originated from CCSNe is estimated to be on the order of 40%.

Up to now, all detailed analyses presented in this section utilized stars in the metallicity range [Fe/H] < −2.5. Section 3.4 showed that in regime 1 and 2 (for limited-r stars) Eu is probably coproduced with Fe in core-collapse events. We have introduced them as category I and II events. However, in regime 3 (for complete *r*-process stars) a highly productive Eu source, with no or only negligible Fe production, had to be added, which we give the label of category III events. The regime 3 stars could be polluted by core-collapse events of possibly different types, producing Fe, but additionally a strong *r*-process event had to contribute as well, characterized by a negligible correlation with Fe. The question arises which one of the events discussed in the introduction is responsible, and whether they occur with a delay after the Fe-contribution from core-collapse events. A general discussion of *r*-process contributions in the early Galaxy (with extended literature) can be found in Cowan et al. (2021). The main question with respect to these sources is related to their (massive) single or binary star origin and a possible delay in their appearance as a function of metallicity. Dependent to some degree on the refinement of the method to perform inhomogeneous galactic chemical evolution simulations (see e.g., Wehmeyer et al. 2015; Cescutti et al. 2015; van de Voort et al. 2020), which does not assume immediate extended mixing of ejecta with the interstellar medium on galactic scales, it has also been discussed that a massive star related source is required in order to reproduce the very early appearance of strong *r*-process elements, while neutron star mergers (NSMs) would appear later (at metallicties [Fe/H] > −3 to −2.5). This conclusion could possibly be circumvented by the existence of extensive mixing of matter or ejecta mass lost in dwarf galaxies, if all lowest metallicity observations relate to stars which originated in these early substructures and building blocks of galactic evolution (see e.g., Ojima et al. 2018).

In order to test whether different events contributed to these regime 3 stars, that is, whether category III events relate to one or more than one site, we select the actinide element Th which can only be produced in strong *r*-process events and thus reduces uncertainties introduced by weak *r*-process components. Before discussing this further, we want to point to an interesting additional fact, related to Th observations. Limited-r stars have been initially defined as those with [Eu/Fe] < 0.3, this comes typically with a nondetection of elements of the third *r*-process peak as well as actinides. When having a look at Fig. 10 (left panel), one recognizes that Th can be observed already in stars with [Eu/Fe] > 0−0.1. Therefore an upper limit for limited-r or a lower limit for complete *r*-process stars of [Eu/Fe] ≈ 0 seems more appropriate than the up to now utilized value of 0.3.

After having identified regime 3 more clearly, that is already starting at [Eu/Fe] ≈ 0, the question to be answered is whether this strong *r*-process regime with Th production is related to one or more astrophysical sites. A superposition of sources would be indicated by a nonlinear behavior of Th abundances (taken from regime 3 observations) as a function of their rank. In Fig. 10 (right panel) we show this relation for Th and see clearly a nonlinear behavior. Thus, it is obvious that the Th observed in regime 3 stars requires a superposition of (at least) two different category III sources (category IIIa and IIIb, see below). We have neutron stars mergers as a clear candidate for a complete *r*-process, the question arises which additional

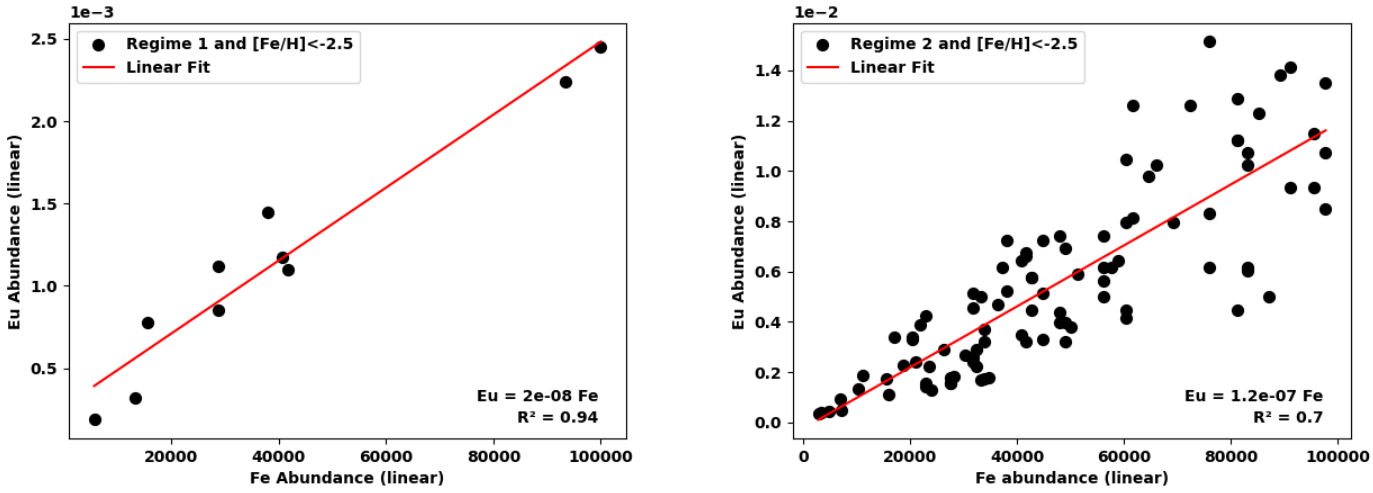

Fig. 9. Relationship of Eu and Fe. *Left panel*: linear abundance of Eu versus Fe in regime 1 ([Eu/Fe] ≤ −0.32). *Right panel*: linear abundance of Eu versus Fe in regime 2 (−0.32 < [Eu/Fe] < 0.3). Two corresponding linear fits are shown as well, with a large(r) scatter in regime 2.

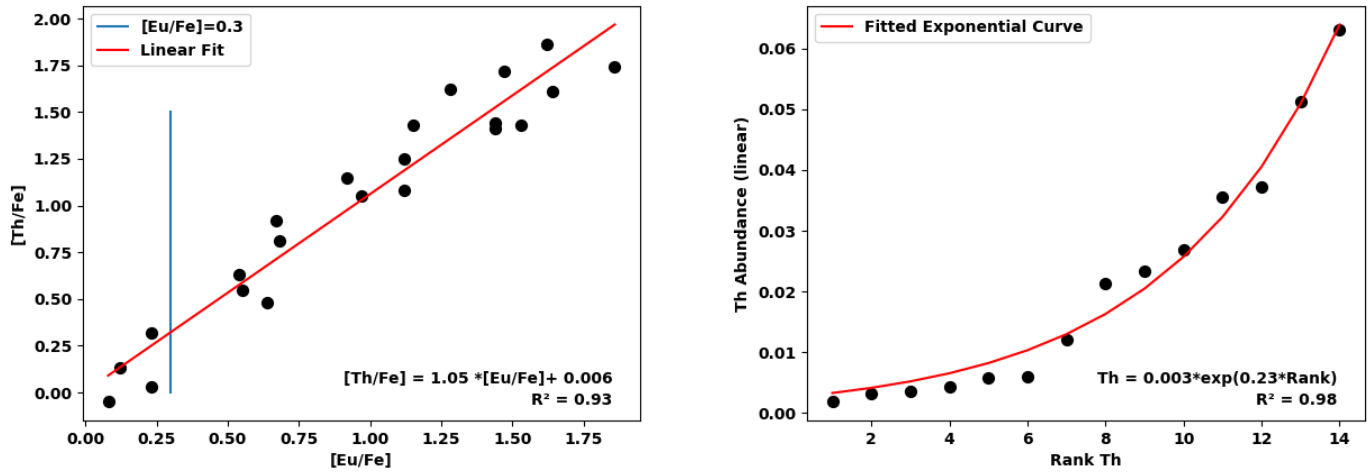

Fig. 10. Th trends with *r*-process enrichment and ranks. *Left panel*: observed [Th/Fe] as a function of [Eu/Fe] in low metallicity stars with [Fe/H] < −2.5. It can be recognized that already for [Eu/Fe] > 0 Th can be found, indicating a strong *r*-process. The blue line shows the previously utilized upper limit for limited-r or weak *r*-process stars. *Right panel*: detected Th abundances in low metallicity stars with [Fe/H] < −2.5 plotted versus their rank, showing a strongly nonlinear behavior.

site(s) could be responsible, having in mind our earlier discussion related to delays of ejecta from binary stellar systems, while those essentially vanish for collapsing massive stellar sites. In Fig. 11 we show observations of [Th/Fe] with respect to metallicity [Fe/H] (with the present-day solar Th abundance taken from Asplund et al. 2009), indicating quite a number of high values at very low metallicities around [Fe/H] = −3.

If a strong *r*-process site related to the core-collapse of massive stars can be considered (e.g., collapsars or also magnetorotational supernova, Siegel et al. 2019; Siegel 2019; Winteler et al. 2012; Mösta et al. 2015, 2018; Nishimura et al. 2017; Reichert et al. 2021), it would be accompanied by observed high [Th/Fe]-values at lowest metallicities. This behavior, shown in Fig. 11, might potentially be identified with the contribution of such a site. Although one should be careful with interpretations, this could point to one of the (possibly more than) two strong *r*-process – and therefore Th (and also Eu) – sources, this one appearing already at lowest metallicities. One option for this source would be collapsars, that is stars with masses even higher than those of regular CCSNe, which explode very early in galactic evolution (Siegel et al. 2019). For higher metallicities between [Fe/H] = −3 and −2 NSMs will set in (Wehmeyer et al. 2015; van de Voort et al. 2020). This would consistently lead to a superposition of sources with a nonlinear behavior of Th abundances as a function of their rank, as discussed above. Regime 3 (or *r*-process enriched) stars requiring a superposition of (at least) two different sources, have already been introduced above as category IIIa and IIIb. Whether there is room for another source in this superposition (e.g., magnetorotational supernovae Winteler et al. 2012; Mösta et al. 2014, 2015, 2018; Reichert et al. 2021) has to be left open at this point. In such an interpretation a subclass of category III events, contributing already at lowest metallicities and producing a strong *r*-process, would come with a not necessarily small, but negligible Fe-production in comparison to solar Eu/Fe abundance ratios. On the other hand, those events of category III which contribute with a delay are dominated by sites of a delayed stellar origin, for example probably compact binary systems, leading to NSMs and NS-BH mergers with essentially no Fe production at all. We subsequently discuss how both types of events relate to the onset of high [Eu/Fe] values in Fig. 2 (left panel).

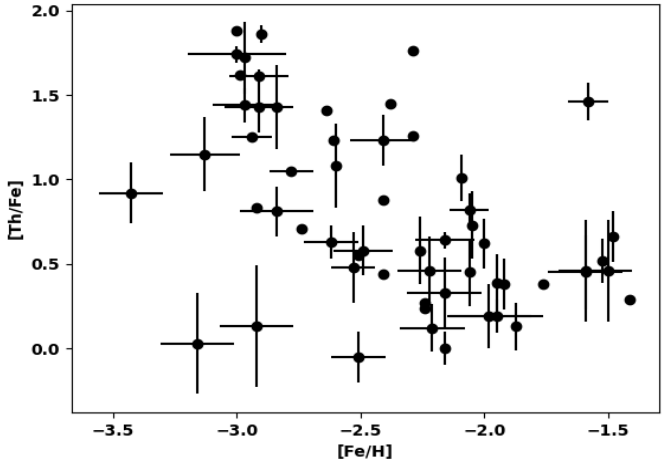

Fig. 11. Th trend with metallicity. Observed [Th/Fe] as a function of metallicity [Fe/H] from the Saga database. For the solar abundance of Th its present-day value is utilized.

Summarizing the results of Sect. 3, compared to the initial overview of chemical evolution in Sect. 2.1, we find the following situation. The initial approach started out with the ansatz that abundance patterns in low-metallicity stars with [Fe/H] < −2.5 can be interpreted as the outcome of a single contributing *r*-process source (based on the analysis of Ryan et al. 1996). This would, in the case of only one type of contributing nucleosynthesis event, lead to an overall (almost) identical abundance ratio between two elements (i.e., a perfect correlation with PCC = +1), independent of whether the total admixtures to the individual stars vary. If different types of events with different abundance patterns occurred, this would lead to separate classes of observations, that is so-called clusters. Combining all of these observations within a global data set would lead to no or only a very low correlation, but if one finds a way to separate the classes into clusters, one can see for each of them individual correlations, caused by coproduction in the events responsible for that class or cluster. In this way we could separate the Eu observations in limited-r stars, related to weak-r production sites and r-enriched stars with strong *r*-process production sites. Among the weak-r production sites we have identified two categories of events (I and II) with strong correlations between Eu and Fe, suggesting a coproduction in these events. If we have a look at the complete (r-enriched) stars, we find a very weak correlation between Eu and Fe, that is separate types of events must have contributed to these two elements and overall no or only a negligible coproduction of Eu and Fe seems to have occurred. Because we find Fe in all these observations, indicating its origin from a different site than that for most of the Eu, points to regular core-collapse supernovae as the likely site. This leads to the complication that one is already at the stage in galactic evolution where not only one single event is responsible for the abundance observations in a low-metallicity star, but at least two or several events contributed already. This can in principle weaken the interpretation of coproduction to explain all elements in such low-metallicity stars by the imprint of a single nucleosynthesis source. Nevertheless, detecting strong correlations within clusters can still give powerful hints for the analysis of a set of stellar abundance observations. Fortunately, with the rank method explained in Appendix B we found a powerful tool that has been utilized in Figs. 7 and 8. It underlines that Fe goes back to essentially one dominating origin (core-collapse events), while Eu must have several origins (related to weak and strong *r*-process sites). In Fig. 10 we could see that even the strong *r*-process element Th must have two contributing sites.

Making use of these insights we could point to the two types of category I and II events (due to the correlated Fe production, probably related to specific types of CCSNe) with different efficiencies for producing *r*-process elements such as Eu, as outlined in Sect. 3.4. The discussion related to the Th abundance led to the question whether a second category III subsource is required, which is connected to core-collapse of massive stars, and would also produce Th and U, while category III in total (IIIa and IIIb) is responsible for the complete (r-enriched) stars of regime 3 with [Eu/Fe] > 0. We later return to the question of whether the subsets of category III type events discussed above, which in total are responsible for complete *r*-process enriched stars of regime 3, also produce Th and Eu in similar or different ratios for the majority of complete *r*-process stars.

4. The Fe-group and light trans-Fe elements: Asking for a variety of core collapse events

In regime 1 and 2 we found a clear correlation between Eu and Fe, indicating a coproduction in a weak *r*-process by a specific kind of core-collapse supernovae. We also noticed before that all the stars of regime 3 contain Fe as well. Thus, the question arises whether it was produced in preceding supernovae before NSMs set in with strong *r*-process contributions, resulting this way in a small or negligible correlation to Fe. However, a further question needs to be posed, whether some of these *r*-process enriched stars also go back to sources which coproduced Fe combined with enriched Eu (in comparison to the solar Fe/Eu ratio in negligible proporation), as alluded to already in the preceding section. For this reason we revisit the correlation of Ni and Fe, shown already in Fig. 5 for metallicities [Fe/H] < −2.5, and extend this analysis also to Zn and other trans-Fe elements.

4.1. Correlations of Fe with Ni and Zn

Figure 5 showed that the Ni/Fe ratio varies for these low metallicities about a factor of three around solar ratios. The SAGA database finds a relatively stable behavior with a mean value close to solar as a function of metallicity [Fe/H]. A decline of the scatter toward higher metallicities is due to averaging out of individual contributing event characteristics and mixing of the ISM. We note that [Ni/Fe] in (simplified) spherical explosion models of CCSNe, for example by Curtis et al. (2019) and Ebinger et al. (2020), covers a range from about −0.35 to +0.4. In case there would be a superposition of CCSNe and other Fe and Ni producing sources at low metallicities, and both sources contribute Ni and Fe in (slightly) different ways, one would expect a superposition in the [Ni/Fe] range. The predicted CCSN ratios seem to be consistent with the observations within their error bars, however, a larger spread of values due to other sources cannot be excluded at this point. In the Sect. 3.2 we discussed the Fe and Ni contributions from explosive Si-burning. Fe is dominated by ^{56}Fe, a decay product of ^{56}Ni. Ni has a significant contribution from ^{58}Ni, being produced under slightly neutron-rich conditions, that is $Y_e < 0.5$, which can be due to weak interactions during core collapse or also to due metallicity (CNO turns to ^{14}N in H-burning and via two alpha-captures and one β^+-decay to slightly neutron-rich ^{22}Ne). Thus, ^{58}Ni is a measure of slightly neutron-rich conditions. ^{60}Ni, on the other hand, is a product of alpha-rich freeze-out of explosive Si-burning, a decay product of ^{60}Zn, resulting from a further alpha-capture on ^{56}Ni.

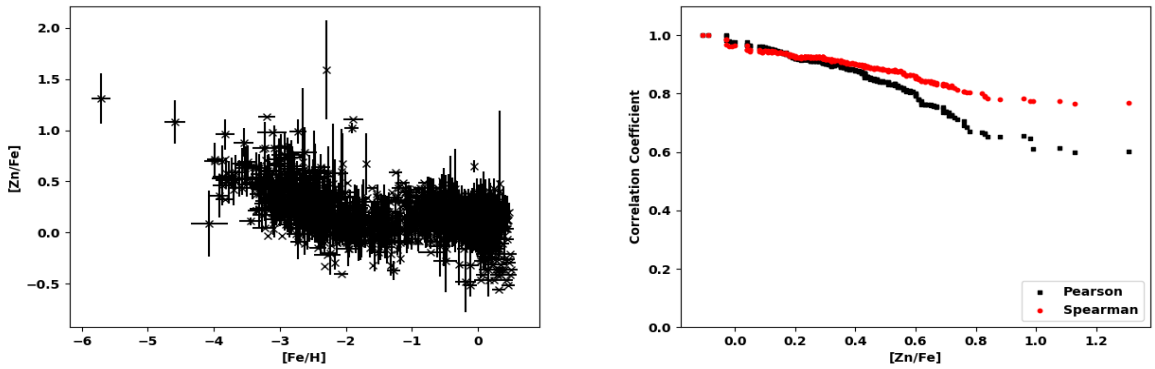

Fig. 12. Zn/Fe trend with metallicity and correlations. *Left panel*: [Zn/Fe] as a function of metallicity [Fe/H] for Milky Way stars from the SAGA database. Below [Fe/H] = −2 an increasing trend can bee seen. *Right panel*: correlation of Zn versus Fe for stars with [Fe/H] < −2.5, showing a strongly decreasing correlation for increasing [Zn/Fe].

Therefore, larger variations of [Ni/Fe] can be due to (a) a slight neutron-richness, and (b) higher entropy explosions, leading to a stronger alpha-rich freeze-out. While probably (a) dominates for regular CCSNe, not leading to too extreme [Ni/Fe]-values, hypernovae and collapsars experience the conditions related to (b) and could be responsible for the highest [Ni/Fe] observations. Such conclusions could be underlined if one sees an accompanying Zn/Fe enhancement, with ^{64}Zn being the decay product of ^{64}Ge, resulting also from a very strong alpha-rich freeze-out and discussed often in galactic evolution research as going back to hypernovae and collapsars (Nomoto et al. 2006; Nomoto 2017; Kobayashi et al. 2020). For this reason we now have a look at [Zn/Fe] as a possible indication for hypernovae and collapsars, which are also considered as a strong *r*-process source (Siegel et al. 2019; Siegel 2019) at the lowest metallicities [Fe/H] < −3.

As has been discussed above, Zn (via the decay product of ^{64}Ge) provides a test for a strong alpha-rich freeze-out. The average of [Zn/Fe] observations at metallicities from [Fe/H] = 0 down to −2 are of the order 0 (i.e., solar). This is dominated by type Ia supernovae down to −1, and due to a combination from normal freeze-out of explosive Si-burning in Chandrasekhar mass explosions (e.g., Thielemann et al. 1986; Iwamoto et al. 1999; Maeda et al. 2010) and an alpha-rich freeze-out in sub-Chandrasekhar He-detonations (e.g., Seitenzahl & Townsley 2017). For an overview that a combination of both subtypes of SNe Ia is needed see, for example, Maoz et al. (2014), Goldstein & Kasen (2018), Livio & Mazzali (2018), and Seitenzahl et al. (2019). Below such metallicities the Zn/Fe ratio is determined by core-collapse events. Down to [Fe/H] = −2 to −2.5 the average [Zn/Fe] is still 0 (solar) and given by a superposition of CCSNe over the whole mass range of an initial mass function (Tsujimoto & Nishimura 2018). The average rises from [Fe/H] = −2.5 to −3 up to [Zn/Fe] = 0.5 with a large scatter and stays at that value for even lower metallicities.

In Fig. 12 (left panel) one can see that for [Fe/H] < −2.5 still [Zn/Fe] < 0 entries occur. At lower metallicities the negative values for [Zn/Fe] disappear, underlining an increasingly alpha-rich freeze-out, which could be interpreted via the fact that at such low metallicities the average mass of exploding CCSNe is shifted to more massive progenitor stars. This leads to increasing compactness and increasing explosion energies. The range of [Zn/Fe] ≈ 0.5 seems to belong to such massive CCSNe (Grimmett et al. 2020). Figure 12 (right panel) shows the Pearson and Spearman correlations of Zn and Fe, based on upper limits of the considered [Zn/Fe] intervals for all stars with [Fe/H] < −2.5. The entries including [Zn/Fe] intervals over the whole range up to values given on the abscissa lead to a divergence of PCCs and SCCs and to lower correlations above [Zn/Fe] of 0.4 to 0.5. This goes along with a larger scatter in the Zn/Fe ratios and could be interpreted as a sign of larger variations in the Zn and Fe ejecta of highest mass core-collapse sources. Tsujimoto & Nishimura (2018) interpret the rise of [Zn/Fe] being due to magneto-rotational supernovae of the type described in Nishimura et al. (2017), with varying strength of precollapse magnetic fields and rotation, while Nomoto et al. (2006), Nomoto (2017), and Grimmett et al. (2020) contribute the high levels of Zn/Fe at lowest metallicities to hypernovae and collapsars. If we follow our earlier discussion related to Th/Fe and its possible source in such events (Siegel et al. 2019; Siegel 2019), these high Zn/Fe ratios at very low metallicities would provide a connection between these abundance features of a high Zn/Fe ratio and a strong (Th and actinide producing) *r*-process.

4.2. The light trans-Fe elements, Sr, Y, Zr and correlations with Fe

Next we also analyze how the light trans-Fe elements Sr, Y, and Zr behave in this respect. It is well known that for higher metallicities, when low and intermediate mass stars started to contribute to galactic evolution, these elements are produced in an *s*-process. However, observations at low metallicities required a different source, initially dubbed the LEPP (light – heavy – element primary process, see Travaglio et al. 2004). There exist possible explanations related to core-collapse supernovae with mildly proton-rich and (or) neutron-rich conditions (Fröhlich et al. 2006; Pruet et al. 2006; Kratz et al. 2008; Farouqi et al. 2008, 2009; Roederer et al. 2010; Arcones & Montes 2011; Arcones & Thielemann 2013; Akram et al. 2020). In fact, recent core-collapse supernova investigations by Ghosh et al. (2022) find across the mass spectrum of CCSNe a superposition of *νp*-process contributions up to $A \approx 60-70$ and a (very) weak *r*-process contribution up to the second *r*-process peak at $A = 130$, but not beyond. On the other hand Sr has also recently been identified in the kilonova event following the neutron star merger GW170817 (Watson et al. 2019). Thus, probably weak and strong *r*-process (and other) sources can contribute and this will be discussed in the following, based on correlations with Fe, in a similar way as performed before in Sect. 3 and in the previous subsection.

Similar to Fig. 3 (right panel), we display in Fig. 13 the correlations of these elements with Fe as a function of [Sr/Fe] and

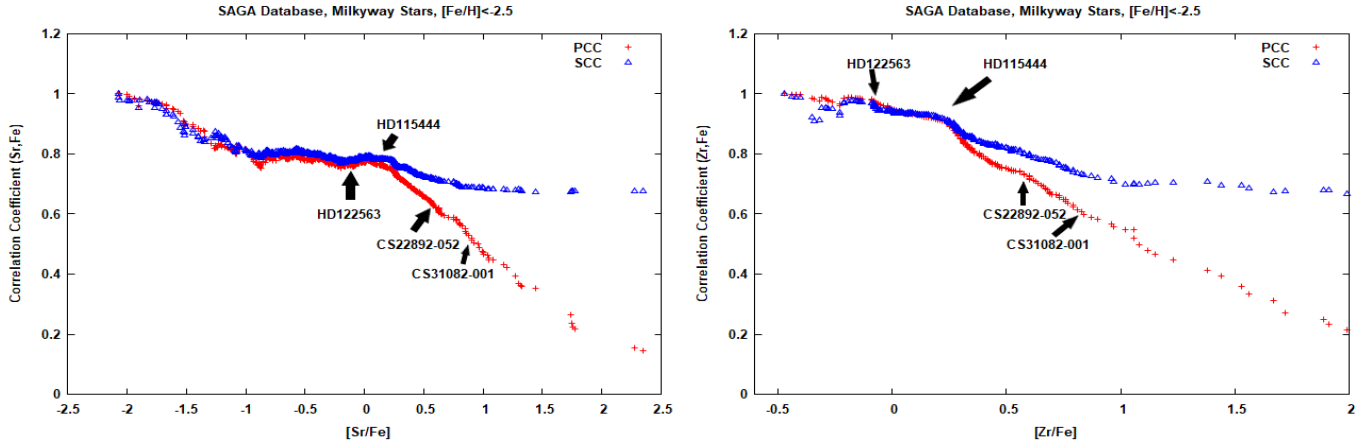

Fig. 13. Comparison of correlation methods for Sr and Zr. *Left panel*: PCCs and SCCs of Fe with Sr in stars with [Fe/H] < −2.5. *Right panel*: PCCs and SCCs of Fe with Zr in stars with [Fe/H] < −2.5. Y (not shown here) behaves in a similar way. Contrary to Fig. 3 (*right panel*) also stars with lower [Sr,Y,Zr/Fe] values than those with a weak *r*-process signature, such as HD 122563, are observed. HD 115444, CS22892−052, and CS31082−001 appear in the same order as seen in their increasing *r*-process strength.

[Zr/Fe] ([Y/Fe] behaves in a similar way). This extends our PCC and SCC analyses for these correlations, making use of exactly the same method as applied before for Fe, Eu, Ni, and Zn. As in the Fe and Eu case, we see similar (although not identical) features, starting out with two (or better three) kinds of plateaus with correlation coefficients close to 1 and 0.8, and declining correlations toward higher [Sr/Fe], [Y/Fe], and [Zr/Fe] values, combined with a divergence of the PCC and SCC curves. The PCCs go down to 0.2, that is they indicate a vanishing correlation, while the SCCs can stay as high as 0.4−0.5 for reasons we discussed earlier, based on metric or rank deviations from the relation between the abundances. At first glance it is not obvious how this behavior relates to limited or weak *r*-process stars and complete or enriched *r*-process stars, but the location of the four well-known stars HD 122563, HD 115444, CS22892−052, and CS331082−001 in these plots shows that the increase in [Sr/Fe], [Y/Fe], and [Zr/Fe] goes in parallel with the increase in [Eu/Fe]. While details might be different, the tendency is the same. However, the appearance of additional plateau phases to the left of HD 122563, which stands for an extreme limited-r star in these plots (see also Fig. 3, right panel), can be interpreted as stemming from additional sources, not related to an *r*-process producing Eu. These must be core-collapse supernova events without Eu *r*-process production, which we postulate as category 0 events. Such sources that lead to a very weak *r*-process have been discussed above, ranging from contributions of a νp-process to explosive Si-burning with moderate entropies and (or) very modest variations of Y_e around 0.5, down to 0.43. These plateaus at low [X/Fe] values could not have been noted as a function of [Eu/Fe], as such category 0 events do not produce Eu.

The low values for the Pearson and Spearman correlation coefficients, when considering the whole range of observed [Sr,Y,Zr/Fe] values and their scatter, including the higher ones shown in Fig. 13, also make it clear that they require additional rare sources of events not correlated with Fe (category III). However, the stars also in the plateaus for the lower [Sr,Y,Zr/Fe] values below HD 115444, which show a high correlation with Fe, require a superposition of different sources, as the plots of their abundances versus their ranks in Fig. 14 indicate. It can be noted that Sr shows in Fig. 13 an extension to lower [X/Fe] values and an earlier and stronger deviation from the linear fit in Fig. 14. As discussed in Appendix B, the deviation from a linear relationship points to a superposition of sources in this regime. This would be explainable with a superposition of category 0, I, and II events. We have seen such patterns also in Figs. 7 and 8 for the relation between Eu abundances versus their rank, with a strong nonlinear behavior in the first case, and a close to (with exceptions at low and high ranks) linear behavior in the second case for Fe. Thus, these limited-r or weak *r*-process regimes 1 and 2 required a superposition (of possibly two sources), as shown in Fig. 9. For Sr, Y, and Zr we come to the same conclusions, but requiring an additional category 0 source, which does not produce Eu. This leads to the conclusion that there exists a strong source (category III) with no (or a negligible correlation) to Fe, and there exist (possibly more than) three sources which are correlated with Fe (category 0, I, and II). The strengths with which these sources affect different mass ranges (i.e., trans-Fe versus Eu) seem different, but the principle effect is similar. It needs to be examined further whether the slightly stronger effect for Sr points to additional subcategories.

Similar to the last paragraph in the previous Sect. 3, one should point to more extended interpretations of correlations, even at low metallicities <−2.5. Globally among all VMP stars, one does not see only the imprint of one nucleosynthesis event, where a correlation between two elements means automatically their coproduction. We have rather seen different subclasses (clusters) of stars, where each of them still shows only the imprint of one type of nucleosynthesis event. In this case correlations, restricted only to these subclasses, can still be interpreted as coproduction. A further extension is that in certain VMP stars we see the superposition of several nucleosynthesis contributions. In that case the rank analysis for each element of interest made it possible to test whether one or several types of events contributed. We noticed that this is the case for Sr, Y, Zr, Eu, and Th (and possibly even for Fe, when considering the lowest and highest ranks, i.e., very small as well as large Fe contributions). For Th we came to the conclusion that two types of events had to exist among regime 3 (*r*-process enriched) stars (category IIIa and b), for Eu we noticed three types of events, category I and II for limited-r stars and category III for *r*-process enriched stars. Now for Sr, Y, Zr we noticed four types of events, category III for *r*-process enriched stars, category I and II for limited r-stars,

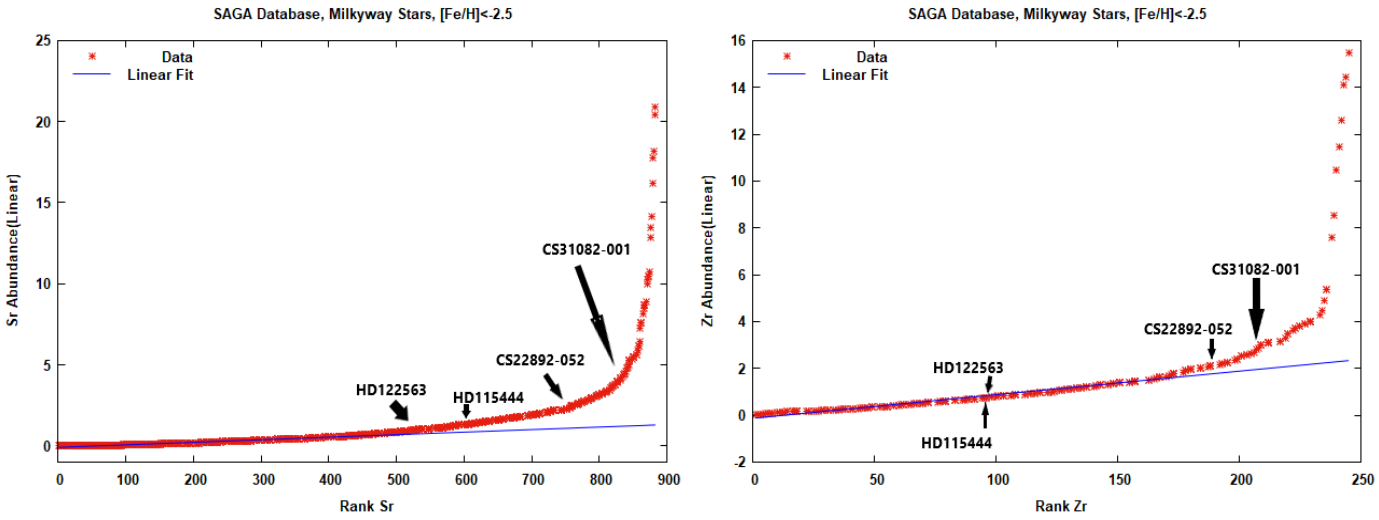

Fig. 14. Abundance trends with ranks. *Left panel*: Sr abundances versus their corresponding ranks up to the regime where the PCCs and SCCs indicate only low correlations, i.e., including complete *r*-process stars of regime 3. We see the start of deviations from a linear behavior already at limited-r stars (HD 122563). *Right panel*: Zr abundances versus their corresponding ranks similar as for Sr. The deviation from a linear behavior starts later at the r-II stars (CS22829−052 and CS31082−001).

and also category 0 (representing regular supernovae) for low metallicity stars which do not even have Eu detected, but show these three elements.

If we summarize these issues with respect to Fe production, we see three types of sources: category 0 (regular CCSNe, producing Fe and light trans-Fe elements, e.g., Sr, Y, Zr and possibly elements up to the second *r*-process peak, but not beyond), and category I and II (special core-collapse supernovae with Fe production accompanied by weak r-processing up to the lanthanides, such as Eu). Category IIIb events might also produce Fe, even more than regular CCSNe, but according to our existing analysis still in negligible proportions in comparison to Eu. This behavior and the appropriate analysis tools has been discussed in Sect. 2.1. During the course of the present paper, we have by now identified quite a number of low-metallicity observations which point to the pollution by several preceding events. This is not really a surprise, as the metallicity of the ISM in a remnant of one CCSN (close to [Fe/H] = −3, as discussed in detail in Sect. 2.1), does not have to coincide with the metallicity of a new-born star, possibly triggered by a nearby supernova. The next stellar generation will form (after turbulent mixing triggered e.g., by the motion of galactic spiral arms) with a probably small contribution of a few percent or even less from this supernova remnant. Therefore one expects lowest-metallicity stars, affected by these first CCSNe, to possess values of about [Fe/H] ≈ −5 or even less (e.g., Norris et al. 2007, 2012; Frebel & Norris 2015; Nordlander et al. 2017). For events which occur with 1/10 of the frequency of regular CCSNe one might then expect the first appearance at [Fe/H] ≈ −4 (after typically 10 supernovae enriched the ISM) and events which take only place after about 100 regular CCSNe polluted the ISM, are expected to show their impact at [Fe/H] ≈ −3. This seems to be what we observe in Fig. 2 for weak and strong *r*-process events, and one should therefore expect that we find already contributions from several events at such low metallicities. This reduces somewhat the significance of correlations, especially with Fe, originating dominantly from high-frequency CCSNe, however, the rank tool applies independently and permits such interpretations. We test this framework in Sect. 6 with existing model predictions.

5. Correlations of actinides with lanthanides and third *r*-process peak elements

Before entering the subject of this section in detail, we want to mention beforehand that our work for it included an extended analysis with a closer look at the entire range of elements in the mass vicinity of Eu, that is from atomic numbers in the range 56−66. These elements are here only considered with respect to their observational abundance determinations. It should, nevertheless, be mentioned at this point that modeling of astrophysical conditions, combined with nuclear properties in order to obtain good fits to solar r-abundances, has led in the past to quite a number of publications with different approaches to (and interpretations for) the *r*-process production of these rare earth elements or lanthanides, especially related to the understanding of the so-called pigmy peak between the second and third *r*-process peak. This is, however, not the focus of this paper, here we want to focus on the interpretation of abundance observations and correlations.

Following the earlier detailed analysis of the Eu behavior, in its extension to the rare earth (or lanthanide) elements we realized that they behave similarly with respect to Fe. The correlation coefficients follow similar trends: two plateau phases for regimes 1 and 2 of limited-r or weak *r*-process stars, and a strongly declining correlation when considering the whole [X/Fe]-range, including the complete or strong *r*-process stars of regime 3. These trends exist in general, although they can be more or less pronounced for the different elements. The overall low correlation with Fe (PCCs around 0.2) for the complete [X/Fe] range, including regime 3 stars, is again a strong indication for no or a negligible (in comparison to solar [X/Fe]) coproduction of Fe in the responsible category III events. Whether and how the lanthanides correlate with the third *r*-process peak and the actinides will now be analyzed more extensively in this section.

5.1. Th and rare earths elements (lanthanides)

The large scatter of [Th/Fe] (see Fig. 11), extending over more than two orders of magnitude (if considering that at lowest

metallicities the real Th/Fe ratio was higher due to the Th-decay since then), is comparable to the [Eu/Fe] scatter in Fig. 2. Thus, considering also that Th is only detected in regime 3 stars, that is stemming only from category III events, where we find no or a negligible coproduction of Eu and Fe, we also find very small global correlations of Th with Fe (PCC < 0.2). We have linked these events dominantly to NSMs, an exception could be due to very massive stars turning into hypernovae and collapsars or magneto-rotational supernovae with existing, but negligible in (comparison to solar) Fe/Th and Fe/Eu production, as discussed in the previous Sects. 3.5 and 4.1. Figure 11 indicated that such objects might dominate the Th production at very low metallicities and Fig. 10 (right panel) showed that a superposition of Th-producing sites (in addition to NSMs) has to exist. Here we examine the differences in Eu and Th productions and their correlation (which go either back to category I, II, and III for Eu or only category III events for Th). Independent of this, the Fe in Eu as well as Th containing stars originates from core-collapse events with a dominant fraction stemming from prior CCSN types of the categories 0, I, and II.

Figure 15 (left panel) shows the PCC and SCC curves of Th and Eu as a function of [Eu/Th]. The linear relationship of Th and Eu is quite strong for the whole set of stars in the database utilized (PCC ≃ 0.86 and SCC ≃ 0.91). Only a small divergence between the two statistical methods appears at [Eu/Th] > 0, unlike in the case of Fe and Eu, which shows a pronounced discrepancy between the two methods when including category III events. This is due to a much smaller scatter in Th/Eu than in Eu/Fe, leading to smaller deviations for fits based on metric or rank displacements (see e.g., Mashonkina et al. 2014; Holmbeck et al. 2018). Furthermore, two subgroups of stars seem to occur, the first one in the regime [Eu/Th] < 0, where the PCCs and the SCCs are identical and almost equal to 1. This subgroup makes up for the so-called actinde-boost stars (where [Eu/Th] is subsolar) and includes the best known star CS31082−001 with [Eu/Fe] ≃ 1.62, [Fe/H] ≃ −2.92 and [Eu/Th] ≃ −0.23. In the second subgroup, with [Eu/Th] ≥ 0, the PCCs and SCCs diverge slightly. This is probably an indication that among the r-enhanced stars two slightly different sets of strong *r*-process conditions prevail, leading to more or less actinide production. The best known star of this category is CS22892−052 with [Eu/Fe] ≃ 1.53, [Fe/H] ≃ −3.1 and [Eu/Th] ≃ 0.17. Plotting the figure as a function of [Th/Eu] instead of [Eu/Th] would lead to a very similar result, just reversing the slightly different behavior in the sub versus super-solar regime. Figure 15 (right panel) shows the plot of Th versus Eu for the two subgroups and the corresponding linear fits. The slope of the regression line in the subgroup of the actinide boost stars is twice as high as for the other subgroup. The corresponding r^2 in both fits are very high and almost equal to 1.

Before entering a more detailed discussion how actinide boosts relate to the different regimes of complete *r*-process stars, that is r-I and r-II stars, we want to first have a look at the Th abundances alone. Figure 10 (right panel) had shown that the observed Th abundances are due to a superposition of (at least) two different types of complete *r*-process sources, which we introduced as category IIIa and IIIb (only category III produces detectable amounts of elements in the third peak and beyond). In Fig. 16 it is shown that one finds linear relationships between Th abundances and their the ranks, if one separates them into r-I and r-II stars, that is in each of these r-I and r-II subsets Th is apparently only polluted by one of the two IIIa or IIIb sources. One should keep in mind, this is a relation of the Th abundance with [Eu/Fe] ranges (different for r-I and r-II stars), pointing to the fact that high Th abundances caused by IIIb events are also linked to high [Eu/Fe] values of r-II stars. One can explain this behavior if one assumes that category IIIb events produce more main *r*-process elements than IIIa events by a large factor (possibly ten, separating r-I with [Eu/Fe] > 0 and r-II star with [Eu/Fe] > 1). Then, if IIIb stands for an actinide boost (and thus a higher Th/Eu ratio than in actinide-normal IIIa events), one finds in ISM regions polluted by such an event high Th abundances, but combined with high Eu abundances or [Eu/Fe] values as well. This then leads exactly to the linear relation between Th abundances and their ranks for r-II stars. In the same way, if IIIa events produce smaller Th amounts by a large factor in comparison to IIIb events, they will also produce small amounts of Eu (although the Eu/Th ratio is higher than in IIIb events, but by a relatively small factor), and lead to a smaller [Eu/Fe], that is the composition of r-I stars. Therefore, it looks that category IIIb events are linked predominantly to r-II stars, while categories IIIa events are linked predominantly to r-I stars.

Outliers from this behavior, as also found in Fig. 16, can occur due to a two phase or inhomogeneous pollution in the early Galaxy. The ISM which eventually formed the low metallicity star we observe, can have experienced subsequent pollutions. If a IIIa event is followed by a category I or II event with a strong nearby contribution, it can lift the [Eu/Fe] highly and causes the star, which carries an actinide-normal behavior, to display an r-II [Eu/Fe] pattern. On the other hand, if a category IIIb event took place quite remotely from the ISM cloud, which led to the observed low metallicity star, it will implant the actinide-boost pattern for Th/Eu, but the mixed in Eu is relatively small in comparison to the preexisting Fe of prior CCSNe, this causes an r-I [Eu/Fe] pattern. This way, especially in two phase pollution events r-I stars can also carry an actinide-boost pattern and r-II stars an actinide-normal pattern.

At this point we list a number of low-metallicity stars with actinide-boost and actinide-normal patterns in combination with their r-II and r-I nature. Before doing so, one should reflect about what is really meant by a regular (actinide-normal) r-abundance pattern and an actinide boost, considering also that ^{232}Th has a half-life of 1.405×10^{10} yr. Lodders et al. (2009) and Lodders (2020) give a solar ratio of Th/Eu = 0.45 or 0.42 ($\log_{10} = -0.347$ or -0.377), dated back to the beginning of the solar system 4.57 Gyr ago. This value resulted from Th contributions to the ISM out of which the solar system formed, which requires also to consider the (long) Th half-life since these events took place (e.g., Hotokezaka et al. 2015; Côté et al. 2019). The present terminology puts a star with observed Th/Eu > 0.42 (the value in the solar system at the date of its birth) in the actinide boost slot. Stars were born with higher Th/Eu ratios before Th-decay than listed in Table 6, this difference is actually utilized for age determinations. When applying the actinide-boost definition of Th/Eu > 0.42, we see ten actinide-boost stars with six of them being r-II stars. If relaxing the limit between r-I and r-II stars from [Eu/Fe] = 1 to 0.9 we find seven of them being of r-II stars. This goes in line with the previous finding from Fig. 16 that actinide-boost stars belong dominantly to the r-II class, but inhomogeneous pollution in the early Galaxy by several overlying events can also lead to high [Eu/Fe] values for stars being born with actinide-normal patterns, as well as low [Eu/Fe] values for an actinide-boost pattern. However, the apparently dominating coincidence of joint r-II and actinide-boost characteristics seems to point to the fact that events responsible for an actinide-boost eject also much more *r*-process matter in total (determining [Eu/Fe]) than those responsible for actinide-normal characteristics.

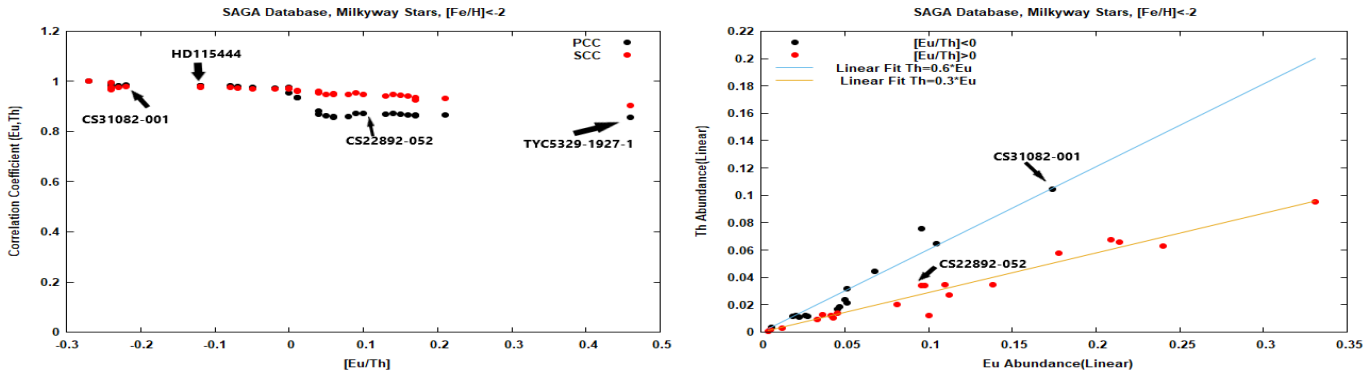

Fig. 15. Correlations of Th and Eu and their relationship. *Left panel*: Pearson and Spearman correlation coefficients for Th and Eu in stars with [Fe/H] ≤ -2 as a function of [Eu/Th]. At [Eu/Th] $\simeq 0$ they start diverging in a moderate way, separating two subgroups (actinide-boost and -normal stars). The positions of three typical stars CS31082−001 (complete, r-II, actinide boost), HD 115444 (complete, r-I, actinide boost), CS22892−052 (complete, r-II), and TYC5329-1927-1 (complete, r-I) are indicated. While the extreme cases CS31082−001 and TYC5329-1927-1 link the actinide-boost and normal behavior to r-II versus r-I stars, this is less clear closer to the dividing line [Eu/Th] = 0. *Right panel*: Th versus Eu abundances in the two subgroups (actinide-boost and actinide normal) of stars with [Fe/H] ≤ -2 and corresponding linear fits.

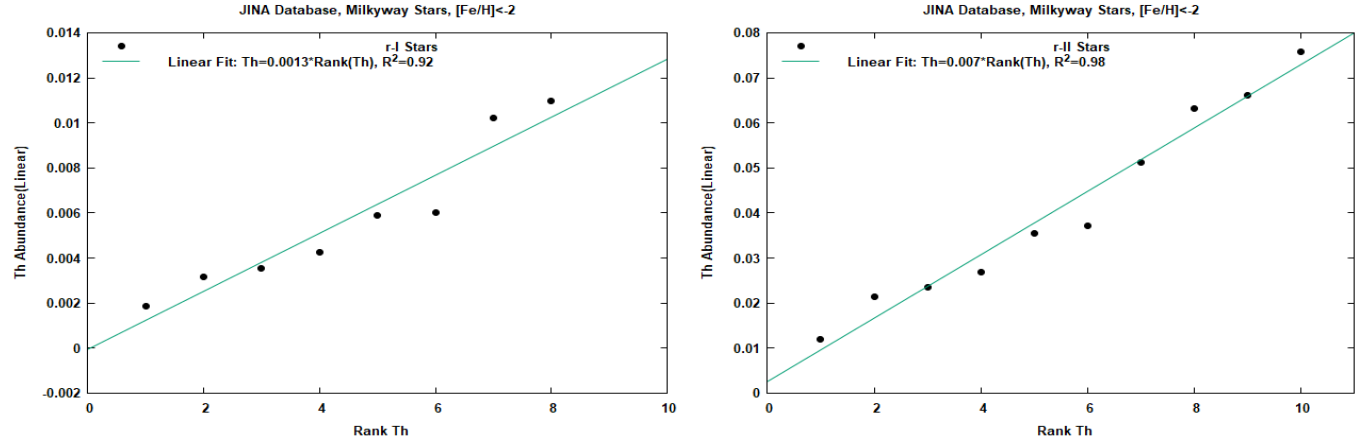

Fig. 16. Th behavior with ranks. *Left panel*: Th abundances plotted versus their ranks for r-I stars. *Right panel*: Th abundances plotted versus their ranks for r-II stars. We find a linear relation for each of these two groups, pointing to unique *r*-process sources for these two regimes, while the global plot of Th abundances versus their ranks in Fig. 10 (*right panel*) indicated a superposition of events.

For comparison we have also done the same analysis for other lanthanide elements in addition to Eu, that is La, Dy, Er, and Yb. They all behave similar to Eu/Th, for the subsolar [X/Th] cases the stars belong to the actinide-boost stars with [Eu/Th] < 0, for the supersolar cases to the regular *r*-process enriched actinide-normal stars.

5.2. Th and (close to) third *r*-process peak elements

In the previous subsection we discussed a clear correlation of the lanthanide elements with Th, varying, however, slightly between the actinide boost stars and the regular r-enhanced stars, pointing to very similar but slightly different strong *r*-process conditions for those elements. Figure 15 had shown this small but measurable difference between actinide boost stars and the regular r-enhanced stars via deviations of the PCC and SCC values, measuring the scatter in different ways. In Fig. 17 we display these correlations with Th for elements being part of or close to the third *r*-process peak. We find that opposite to Fig. 15 the slight divergence between PCCs and SCCs becomes almost negligible, indicating that the pathway to the actinides passes through the third *r*-process peak. This can be interpreted in such a way that if *r*-process environments manage to reach the third peak, they also lead up to the actinides with similar results.

However, there remain still small variations between elements at the (low mass) slope of the third *r*-process peak for actinide boost and regular *r*-process enriched stars, as we can see in Fig. 18 for Os (average $A = 190$) and Ir (average $A = 192$). This can again be noticed in the correlation plot versus [Os/Ir], where the PCCs and SCCs display a small divergence for the higher (Os/Ir) values, belonging to regular *r*-process enriched stars, and the linear correlation seems slightly smaller. When testing the Os and Ir abundances versus their ranks, the relation appears almost linear, that is as expected from a single source. However, small deviations from a linear relation are visible, indicating a possible superposition of similar but slightly different conditions. When the abundances of Os versus Ir are plotted, but split for two different regimes ([Os/Ir] < 0.02 or [Os/Ir] > 0.02), the slope changes by almost a factor of 2 between these two groups, corresponding to actinide boost and regular *r*-processed enriched stars. This behavior (not shown here in a plot) underlines, that the lower mass slope of the third *r*-process peak is still sensitive to such similar but slightly different conditions. On the other hand, when matter has reached the peak, the flow up to the actinides seems unchanged.

Table 6. Trend of Th/Eu with *r*-process enrichment.

Star	Eu	Th	(Th/Eu)	Regime 3 (complete *r*-process) subclass	[Eu/Fe]
TYC5329-1927-1	−1	−1.91	0.12	r-I	0.89
J0858−0809	−2.41	−3.07	0.22	r-I	0.23
HD 108317	−1.37	−1.99	0.24	r-I	0.64
HD 110184	−1.91	−2.5	0.26	r-I	0.08
HE1523−0901	−0.62	−1.2	0.26	r-II	1.86
CS22892−052	−0.86	−1.42	0.28	r-II	1.53
HD 186478	−1.34	−1.85	0.31	r-I	0.63
CS29491−069	−0.96	−1.46	0.32	r-II	1.12
RAVEJ203843.2−002333	−0.75	−1.24	0.32	r-II	1.64
CS29497−004	−0.68	−1.17	0.32	r-II	1.44
J1432−4125	−1.01	−1.47	0.35	r-II	1.44
HE0240−0807	−1.44	−1.9	0.35	r-I	0.55
BD−$15_5$781	−2.28	−2.73	0.35	r-I	0.12
HE2224+0143	−1.02	−1.47	0.35	r-I	0.87
HE2327−5642$^{(*)}$	−1.29	−1.67	0.42	r-II	1.07
HD 6268$^{(*)}$	−1.56	−1.93	0.43	r-I	0.54
HD 115444$^{(*)}$	−1.64	−1.97	0.47	r-I	0.68
HE2252−4225$^{(*)}$	−1.3	−1.63	0.47	r-II	1.12
CS22953−003$^{(*)}$	−1.69	−1.92	0.59	r-I or r-II	0.92
CS31082−001$^{(*)}$	−0.76	−0.98	0.60	r-II	1.62
CS30315−029$^{(*)}$	−2.24	−2.45	0.62	r-I	0.67
HE1219−0312$^{(*)}$	−0.98	−1.19	0.62	r-II	1.47
*red*CS31078−018$^{(*)}$	−1.17	−1.35	0.66	r-II	1.15
2MASSJ09544277+5246414$^{(*)}$	−1.19	−1.31	0.76	r-II	1.28

Notes. (Present day) Observed Eu and Th abundances in $\log \epsilon(\mathrm{X}) = \log(N_\mathrm{X}/N_\mathrm{H} + 12)$ values in low metallicity stars ([Fe/H] < −2.4). The corresponding solar system ratio at the time of its birth (representing the ISM when the solar system got detached) is 0.45 or 0.42 (Lodders et al. 2009; Lodders 2020). Based on their present Th/Eu ratios, the stars with an asterisk would be considered as an actinde-boost stars with Th/Eu > 0.42.

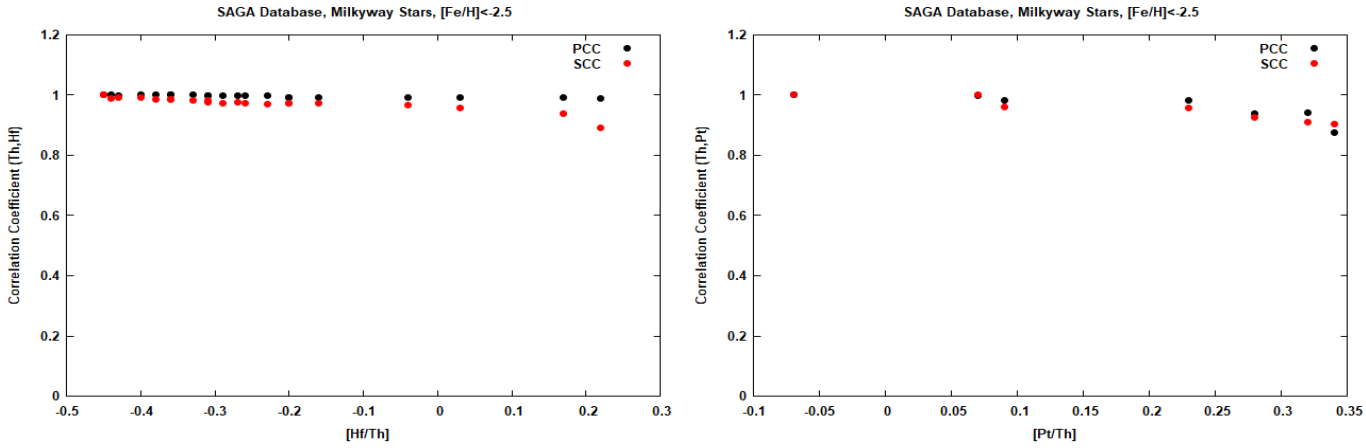

Fig. 17. Correlations of Hf, Pt respectively with Th. *Left panel*: PCCs and SCCs of Th and Hf in stars with [Fe/H] < −2.5 as a function of [Hf/Th]. *Right panel*: PCCs and SCCs of Th and Pt in stars with [Fe/H] < −2.5 as a function of [Pt/Th]. The PCCs and SCCs divergence above [X/Th] ≃ 0 is much smaller than for the lanthanides. Not shown Os behaves in an almost identical way.

6. Interpreting the observational trends in the framework of possible *r*-process sites

6.1. Our findings from the analysis of observational data

In the preceding sections we have gone through a large set of elements at low metallicities with [Fe/H] < −2 or −2.5, initially focusing on Eu, but in addition analyzing Sr, Y, Zr, (Ba, La, Nd, Dy, Er, Yb), Hf, Os, Ir, Pt, and Th, which (at least) at low metallicities are dominated by (weak or strong) *r*-process contributions. The results for the elements in brackets from $Z = 56$ to $Z = 72$ have not been presented here, but we found them to lead to similar results as discussed for Eu. Sr, Y, and Zr have at low metallicities also contributions from regular CCSNe and not only from *r*-process sites. If not considering any selection bias in the SAGA database (Suda et al. 2008), we can find in total 665 stars with [Fe/H] < −2.5, for 379 of them only upper limits with respect to the Eu abundance are

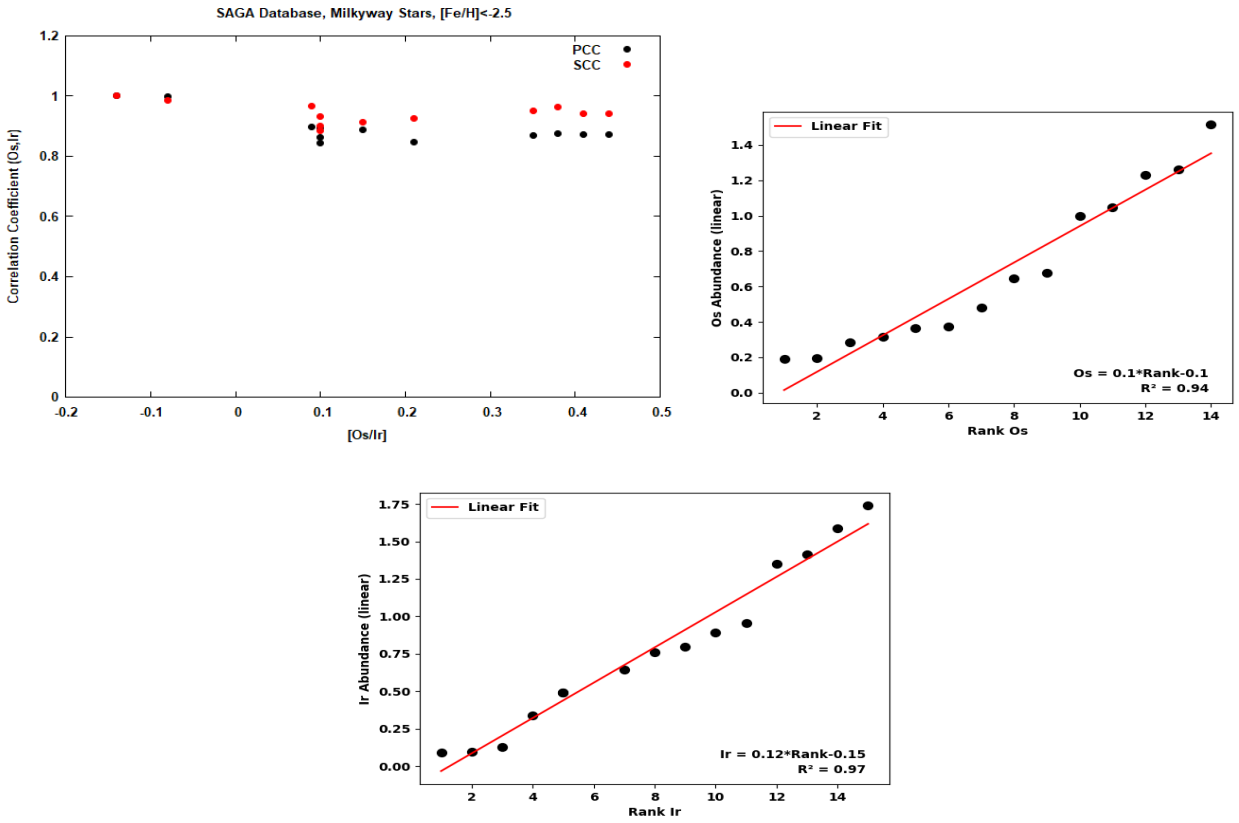

Fig. 18. Correlations of Os and Ir and their trends with rank. *Panel a*: Os versus Ir correlation and *panels b and c*: Os and Ir versus their ranks. The data set includes stars with [Fe/H] < −2.5 and the corresponding linear fits.

known, that is they do not contain a substantial *r*-process contribution beyond the $A = 130$ peak and only upper limits are known. Of the remaining 286 stars, for which direct detections of the Eu abundance exist, 76 belong to the r-poor or limited-r stars with [Eu/Fe] < 0−0.1 and 210 to the r-rich or complete *r*-process stars with [Eu/Fe] > 0−0.1. Thus, a sizable fraction of these low-metallicity stars is carrying the imprint of one or several *r*-process site(s). For all of the ones with [Eu/Fe] < 0−0.1 we found Eu to be strongly correlated with Fe, that is a coproduction of Fe and Eu was indicated. This was also seen for Sr, Y, Zr, as well as Ba and the lanthanide elements La, Nd, Dy, Er, and Yb.

Typically, we found two kinds of plateaus in the correlation patterns among limited-r stars with Fe, seeing for the first one (a) a clear linear relation with the Fe-abundance, and in the slightly less correlated region (b) an apparently also linear relation with Fe, but with a larger slope and also a larger scatter. The second case, could point to a further *r*-process source, also displaying a high correlation with Fe. These limited-r or weak *r*-process stars with a high correlation to Fe (a core-collapse product) made the connection to core-collapse events, occurring early on in galactic evolution. They seem to produce Fe and *r*-process matter, but not (in detectable amounts) elements up to the third *r*-process peak. We have introduced them as category I and category II events. Therefore, we concluded that category I and II components coproduce Fe and the *r*-process elements up to the lanthanides, however, category II in a stronger (but more scattered) fashion. For Sr, Y, Zr the (two) plateaus seem to appear a bit more fuzzy or can, if plotted versus [X = Sr,Y,Zr/Fe] rather than [Eu/Fe], even be interpreted as a three plateau behavior. For this behavior, one can introduce an additional category 0, coproducing with Fe also light trans-Fe elements, possibly even up to the second *r*-process peak (see e.g., Fig. 10 in Ghosh et al. 2022), but not contributing up to Eu. Therefore, regular CCSNe are clear candidates.

Thus, we have now introduced three categories of nucleosynthesis sites which coproduce Fe with heavier elements (category 0 with trans-Fe elements and possibly even up to the second *r*-process peak, categories I and II containing also weak *r*-process element up to the lanthanides, that is including Eu, but no third peak elements and actinides). The question is how this enters into chemical evolution (Fig. 1) and how it affects the original hypothesis that low-metallicity stars with [Fe/H] < −2.5 carry only the imprint of one nucleosynthesis site. In such a case a correlation, that is a close to constant ratio of two elements, would point clearly to a coproduction in that specific site. This would also apply for the case if one has different pockets, related each to one nucleosynthesis site with separate clusters of abundance patterns, where each of them points only to one contributing site. Having introduced category 0, regular CCSNe with high frequency which can show up already at [Fe/H] = −5, see Sect. 2.1, leads to the question whether a VMP star can already carry the imprint of several nucleosynthesis events. We should keep in mind that this might endanger the interpretation of correlation as coproduction. We encountered such situation first when looking at *r*-process enriched stars which also contain Fe in addition to *r*-process elements. The strong advantage was that because of a clearly missing correlation, this underlined separate independent contributions and thus made clear that the contributing *r*-process site(s) must come with no or negligible Fe production.

As was discussed earlier, the remnant matter of a single CCSN should have a [Fe/H] value between −2.5 and −3.

However, most probably the star formation triggered by such a nearby supernova did not lead to a more than 10% pollution of the protostellar cloud, if not less. This would point to the lowest metallicity stars in the range [Fe/H] ≈ −4 or less (we see them already at −6). Thus, at [Fe/H] = −3, already contributions by 10 to 100 CCSNe could exist. The question is how often category I or II events would have contributed as well. If one starts with a suggested site, magnetorotational supernovae – possibly related to magnetar-producing events (e.g., Beniamini et al. 2019) –, one would expect that about 10% of CCSNe fall into the class of magnetorotational supernovae. Taking present-day models with the ejection of about 10^{-6} $M_{\odot}$ of Eu (e.g., Winteler et al. 2012; Nishimura et al. 2017; Reichert et al. 2021), and ten regular CCSNe with about 0.1 $M_{\odot}$ of Fe, would lead to an Eu/Fe mass ratio of about 10^{-6} and an abundance ratio of about 3×10^{-7} (the Fe-ejecta of the order $2-4\times10^{-2}$ $M_{\odot}$ of one such category II event do not change this ratio strongly, see Sect. 6.3.1). This compares reasonably well with what can be seen in Fig. 9, right panel, where we see a scatter of a factor of 2 (up and down), allowing for variations in the Fe contributions from CCSNe as well as the Eu contribution from a magnetorotational supernova. This could explain the only moderately strong correlation found in PCC values in Fig. 3 and Table 3. The overall combined CCSN (category 0) and magnetorotational supernova (category II) Eu and Fe ejecta are consistent with these observations, but the Fe contribution of the latter would only play a minor role. This might put doubts on a proof for coproduction based on the found correlations, although a close to constant about 10% contribution by those events could still be realized as a correlation. We should keep this in mind for the further analysis in this section. For the moment we keep the idea of such category I and II events with a coproduction of Fe and Eu, leaving direct tests of model predictions for them in Sect. 6.3.1. Fortunately, the tool of the abundance versus rank analysis, utilized by now in a number of cases, is not affected by the uncertainties which we described above. This clearly permits to identify several *r*-process contributions for a number of elements in limited-r as well as *r*-process enriched stars.

Among the totality of *r*-process enriched stars with [Eu/Fe] > 0−0.1, we noticed up to now a vanishing or at most negligible correlation of *r*-process elements with Fe (see Fig. 3, right panel and Table 2). Their abundances must have originated from events with a strong *r*-process and negligible Fe production (in comparison to solar Fe/Eu) which we introduced as category III events. The existence of Fe, if not correlated with an *r*-process, points to an almost pure *r*-process site, polluting matter which had previous Fe contributions from CCSNe. We also noticed a nonlinear behavior of abundances versus their ranks for Eu and Th among r-I and r-II stars combined, (i.e., with [Eu/Fe] > 0−0.1), when considering all stars with [Fe/H] < −2.5. Thus, also category III events include superpositions for these elements (see Figs. 7, left panel and 10, right panel).

We have noticed in the case of Th, that this superposition led to a clear division into two types of events, displaying within regime 3 of *r*-process enriched stars a linear relation for each of the two subregimes of r-I and r-II stars (see Fig. 16). This finding relates to r-I and r-II stars which exhibit Th detections. If we try the same approach for Eu separately for r-I and r-II stars, we do not see clear linear relations in regime 3, as displayed in Fig. 19. The Eu contributions to r-I as well as r-II stars must, in addition to category IIIa and IIIb sources, experience also a feeding in from category I/II events which dominate in regimes 1 and 2. Thus, subcategories IIIa/b are the only ones responsible for producing elements in and beyond the third *r*-process peak (such as Th), but the lanthanide element Eu displays also in regime 3 contributions from category I and II events. We know from our earlier analysis that such category I and II events produce Eu. Here we see that these types of events provide also a contribution to regime 3 and not only to limited-r regime 1 and 2 stars. We attempt to estimate this contribution in the following subsection.

If we attempt a linear fit of Eu versus Fe abundances, separately for r-I and r-II stars (although knowing from our earlier analysis that over the whole regime of complete r-stars Eu and Fe are uncorrelated), we obtain the following results displayed in Fig. 20. The r^2 value of 0.44 for r-I stars corresponds to a PCC of 0.66 while 0.42 for r-II stars corresponds to 0.62, underlining the moderate correlation. But the linear Eu/Fe ratios determined, provide averages for the two samples, equivalent to mean [Eu/Fe] values for the two subregimes. We apply these means later when trying to identify the origin of the observed abundance patterns.

6.2. Attempts to link event categories to contributions in observational regimes and to determine their occurrence rate

We have discussed in the preceding subsection that the interpretation of abundance correlations among elements X and Y becomes more complicated if several events have contributed to these elements, as we know that already at low metallicities supernovae contribute via Fe ejecta (and possibly Sr, Y, Zr), but not necessarily to true *r*-process elements. Fortunately, the rank tests permitted to identify whether multiple nucleosynthesis sites caused this behavior. In the following we test these options in order to see which kind of events (i.e., which of the categories 0, I, II, and III) contributed, and whether it is possible to give an idea of the respective role they play in the overall patterns of *r*-process elements found in regimes 1, 2, and 3.

6.2.1. An estimate for the fraction of the elements Sr, Y, Zr, and Eu made by non-CCSNe events

As already shown in the previous sections, in stars with [Eu/Fe] < 0−0.3 the rare earth (RE) or lanthanide element Eu can be produced by events of category I and (or) II, which we have attributed to specific CCSNe scenarios. For [Eu/Fe] > 0−0.3, that is complete *r*-process stars of regime 3 (corresponding to r-I and r-II stars), the Eu production has been predominantly assigned to category III events with no or negligible (in comparison to solar Fe/Eu) Fe coproduction. The latter could still be divided in categories IIIa and IIIb, but we leave them together for the moment in order to simplify things. We discuss the astrophysical origin of all these categories later. In order to estimate the respective Eu fraction from weak *r*-process sites (category I and II) and highly efficient *r*-process sites of category III, we utilize the relationship between the Eu abundances and their ranks.

As we discovered earlier, also shown in Fig. 7 (right panel), for Fe this type of relationship seems to be close to linear with a possible deviation at the highest ranks. This speaks for a dominant production site (core-collapse supernovae, possibly with higher Fe yields for the most massive star collapses, i.e., hypernovae and collapsar). In contrast, for Eu such a linearity is close to solid only for regimes 1 and 2 (see Fig. 8), corresponding to category I and II events, that is events which we interpreted also to result from core collapse via a special kind of supernova which coproduces Fe and Eu. As we have shown in Fig. 16, we have for Th a clear sign of unique contributions from

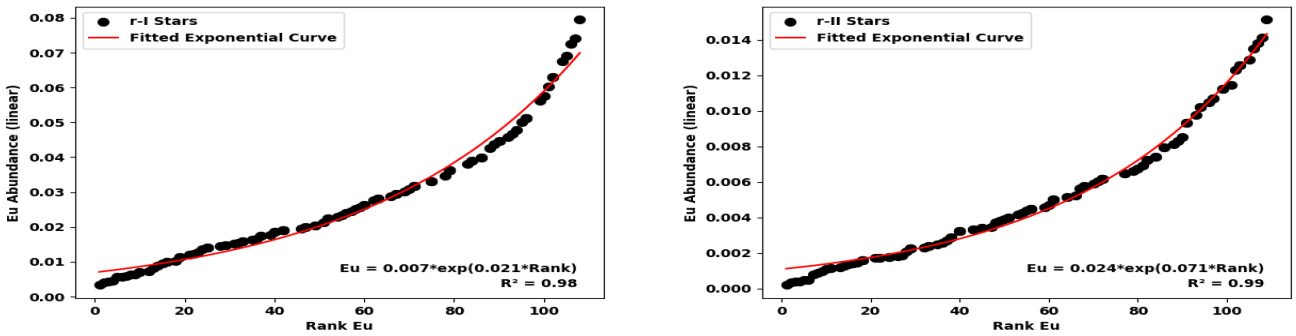

Fig. 19. Eu abundance behavior with rank. *Left panel*: Eu abundances versus their ranks for r-I stars. *Right panel*: Eu abundances versus their ranks for r-II stars. Opposite to Th which clearly pointed to two distinct sources for these two regimes, each via a linear relationship, Eu still seems to require other contributions, in addition to the subcategories IIIa and IIIb.

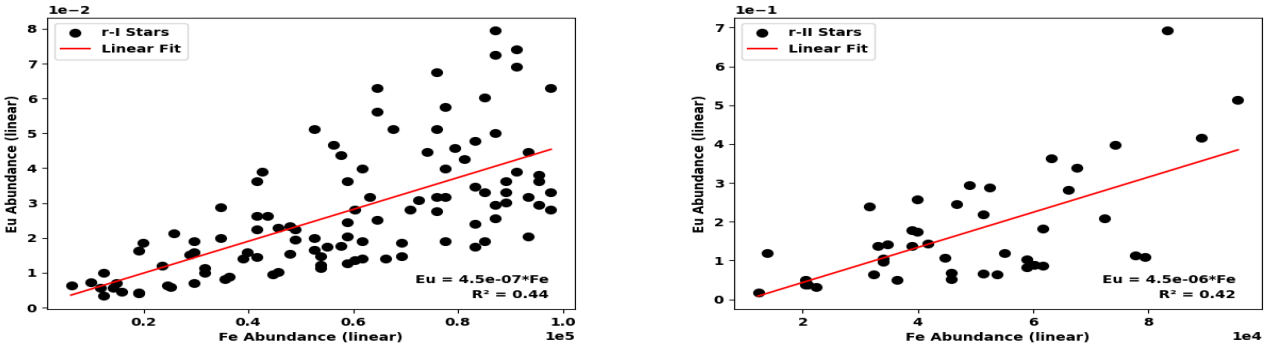

Fig. 20. Relationship between Fe and Eu abundances for r-I and r-II stars. *Left panel*: Eu abundances versus Fe for r-I stars. *Right panel*: Eu abundances versus Fe for r-II stars. The PCC values of 0.66 and 0.64, corresponding to the displayed r^2's underline a moderate correlation for both star types. The determined mean Eu/Fe ratios will be utilized in Sect. 6.3.2.

category IIIa and IIIb events and no detectable superpositions from supernova-type events which produce a weak *r*-process. Opposite to this, Eu seems in all regimes to indicate superpositions (see Figs. 7, 8, and 19), that is also contributions from category I and II events. It is therefore important to also estimate for regime 3 the contributions from weak *r*-process (category I and II specific CCSN) events, leaving the remaining fraction for category III events. The assumption is that the trend found before for weak *r*-process events continues. One option is to utilize Fig. 8 which permits to predict the Eu abundance (calibrated for weak *r*-process stars with a coefficient of the order 10^{-4}) as a function of the Eu rank. This method is utilized for the third entry in Table 7. For the rank method we use the following relation, Eu(category I + II) = $9 \times 10^{-5} \times$ Rank(Eu), and the amount of Eu which then needs to be attributed to events of category III is given by Eu(III) = Eu(tot) − Eu(category I + II).

Table 7 summarizes for a number of selected regime 3 stars the fraction of Eu predicted this way by weak *r*-process CCSNe. When utilizing these estimates and integrating over the total number of VMP stars with $-0.64 \leq$ [Eu/Fe] ≤ 1.92 in the SAGA database, this results in an amount of Eu, originating from weak *r*-process CCSNe of the order 20%. Thus, the major part of Eu (and very likely the whole RE element or lanthanide region) should be due to category III events, but the category I and II contribution is substantial.

We have utilized a similar approach for the three adjacent light trans-Fe elements Sr ($Z = 38$), Y ($Z = 39$) and Zr ($Z = 40$). Here we show Zr as representative case for the neighboring trans-Fe elements and extend our PCC and SCC analyses also for the correlation of Fe with Zr, utilizing exactly the same method as before for Fe and Eu, applicable here, because Fe as well as

Table 7. Eu amount estimation based on rank analysis.

Star	[Eu/Fe]	Eu (CCSNe category I and II)$_{\rm rank}$
HD 107752	0.31	22.2
BS16543−097	0.4	14
HE0105−6141	0.51	12.6
HE2206−2245	0.6	14.1
HD 115444	0.68	14.9
HE0315+0000	0.7	9.9
CS29499−003	0.79	7.3
CS22882−001	0.81	8.7
HE1127−1143	0.9	6.6
HE2138−3336	1.09	7.1
CS22183−015	1.36	4.6
HE2208−1239	1.52	3.6
CS22892−052	1.53	3.7
CS31082−001	1.62	3
CS31062−012	1.65	1.3
HE2258−6358	1.68	1.6
HE0010−3422	1.72	1.8
LP625−44	1.74	1.5
CS29497−034	1.79	2
HE0243−3044	1.9	0.8

Notes. Estimate of the Eu amount (in %) stemming from weak *r*-process CCSNe (category I+II) in selected stars with [Eu/Fe] > 0.3.

Sr, Y, Zr come from the same dominating event, regular CCSNe. Figure 13 showed the resulting curves for the correlation coefficients versus [Zr/Fe]. As in the Fe and Eu case (Fig. 3, right

Table 8. Zr amount estimation based on rank analysis.

Star	[Zr/Fe]	Zr (CCSN events)$_{rank}$
HD 107752	0.05	70
BS16543−097	0.31	45
HE0105−6141	0.19	55
HE2206−2245		
HD 115444	0.2	66
HE0315+0000	0.3	49
CS29499−003	0.45	36
CS22882−001	0.44	43
HE1127−1143		
HE2138−3336	0.81	30
CS22183−015	0.76	37
HE2208−1239	0.84	34
CS22892−052	0.62	49
CS31082−001	0.75	41
CS31062−012		
HE2258−6358	0.69	31
HE0010−3422	1.08	17
LP625−44	1.52	5.4
CS29497−034		
HE0243−3044	1.06	11

Notes. Estimate of the Zr amount (in %) originating from CCSN events in selected stars with [Zr/Fe] > 0.05 and Zr detections.

panel), we observe a divergence of the PCC and SCC curves, here for a value of [Zr/Fe] ≃ 0.3. The relation between Zr and its ranks is shown in Fig. 14. Similar to the case of Eu, the best fit between Zr and its ranks is close to linear for the low rank values of regime 1 and 2 stars. For a first order estimate we utilize the linear relationship shown in Fig. 14 to obtain the results shown in Table 8 (containing the same stars as Table 7 but showing gaps when Zr detections are not known). When integrating over the total number of the VMP stars with $-0.5 \leq$ [Zr/Fe] ≤ 1.91 in the SAGA database, the amount of Zr originating from CCSN-type events is about 33%. The chemical element Y ($Z = 39$) has only one stable isotope (^{89}Y). It shows the same behavior as [Sr/Fe] and [Zr/Fe], concerning the divergence between the PCC and SCC curves. This happens at [Y/Fe] ≃ −0.15 and Y is also the product of different astrophysical sources. When integrating over the total number of the VMP stars with $-1.49 \leq$ [Y/Fe] ≤ 1.41 in the SAGA database, the amount of Y originating from CCSNe is about 37%. Concerning the chemical element Sr ($Z = 38$), the divergence between the PCC and SCC curves takes place at roughly [Sr/Fe] ≃ 0.2 (see Fig. 13). Following the same procedure as for Zr and Y, when integrating over the whole VMP stars with $-2 \leq$ [Sr/Fe] ≤ 1.32 in the SAGA database, the amount of Sr originating from CCSN-type events is about 50% and the remaining part of about 50% is originating from category III events. In the case of an observational bias (number of observed r-poor versus r-enriched stars in comparison to a different real distribution) these fractions could increase significantly.

6.2.2. The frequency of category III events based on the Eu-Fe correlation pattern

In the previous sections we discussed the ratio of two elements X/Y imprinted by explosive events into the interstellar medium, being then inherited in new star formation environments. We want to address here once more Eu/Fe. If different categories of *r*-process environments would always come with an Fe coproduction and a specific ratio of Eu/Fe, one would see this directly in observations. Instead in reality, one finds certain ranges for r-poor (regimes 1 and 2), and r-enriched stars (regime 3). In order to test realistically how certain classes of event categories contribute to galactic evolution, one should know defined abundance production patterns for all categories, inject them with the appropriate event frequencies with the delay of stellar (or system) lifetimes before injection, plus treating the whole system inhomogeneously in a 3D approach during the early phases of the galaxy. And all of this should preferably also be done as a function of metallicity. Such approaches have been developed (Wehmeyer et al. 2015; Cescutti et al. 2015; van de Voort et al. 2020, 2022) but are nevertheless still in their infancy. In addition, the required abundance pattern predictions for all events are still highly uncertain. Therefore, we have tried here a reverse engineering approach, based on observations and correlations.

Let us in a first simple approach assume that the observed abundance ratios in the three regimes are consistent with appropriate variations within the different event categories (i.e., production sites) and that these observations indicate the coproduction of the observed elements. In this case each of the low-metallicity stars carries the imprint of one explosive nucleosynthesis site. However, our introductory words in Sect. 2.1 left also the option, supported by the findings in Sect. 6.1 that this might not necessarily be true in certain phases of galactic evolution and that several events could have already contributed to the abundance pattern of VMP stars. Here we want to verify in a first test whether the general assumption of an overall Fe and Eu coproduction would be consistent with the correlation pattern of Fe and Eu as shown in Fig. 3 (right panel). The method consists of:

1. Randomly generating equally distributed Fe values (20 000) between $\log \epsilon \simeq 3.4$ and $\log \epsilon \simeq 5$ ($\log \epsilon = \log(N_{Fe}/N_H) + 12$), which corresponds to metallicities [Fe/H] between −4 and −2.5 of our data.
2. Randomly generating for each of these metallicity values equally distributed (Eu/Fe) values (20 000) between 2.4×10^{-8} and 1.4×10^{-5} to mimic the ratio of Eu and Fe throughout the three regimes (see Table 5 for more details).
3. Calculating for each of these entries the corresponding Eu values by multiplying the (Eu/Fe) ratios in the list of item two with corresponding Fe values in item one.
4. Items one through three result in a list of Eu and Fe abundance pairs of sample stars for which one can test correlations via PCCs and SCCs as a function of [Eu/Fe].

This procedure was repeated many times, in order to test how robust the calculated PCC and SCC curves are. It results in the following behavior (not shown here in a figure): When Fe and Eu were always coproduced throughout the three categories with the ratios chosen in item 2, the correlation of Fe and Eu remains at a relatively high level throughout the whole [Eu/Fe]-range at about 0.65 instead of 0.2 for the real case. One finds a linear relation between Eu and Fe abundances with a moderately broad scatter. Furthermore, the PCC and SCC curves do not diverge at all. Thus, two interesting features emerge from these tests: (1) Despite largely varying individual Fe and Eu abundances for the sample stars, the correlations between Eu and Fe remain moderately high, as long as Fe and Eu are added jointly to a stellar composition, and (2) PCCs and SCCs do not diverge, contrary to the case when utilizing observational data. In that case we saw a strong decline for increasing [Eu/Fe]-values and a divergence between PCCs and SCCs. Thus, adding jointly Eu and Fe

over the whole observed [Eu/Fe]-interval, which represents the three regimes, is not consistent with reality. This agrees with our previous findings that category III stands for a strong *r*-process contributor with no or negligible Fe production (in comparison to solar Fe/Eu ratios).

Therefore, we performed an additional test, assuming that Fe and Eu are only coproduced in categories I and II, which should be responsible for reproducing data in regimes 1 and 2 with [Eu/Fe] < 0−0.3. A fraction λ ($0 \leq \lambda \leq 1$) of Eu (here defined as Eu*) is produced in addition without Fe in category III. This stands for an independent *r*-process source with no (or negligible) coproduction of Fe. The question is how this reproduces regime 3 stars, as we know from the previous analysis (see Table 7) that also category I and II stars contribute to the Eu in regime 3. This means that we do not necessarily find *r*-process Eu from only a single event which contributed to a proto-stellar cloud of the ISM before star formation, but we might need to determine Eu* by subtracting the category I/II contribution. Therefore, the second test consists of:

1. As in test 1 choosing the metallicity, that is the Fe abundance of a sample star by randomly generating equally distributed Fe values between $\log\epsilon \simeq 3.4$ and $\log\epsilon \simeq 5$, which corresponds to metallicities between −4 and −2.5 of our data.
2. Adding Eu from category I and II stars for the same metallicity via randomly generating equally distributed (Eu/Fe) values between 2.4×10^{-8} and 2×10^{-7} to mimic the ratio of Eu and Fe in the first two regimes (see Table 5 for more details).
3. Adding Eu* from category III stars. This is obtained (in an approximation) in two steps: (a) Randomly generating equally distributed (Eu/Fe) values between 2.1×10^{-7} and 1.4×10^{-5} to mimic the ratio of Fe and Eu in regime 3 (see Table 5 for more details). (b) However, Eu* in a regime 3 sample star should be obtained by subtracting the category I and II contribution.
4. Thus, we utilize the Eu$^{\rm I/II}$ (multiplying the (Eu/Fe) values of item 2 with the Fe value for this chosen metallicity of item 1) and subtract it from the Eu, as obtained in item 3(a) for the same chosen metallicity. This results in Eu* in regime 3, which is only stemming from category III events without Fe coproduction.
5. The remaining question is how frequent category III events are in comparison to category I and II events. Therefore, we multiply Eu* with a free factor λ in the range from zero to one. The total Eu of the sample star is then Eu = Eu$^{\rm I/II}$ + $\lambda \times$ Eu*, providing at the end the pair of Fe and Eu values of this sample star and also its Eu/Fe ratio.
6. This permits to calculate the PCCs and SCCs of the overall Eu and Fe correlation as a function of [Eu/Fe].

The procedure described above is clearly an approximate one and should in principle be followed at some point by a large-scale inhomogeneous chemodynamical evolution simulation that takes into account the contribution of all discussed sources, their frequency and the individual time evolution. On the other hand, it also includes the simplification that one only talks about category I and II events and category III events, rather than dividing also into I and II as well as IIIa and IIIb. The procedure also assumes that each regime 3 star contains also contributions from category I and II sources. This, however, is strongly supported by the findings of the previous subsection (see Table 7) which actually analyzed the Eu contributions from category I and II events to regime 3 stars. Keeping this in mind, and following the outlined procedure of test 2, Fig. 21 results. We utilized two choices for the division between limited-r (regime 1 and 2) stars and *r*-process enriched stars (regime 3). The top figure shows observational PCC-values and selected results of PCC-values for the test cases with λ = 0.01 (1%), 0.02 (2%), 0.03 (3%), 0.04 (4%) and 0.1 (10%) when utilizing [Eu/Fe] < 0.3 for the upper limit of limited-r or r-poor stars. We realize, however, in the bottom figure that a break at [Eu/Fe] = 0 rather than at 0.3 would be a better choice for dividing among limited-r and *r*-process enriched stars. This is in line with our previous finding that Th, a strong *r*-process product, is found already in stars with [Eu/Fe] > 0 (see Fig. 10). We see that the best agreement with the correlation pattern of observational data is achieved for values of λ close to 0.02. This means that only about 2% of all events contributing Eu (without Fe) via *r*-process sites are sufficient, in order to explain the Eu and Fe correlation pattern. This exercise does not yet point to concrete scenarios for category III events and does not make a difference between IIIa and IIIb events, as long as the Fe coproduction is negligible.

The two tests performed above simplify somewhat reality, but they come with the result that the strong *r*-process events of category III, producing Eu without Fe, stand for only a 2% fraction in comparison to Fe and Eu coproducing core-collapse events, which we introduced as category I and II events. What does this finding say about the ratio of strong *r*-process events, producing Eu without Fe, to regular CCSNe? In the SAGA database there exist 932 stars with Fe and Sr detections. Out of these 282 stars show Fe, Sr and Eu. These represent 30% in comparison to the 650 stars which show Fe and Sr without Eu. The latter could be identified with regular (i.e., category 0) CCSNe which probably coproduce Fe and Sr. Thus, following this interpretation that category III events represent 2% of the whole sample of category I and II plus III events, and all these represent only 30% of all category 0, I/II, and III events (dominated by regular CCSNe category 0 events), we find about 6 per mil of category III events in comparison to the overall CCSN events. This is within uncertainties (including possible astronomical selection biases plus the chance that some CCSNe might not produce Sr) close to the 2 per mil of compact binary merger events in comparison to CCSNe found in Rosswog et al. (2017), consistent with a neutron star merger rate of 3.7×10^{-5} yr^{-1} (Pol et al. 2020) and a CCSN rate in the Galaxy of 1.6×10^{-2} yr^{-1} (Rozwadowska et al. 2021).

6.3. Identifying the suggested *r*-process sources/event categories by comparison with observational regimes

In the preceding subsections, we have categorized *r*-process sources in events of category I, II, and III (with the sub categories IIIa and IIIb) without trying definitely, yet, to identify them with stellar sites (although some of these discussions took place, already). When focusing on the Fe-group elements we tried to be already more concrete and pointed to stellar core collapse with varying initial stellar masses. We also mentioned that even in the case of regular (neutrino-driven) core-collapse supernovae, due to $Y_{\rm e}$-variations in the ejecta (see e.g., Ghosh et al. 2022), light trans-Fe elements such as Sr, Y, and Zr and even elements up to the second *r*-process peak can be produced. We introduced for these sources category 0 events. In the following we want to discuss possible production sites of the identified *r*-process categories.

A minimal requirement for an *r*-process is a sufficiently large neutron-to-seed-nuclei ratio, which depends on $Y_{\rm e}$, the entropy, and the expansion velocity of ejected matter. These conditions have to be compared with possible scenarios for the different categories of events which we have concluded to exist from observational constraints and correlations.

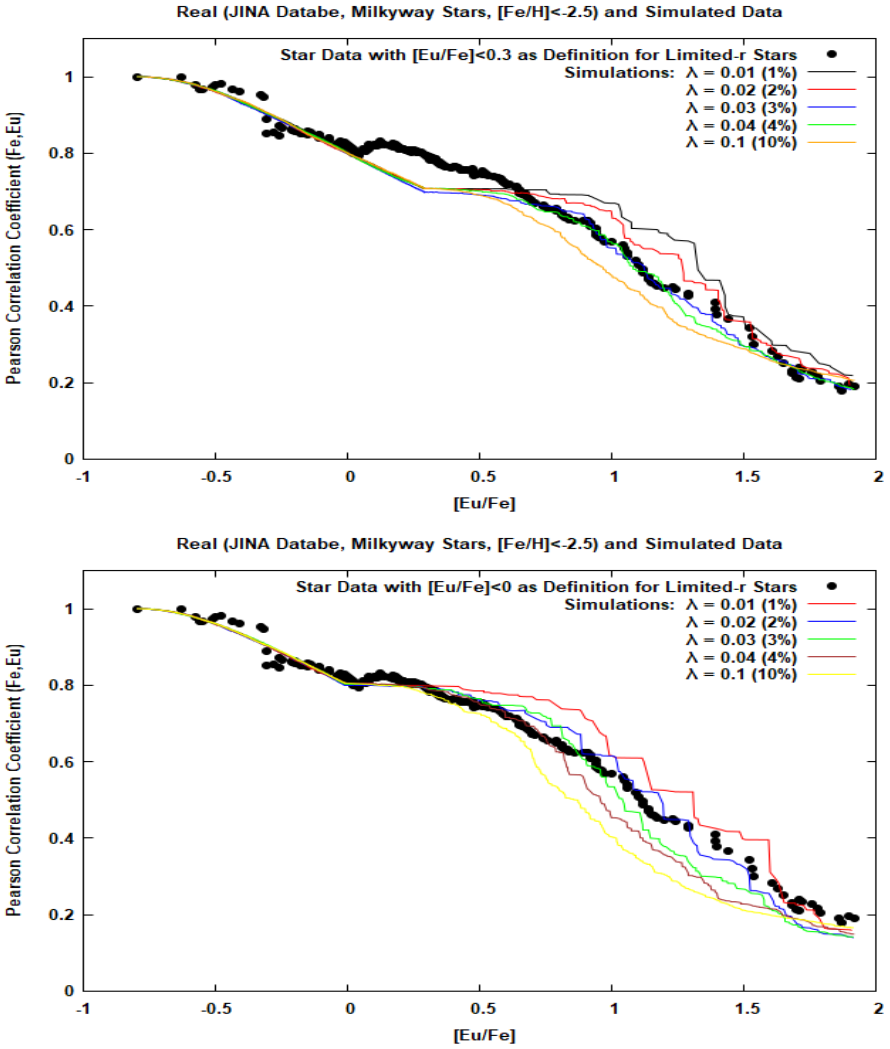

Fig. 21. Simulation of the PCCs and SCCs of Fe and Eu. PCC values of real and randomly generated Eu and Fe in stars with [Fe/H] < −2.5. See the text for this approach where λ relates to the fraction of category III events (where Eu is added independently without adding any Fe) versus the sum of category I+II+III events. *Top panel*: [Eu/Fe] < 0.3 is utilized for the upper limit of limited-r stars. *Bottom panel*: [Eu/Fe] < 0 is utilized as an upper limit for the same star type. In both cases a λ of about 2% seems to provide the best fit to the data.

In the introduction we have discussed the following possible *r*-process sources: (a) regular core-collapse supernovae with either no or only a very weak *r*-process and a *νp*-process, possibly producing in a combined fashion elements such as Sr, Y, and Zr and beyond, (b) electron capture (EC) supernovae in the 8−10 $M_\odot$ mass range (if they exist and are not disqualified by their abundance pattern for realistic Y_e's), (c) magneto-rotational supernovae with a varying (dependent on initial magnetic fields and rotation rates) weak to strong *r*-process (probably in most cases weak), (d) quark-deconfinement supernovae of massive stars that explode due a quark-hadron phase transition at supranuclear densities (rather than the commonly assumed neutrino-powered mechanism), (e) collapsars (observable as hypernovae) that lead to a black hole plus torus configuration, and finally (f) compact binary mergers (of both double neutron star and neutron star – black hole systems) driven to coalescence by gravitational wave (GW) emission.

Out of these sites (a) might provide the conditions for a very weak *r*-process and *νp*-process, whether only up to Sr, Y, Zr or up to (but not beyond) the $A = 130$ peak is still debated (Wanajo et al. 2018; Curtis et al. 2019; Fischer et al. 2020a; Ghosh et al. 2022). (b) is a class of supernovae whose existence is put into question after recent re-determinations of the electron capture rate of ^{20}Ne (Kirsebom et al. 2019a,b), but is not firmly excluded, however, leading to a too strong decline in abundances as a function of A for realistic Y_e-conditions (Wanajo et al. 2011). (c) could plausibly lead to magnetars, neutron stars with surface magnetic fields of the order 10^{14} G, which form in ∼1 out of 10 of core collapse supernovae (e.g., Beniamini et al. 2019). Dependent on the initial fields, varying weak (probably dominating) to strong *r*-process conditions can be obtained, the latter, however, only for precollapse fields beyond 10^{12} G (Winteler et al. 2012; Mösta et al. 2014, 2015, 2018; Halevi & Mösta 2018; Nishimura et al. 2015, 2017; Bugli et al. 2020; Reichert et al. 2021). Case (d) has been proposed for a while. Dependent on the nuclear equation of state for massive core-collapse events, the collapse of the proto-neutron star to a black hole can be avoided (in a narrow stellar mass range) due to a quark-hadron phase transition with the right properties. The ejecta would experience a weak *r*-process, but populating even the actinides, however, with negligible abundances (Fischer et al. 2020b). Case (e) has been extensively discussed in the context of long-duration gamma-ray bursts (Woosley 1993; MacFadyen & Woosley 1999; MacFadyen et al. 2001). They involve the collapse of massive stars that rotate rapidly enough so that an accretion torus can form outside of the last stable orbit of a forming black hole, and they go along with relativistic polar and nonrelativistic torus outflows. This scenario has been proposed by Cameron (2003) as an *r*-process site and recently been examined in more detail by Siegel et al. (2019)

and Siegel (2019). The remaining site, (f), is related to compact binary mergers (see Thielemann et al. 2017; Rosswog et al. 2017; Cowan et al. 2021, for overviews).

In the literature one can find further suggestions for weak *r*-process sites, that is predictions from neutrino winds of magnetized neutron stars (Vlasov et al. 2017) and from neutrino winds of regular CCSNe following the explosions (e.g., Wanajo 2013). However, there exist open questions about these yields and (or) their importance. (i) Wanajo utilized a $Y_e = 0.4$ for his proto-neutron star winds – presently it is not clear whether such low values can be attained (Wanajo, priv. comm.) – and the effect comes only for quite massive neutron stars. On the other hand Bollig et al. (2021) show that a long-term accretion flow over seconds hinders the neutrino-driven wind. They suggest that the wind develops only in the lowest-mass cases. (ii) The above mentioned investigations for magneto-rotational supernovae predict dynamical ejecta of the order $0.01-0.1\ M_\odot$, while the wind ejecta of Vlasov et al. (2017) for fast rotating magnetized proto-neutron stars (which should follow such dynamical ejecta) are of the order 10^{-4} to $10^{-3}\ M_\odot$. Here one might need to include both such ejecta (the dynamical as well as the wind ejecta), which we discuss when considering case (c).

All the sites from (a) to (e) relate to massive stars, and except for (e) they are essentially candidates for a weak *r*-process. (c) can possibly vary from a weak to (in rare cases) a strong *r*-process, (e) is a convincing case for a strong *r*-process. All of these events will coproduce Fe, but for the strong *r*-process candidate (e) this amounts to a negligible level in comparison to solar Fe/Eu ratios, for case (c) this depends on the strength of magnetic fields and the rotation rate.

The progenitors for the cases (a) to (f) vary substantially in their initial electron fractions: all sites apart from (f) start with a pre-explosion Y_e-value close to 0.5 and de-leptonize to low Y_e-values just prior to or during the collapse and explosion (and they need to avoid reraising Y_e, for example via ν_e-capture as in case (c) for low magnetic fields). Only the sites related to (f) start at the opposite end with electron fractions close to 0.05 (see Fig. 22) and the ejecta becoming releptonized by positron- and ν_e-captures. Extremely low initial Y_e-values provide compelling environments for a strong *r*-process. During the explosive event, which triggers an *r*-process, it is unlikely to maintain a perfect β-equilibrium, but during the expansion a transition from (close to) one β-equilibrium to (close to) another one is possible. Matter may, for example, transition from cold, catalyzed neutron star matter with a very low Y_e to a higher-Y_e β-equilibrium state that is determined by the balance of electron and positron as well as neutrino and antineutrino captures. Thus, when assuming that the temperatures in the explosion are large enough to drive matter (close to) β-equilibrium, this may provide us with some hints on the physical conditions at the production site. To fix orders of magnitude, we show in Fig. 22 the β-equilibrium values (assuming vanishing neutrino chemical potentials) for a broad range of physical conditions. The concrete values have been calculated using the DD2 equation of state (Hempel & Schaffner-Bielich 2010), but deviations for other equations of state are only expected at the highest densities ($\gg 10^{14}$ g cm^{-3}) that are very unlikely to be ejected and therefore are not relevant for our discussion here. Not too surprisingly, the matter inside a neutron star is extremely neutron-rich ($Y_e < 0.1$) with Y_e-values actually starting to dip down to close to zero when approaching 10^{14} g cm^{-3}. The figure also includes contour lines of Y_e values in the range 0.1−0.15, which have been identified as optimal conditions for an *r*-process with an actinide boost (e.g., Holmbeck et al. 2019; Wu, priv. comm.; Thielemann et al. 2022; Eichler et al. 2019).

6.3.1. Category 0, I, and II events

Let us first try to make the connection to category 0, I, and II events which are responsible for either producing only the trans-Fe elements or are responsible for a weak *r*-process, including Eu production but no (or negligible amounts of) third *r*-process peak or actinide elements. They all showed apparently very strong or strong correlations with Fe, as discussed in earlier sections. One major question is whether the nondetection of Eu in a large fraction of stars means that (i) all such stars have not experienced any Eu or *r*-process pollution or (ii) whether this is just due to observational uncertainties. (i) would be consistent with the non-production of a weak *r*-process in regular CCSNe, being in line with a strong debate about a full *r*-process occurrence in such events. The production of Sr, Y, Zr, and even heavier elements below the $A = 130$ peak seems possible in a combination of a *νp*-process (e.g., Fröhlich et al. 2006; Eichler et al. 2018) and a (very) weak *r*-process (Wanajo et al. 2018; Curtis et al. 2019), for the latter see also Kratz et al. (2007), Farouqi et al. (2009), and Akram et al. (2020), but Eu seems not to be produced. An excellent update on this situation is recently provided by Ghosh et al. (2022). This would exclude within our present understanding a weak *r*-process Eu production in regular CCSNe, opposite to category I or II events. Therefore, we decided to call them category 0 events, underlined already to some extent by an apparent three-plateau feature in the correlations for Sr, Y, and Zr (Fig. 13). The remaining options for category I and II events among the listed sources would be (b) electron capture supernovae, (c) magneto-rotational supernovae and (d) quark-deconfinement supernovae. All limited-r or weak *r*-process stars are characterized by a high Sr/Eu ratio (see Fig. 2, right panel) and a very strong to moderately strong correlation of Eu with Fe, indicating a coproduction of Fe and Eu. This was the reason to identify them with a type of core-collapse supernovae. We have summarized presently available predictions for EC supernovae (EC SNe, Wanajo et al. 2011), magnetorotational supernovae (MHD1 and MHD2, Nishimura et al. 2017; Reichert et al. 2021), and QD supernovae (Fischer et al. 2020a) in Table 9, taken from Fig. 5 in Wanajo et al. (2011), Figs. 4 and 5 in Nishimura et al. (2017) (in a restricted range of magnetic field strengths), Table 2 in Reichert et al. (2021) (one out of 4 models), and Table 3 in Fischer et al. (2020a), in comparison to the observed ratios in low metallicity stars of regimes 1 and 2. If one would add late wind contributions of Vlasov et al. (2017) to the magnetorotational models, they would at most add 10% to the Sr and Eu values presented in Table 9. The listed sources are the ones expected to be explained via category I and II events. We note that some of these entries contain a range of values due to a variety of models contained in these publications. For the EC supernova models we utilize the entries for Y_e between 0.2 and 0.25 instead of a more realistic $Y_e = 0.4$. This goes beyond uncertainty estimates permitting Y_e values only down to 0.3. However, for such values no Eu would be produced, underlining that EC supernovae (if existing) probably are not good candidates for category I or II events. The MHD1 results represent the range of *i* entries for intermediate magnetic fields, the MHD2 entries take the only model which produces non-negligible amounts of Eu, but an average over the range of magnetic field strengths and rotation rates would probably be different. Sr ejecta could be lowered by a factor of 10 while Fe ejecta can be higher by up to a factor of 10 than listed. The QD supernova entry gives the range of two model predictions. The observational entries for regime 1 and 2 are taken from Fig. 2 (right panel) for Sr/Eu, taking the full range of the observations,

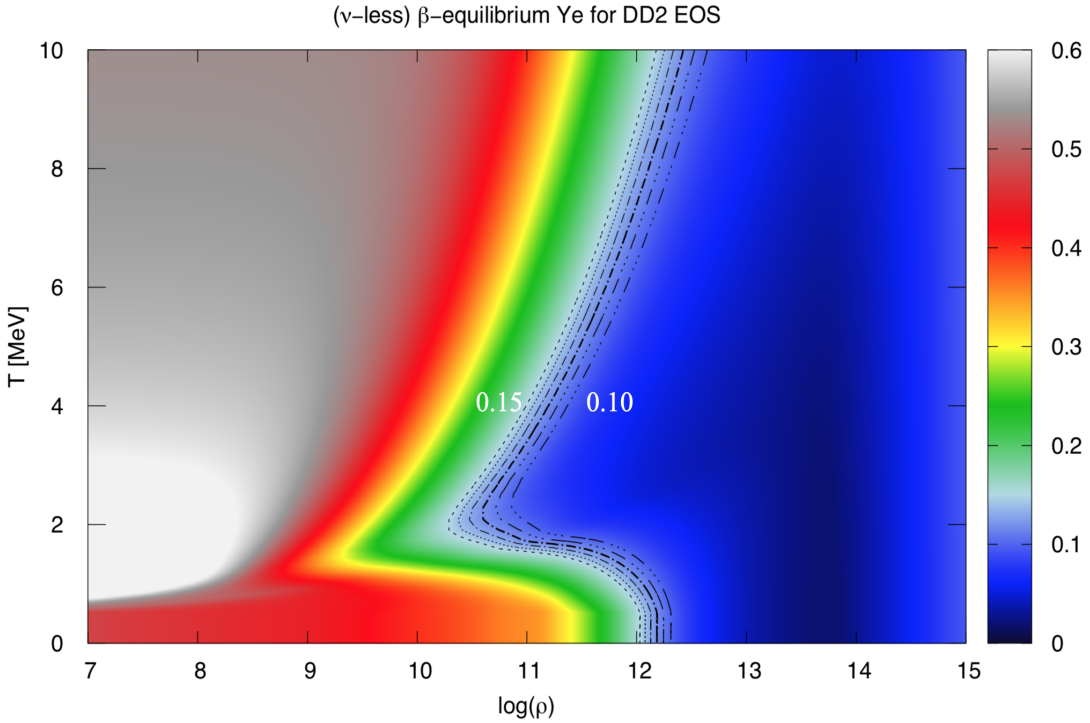

Fig. 22. β-equilibrium Y_e for DD2 EoS. β-equilibrium values for a broad range of relevant densities and temperatures, employing the DD2 equation of state. The colors indicate Y_e, contour lines in the range of 0.1 to 0.15 are also displayed.

for Sr/Fe the upper limits of the second and third plateau in Fig. 13, and for Eu/Fe the average values based on the fits in Fig. 9. The Eu/Fe ratios which we find in regime 1 and 2 stars are on average of the order 2×10^{-8} and 10^{-7}. Thus, in case the observed abundance ratios in those stars would reflect directly the production ratios from the pollution by a single event, we should find consistent and identical ratios in the responsible event ejecta. The last line of Table 9 contains also the total amount of ^{56}Ni (decaying to Fe) ejected in the models/sites considered here for weak *r*-process events (but, as mentioned before, this can vary strongly in the variety of models considered for these types of events).

We see for all the candidates in Table 9 a reasonable agreement between model predictions and observations for the Sr/Eu ratios, representing a typical weak *r*-process pattern (maybe with exception of the EC SNe which get close to the observed ratios only with highly reduced Y_e values, stretching the uncertainties possibly beyond permitted limits). Generally, the Sr/Fe and Eu/Fe ratios seem to be two to three orders of magnitude too high. For magnetorotational SNe this might be due to the fact that we included cases with too high magnetic fields, case *i* from Nishimura et al. (2017) and 35OC-Rs from Reichert et al. (2021). When utilizing lower magnetic fields on average, the Sr as well as Eu abundances will be reduced and the Fe abundances enhanced. This can reduce Sr/Fe ratios by one to two orders of magnitude (Reichert, priv. comm.), but a constraint would be that on average the Eu/Fe ratios need to be reduced in similar proportions as Sr/Fe, in order to obtain the same Sr/Eu ratio. This depends on the distribution of such model properties (magnetic field strength and rotation rates) in realistic samples, as the lanthanide fraction beyond the second *r*-process peak is much more sensitive to such changes than the Sr abundance.

In all cases the Sr/Fe as well as Eu/Fe ratios produced in these events are exceeding the ones observed in regime 1 and regime 2 stars by a large factor. A solution to this, in line with our previous discussion, is that – already at these low metallicities – we do not see only a single event pollution, but that for these regime 1 and regime 2 stars already many regular supernovae contributed as well, adding essentially Fe, but only affecting mildly the Sr/Eu ratio with existing but small Sr production. Independent of these considerations, but in line with what was just said, the magnetorotational supernovae (item c in our list of possible sites) show a highly varying degree of the *r*-process strength, dependent on the initial magnetic field and rotation. Due to this they will come with a larger scatter which we also see for regime 2 in Fig. 9. This might qualify them as good candidates for category II. Weak *r*-process stars of regime 1 show a highly uniform behavior. Thus, such ejecta properties would also be required from category I events. Electron-capture supernovae seemed ideal candidates in this respect, but they have recently been put in question with respect to their real existence (Kirsebom et al. 2019a,b). While the outcome is still open (Jones et al. 2016), and they could possibly be considered as a well-defined event, being progenitors of low mass neutron stars (Hüdepohl et al. 2010) with robust abundance features (Wanajo et al. 2011), the probably much too high Sr/Eu ratio puts them in question. It remains to be seen whether QD supernovae (d) could be an alternative for category I events or (with possibly improved physics input in future investigations) also regular supernovae (a).

What remains to be said, while MHD1 and MHD2, as well as the QD supernovae, show a reasonable Sr/Eu ratio consistent with regime 1 and (or) regime 2 stars, the Sr/Fe and Eu/Fe ratios are by orders of magnitude higher than what is seen in observations. This argues for the additional Fe floor from prior regular CCSNe mentioned above (but not producing Eu, and possibly Sr only to a negligible extent) that has existed before pollution with a category I or II event. This is in line with our previous findings that category 0 supernova ejecta can already be found at metallicities as low as [Fe/H] < -5. Comparing the

Table 9. Observed element ratios versus astrophysical events.

Element ratio	Obs. Regime 1	Obs. Regime 2	EC SNe	MHD1	MHD2	QD
Sr/Eu	200–750	200–800	$300–10^5$	438–1300	340	142–468
Sr/Fe	$<2\times10^{-6}$	$<2.5\times10^{-5}$	3.3×10^{-2}	7×10^{-3}–5×10^{-2}	2.6×10^{-2}	$(5.1–5.8)\times10^{-3}$
Eu/Fe	2×10^{-8}	10^{-7}	3×10^{-7}–10^{-4}	$1.5–3.6\times10^{-5}$	7.5×10^{-5}	$(1.1–4.1)\times10^{-5}$
Fe [$M_\odot$]			3×10^{-3}	3×10^{-2}	2×10^{-2}	5.5×10^{-2}

Notes. Candidates for category I and II events.

produced Fe from the simulations shown in Table 9 to the typical Fe-production in CCSNe shows options for reducing the apparent overproduction. If we would link QD supernovae to category I events (responsible for regime 1) and magnetorotational supernovae to category II events (responsible for regime 2 with the larger scatter), we find an overproduction of Sr/Fe and Eu/Fe by a factor in excess of 1000 and 150–360 (or even up to 750) for QD and magnetorotational supernovae, respectively. Thus, we would need n additional supernovae with 0.1 $M_\odot$ of Fe to reduce these ratios to the ones observed in regimes 1 and (or) 2. This leads to $0.055 + n \times 0.1 = 1000 \times 0.055$ for QD supernovae or $0.02+n\times0.1 = 750\times0.02$ and $0.03+n\times0.1 = (150\,\text{to}\,360)\times0.03$ for the MHD2 or MHD1 models of magnetorotational supernovae. Taking this at face value would require the addition of about 500 CCSNe with their Fe to each QD supernova in order to reproduce the observations of regime 1 and 45 to 107 (for MHD1) and 150 (for MHD2) CCSNe in addition to each magnetorotational supernova to reproduce the observations of regime 2. But permitting Sr/Fe and Eu/Fe ratios for magnetorotational supernovae, averaged over the full range of magnetic field strengths and rotation rates (with decreased Sr and Eu and increased Fe ejecta), could reduce these ratios by up to a factor of 10, resulting in n values around 10, consistent with the number of supernovae from massive stars which lead to magnetar formation. This result is consistent with the discussion in Sect. 6.1, where we utilized ejected Eu masses of the order 10^{-6} $M_\odot$ from magnetorotational supernovae, while the entries for MHD1 and MHD2 in Table 9 vary between 1 and 5×10^{-6}. To summarize: about 500 CCSNe per QD supernovae, and possibly a number as small as 10 regular CCSNe per magnetorotational supernova are required to explain the observations for regime 1 and 2, respectively. This has to be taken with care, requiring that these simulation models are approaching reality. The number for the ratio of regular CCSNe (with typically 0.1 $M_\odot$ Fe production) to the category I as well as II events would make sense, as these are at the higher end of the IMF and for QD supernovae in a very narrow stellar mass range or require for magnetorotational supernovae specific conditions for precollapse magnetic fields and rotation rates (possibly consistent with the fraction of CCSNe resulting in magnetars).

6.3.2. Category III events

Finally, we have also to identify the astrophysical counterparts of category IIIa and b events. Let us begin with sites of type (f) compact binary mergers, more specifically the mergers of two neutron stars, since they are the only events that have been directly observed to synthesize (both strong and lighter) *r*-process nuclei, as discussed in the introduction. Fe could not be detected, underlining a noncorrelation of the heavy *r*-process elements with Fe. However, the two neutron stars originate from earlier CCSN explosions which produced Fe. All *r*-process

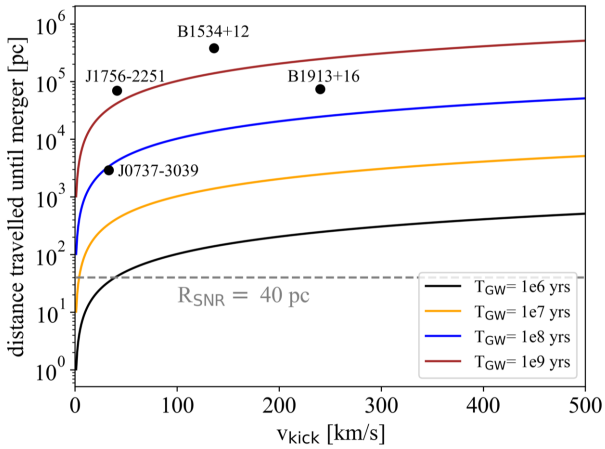

Fig. 23. Distance travelled by neutron star binaries until the merger. A few neutron star binaries with sufficiently known details to determine the gravitational wave inspiral time T_{GW} and the distance travelled until the merger, based on their kick velocities. The observational data are taken from Table 3 in Tauris et al. (2017).

enriched stars in regime 3 contain Fe as well. The reason of that is, these stars are polluted by the merger, but they could also contain products from the preceding supernovae. Whether the Fe stems from the two supernovae of the progenitor system or prior frequent CCSNe needs to be discussed. It relates to the question whether the neutron star mergers take place within the supernova remnant(s), spanned out after the preceding supernovae explosions, or the merger might take place outside the remnants due to neutron star kick velocities. Here we show those neutron star binaries from the overview Table 3 in Tauris et al. (2017) where gravitational wave inspiral times T_{GW} and system velocities are known. With this information we know which distance each binary moves before the merger and we can compare this distance to the typical size of a supernova remnant (SNR). Of those systems none will merge near their supernova remnants. In Fig. 23 even the closest one, the double pulsar J0737−3039, will merge about 100 SNR radii from the site of the last supernova. Thus, at least for these selected well-known systems the neutron star merger ejecta will not easily mix on short time scales with their prior supernova ejecta.

The question remains whether the cases presented in Fig. 23 are a representative sample for the whole merger population or are affected by an observational bias. It is easier to detect long-lived systems, as for higher eccentricities the merging event will come much faster (see, e.g., Fig. 1 in Rosswog 2015a). Nevertheless, it needs a v_{kick} as small as 30 km s^{-1} (while these kick velocities are typically as high as several hundreds of km s^{-1}) in order to inspiral and merge after a short period of 10^6 years within a range of about 30 pc (smaller than a typical supernova remnant). The presence of *r*-process-enriched ultra-faint

dwarf galaxies (UFDs) with a shallow gravitational potential suggests small natal kick velocities for binary neutron stars at birth (<15 km s^{-1}, Beniamini et al. 2016). In fact, the analysis of observed binary neutron stars in the Milky Way suggests that the majority of the systems receive small kicks of <30 km s^{-1} (Beniamini & Piran 2016), although a high velocity population of >150 km s^{-1} exists as well (about 20%, Behroozi et al. 2014). Thus, to summarize: we expect a low-kick population, but even such a population would need an extremely short inspiral time of only 10^6 years in order to be able to permit mixing of the merger ejecta with Fe from the preceding supernova remnants. In addition, a high-kick population exists, which is very unlikely to merge within the supernova remnant. In the second case the question arises how enriched the ISM was already with Fe ejecta of other independent supernovae at the point when the merger takes place. This is independent of the preceding double supernova system, responsible for creating the binary neutron star system. In all cases NSMs fulfill the requirements of category III events, that is no or negligible correlation of *r*-process elements with Fe. Nevertheless, as we know from observations, the ISM around the merger apparently contains already preexisting Fe.

We have also discussed case (e), that is collapsars, as contributors to category III, this way having two category III subcategories: IIIa (NSMs) and IIIb. In addition, those magneto-rotational supernovae of case (c) with highest magnetic fields, permitting a strong *r*-process, might also be possible contributors to category III events, although Mösta et al. (2018) argue that the high fields required are unlikely, and in most cases (in 3D simulations) a kink instability prevents a strong *r*-process, causing only a weak one. Both types of events, that is collapsars and extreme cases of magnetorotational supernovae, would come with some coproduction of Fe (small in comparison to solar Fe/Eu), displaying maybe a small but possibly negligible correlation. Such explosions related to the most massive stars occur already in the earliest phases of galactic evolution, that is for sure at [Fe/H] < −3. A further analysis with respect to the appearance of strong *r*-process events at very low metallicities might also help to test whether not only core-collapse events of massive stars can be responsible at such low metallicities, see Fig. 11. Wehmeyer et al. (2019) investigated neutron star – black hole mergers in chemical evolution studies, systems which would also lead to a black hole torus, similar to collapsars. Also neutron star mergers, with a large combined mass and fast black hole formation, can lead to black hole torus systems. How in those cases the prior binary evolution retards the merger event in galactic evolution with respect to metallicity remains an important issue. The above considerations lead to the questions of the identification of category IIIa and IIIb events, and the possible relation to an actinide boost.

An interesting question is related to the division between actinide boost stars and normal r-enriched stars which display a strong *r*-process. In Fig. 10 (right panel) we have seen that the actinide production (Th) is due to a superposition of events. In Fig. 16 we saw a clear difference for two distinct subgroups in regime 3, related to two subcategories of category III (IIIa and IIIb), explaining r-enriched stars responsible for solar-type strong *r*-process abundances as well as actinide boosts. We could also show that this division is somewhat related to the observational classes of r-I and r-II stars. Thus, two questions have to be answered: (i) what are the environment conditions permitting such an actinide boost, and (ii) which astrophysical objects experience these physical conditions. (ii) could possibly lead to further questions whether environments different from typical neutron star mergers could be responsible, that is neutron star – black hole mergers or possibly collapsars. But let us first concentrate on (i), the required environment conditions.

Recent studies (Holmbeck et al. 2019) based on one hydrodynamic trajectory from tidal dynamical ejecta[4] conclude that actinides are substantially overproduced relative to lanthanides for Y_e-values in the range 0.1–0.15, due to the influence of fission cycling. This is consistent with Wu (priv. comm.) Thielemann et al. (2022) and a recent study of Eichler et al. (2019), which finds, with a variety of nuclear mass models, that slightly larger electron fractions in the range of ∼0.15 are most favorable to explain actinide boost matter. Interestingly, the initial neutron stars, or also massive stars before core-collapse, are practically free of such matter. In Fig. 24 (left panel) we have binned the masses according to the Y_e-values of initial neutron stars. The models were calculated by solving the Tolman-Oppenheimer-Volkoff equations together with realistic equations of state (DD2 and SFho). We show the results for two masses, 1.4 $M_\odot$, representing the probably most common neutron star mass, and 1.8 $M_\odot$, at the higher mass end but consistent with the recent LIGO detection GW190425 (Abbott et al. 2020), where at least one neutron star was very heavy. Plotted is the mass fraction inside the neutron star that has an electron fraction above the Y_e-value given on the *x*-axis. To fix ideas, let us focus on the black line (1.4 $M_\odot$ and DD2-EOS): the curve starts trivially at a value 1, since all the matter has a nonzero Y_e. The curve shows that essentially the whole star has an electron fraction below ∼0.08 and only a tiny mass fraction of $\sim 10^{-4}$ has a Y_e above this value. In other words: there exists hardly any matter in the original neutron stars in the range that is required to produce actinide boost stars. This result is rather robust against changes of the mass and the EOS. Similarly, massive stars before becoming collapsars or hypernovae do not contain matter with the required properties before core-collapse.

Given that actinide boost stars contribute a substantial fraction to the *r*-process enriched stars, requiring a dominant fraction of the ejecta to originate from a very narrow Y_e-range in order to reproduce their observed abundance pattern, indicates that nature robustly produces a restricted range of conditions where such Y_e-values occur. The question of how this in nature takes place, is up to now not settled. We want to discuss here a new, admittedly somewhat speculative possibility.

A binary merger, where a central neutron star survives, drives, due to the intense neutrino irradiation, the electron fraction of the secular ejecta values well beyond the upper limit of 0.15 for an actinide boost (Perego et al. 2014; Martin et al. 2015; Sekiguchi et al. 2016). To corroborate this, we plot in Fig. 24, right panel, the equilibrium electron fractions for neutrino-driven winds (Qian & Woosley 1996)

$$Y_e^{\rm eq} \approx \left[1 + \frac{L_{\bar\nu_e}\left(\epsilon_{\bar\nu_e} - 2\Delta + 1.2\Delta^2/\epsilon_{\bar\nu_e}\right)}{L_{\nu_e}\left(\epsilon_{\nu_e} + 2\Delta + 1.2\Delta^2/\epsilon_{\nu_e}\right)}\right]^{-1} \approx \left[1 + \left(\frac{\epsilon_{\bar\nu_e}}{\epsilon_{\nu_e}}\right)\left(\frac{L_{\bar\nu_e}}{L_{\nu_e}}\right)\right]^{-1}. \quad (1)$$

Here, $\Delta = 1.293$ MeV is the neutron-proton mass difference, $\epsilon = \langle E^2\rangle/\langle E\rangle$ relates to neutrino energies, and L to their luminosities. In the approximation on the right we have assumed that neutrino energies are large enough so that, to acceptable accuracy, the terms containing Δ can be neglected. This approximation is shown in the right panel of Fig. 24. We mark in the plot the relevant contours $Y_e = 0.10$ and 0.15, and we have indicated the equilibrium Y_e region that is expected, based on the neutrino

[4] Trajectory from the simulations described in Rosswog et al. (2013).

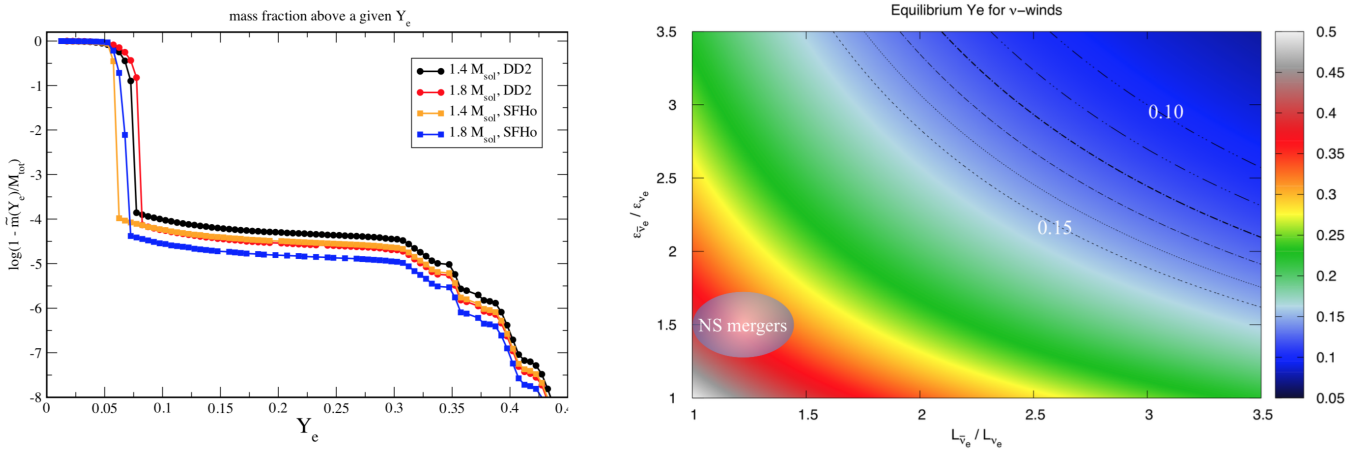

Fig. 24. Mass fraction in neutron stars above a given electron fraction and conditions for an actinde boost. *Left panel*: mass fractions in neutron stars above the given electron fraction Y_e of the x-axis. Rather insensitive to mass and equation of state, the bulk of a neutron star has an electron fraction below ≈0.08, only a tiny mass fraction of $\approx 10^{-4}$ is above this value. *Right panel*: equilibrium Y_e in a neutrino-driven wind as a function of the ratio of (anti)neutrino energies and luminosities (see text for details). Marked is the Y_e-range favorable for an actinide boost (0.1−0.15) and the regions expected for neutron star mergers.

properties from neutron star merger simulations (Dessart et al. 2009; Rosswog et al. 2013; Perego et al. 2014; Sekiguchi et al. 2016; Foucart et al. 2016), assuming such neutrino-dominated environments will also attain a weak equilibrium, which may only be the case for long-lived central neutron stars. If so, neutrino-driven winds from neutron star mergers with surviving central remnants are not viable candidates for actinide boost matter. In reality simulations contain a spectrum of ejecta, starting from ejected tidal tails of essentially pristine neutron star matter up to the high Y_e-values related to the discussed neutrino-driven winds which reached a weak equilibrium. However, it is not expected that in this spectrum the preferred narrow Y_e-interval around 0.1−0.15 plays a dominant role.

If instead a black hole is present or forms, the neutrino irradiation is dramatically quenched and the gas flow around the BH robustly regulates itself into a state of mild electron degeneracy. Due to negative feedback between electron degeneracy and neutrino cooling (higher degeneracy leads to fewer electrons and positrons, therefore reducing the neutrino emission, which leads to a higher temperature and thus to a lowering of the degeneracy), the disk midplane settles inside of the inner $\sim 10\, GM_{\rm BH}/c^2$ to electron fractions of $Y_e \approx 0.1$ (Beloborodov 2003). Interestingly, this occurs once the accretion rates exceed an ignition value (that depends on the BH spin, see Chen & Beloborodov 2007) and the corresponding accretion rates are those that are needed to power (long or short) GRBs (Lee & Ramirez-Ruiz 2007). While discovered in semi-analytic models, this self-regularization to low Y_e-values in the disk midplane is also found in full-fledged numerical (magneto-) hydrodynamic simulations, see, for example, Siegel & Metzger (2018) and Fernández et al. (2019).

The simulation of such neutrino-cooled accretion flows is a major challenge since models should include the (potentially self-gravitating) MHD flow around a rapidly spinning black hole, (semi-transparent) neutrino transport and effects of composition, degeneracy and nuclear recombination. To make things even harder, one needs to resolve the small length scales of the magneto-rotational instability (Chandrasekhar 1960; Balbus & Hawley 1998) and to evolve the black hole torus system for a very large number of dynamical time scales (up to several seconds, while the dynamical time scales are ∼ms). Therefore, it is not entirely surprising that the exploration of this topic is still in initial stages, that large parts of the relevant parameter space are not explored yet and, where parameters are comparable, the results do not yet agree (at least not concerning the ejecta composition). The currently existing GRMHD explorations (Siegel & Metzger 2017, 2018; Miller et al. 2020; Fernández et al. 2019) agree that a large fraction (∼40%) of the initial torus mass becomes unbound, but to date there is no agreement about the resulting Y_e and composition of the ejecta[5]. Despite the current lack of consensus about the ejecta properties, we find the black hole torus idea for the source of actinide boost material compelling since

(a) it is the only convincing scenario that we are aware of that regulates itself robustly into the needed Y_e range,
(b) the progenitors are known to exist,
(c) there are good physical reasons why torus black hole systems form in this parameter range. For example, compact binary mergers have, maybe within a factor ∼3, total masses of a few $M_\odot$. They start out with a huge orbital angular momentum reservoir which is continuously diminished by GWs until disruption occurs close to the last stable orbit. The angular momentum left at this stage is still very large and chances are good to form a substantial accretion torus. In double neutron star merger cases where a black hole forms, the large inherited angular momentum ensures that the post-merger black hole has a substantial dimensionless spin of $\chi \approx 0.8$ (Kiuchi et al. 2009; Rezzolla et al. 2010). If the merging system consists of a neutron star and a black hole, the latter cannot be too massive, otherwise the neutron star is swallowed as a whole and no substantial torus forms (for Schwarzschild black holes their mass must be $\lesssim 8\, M_\odot$, see e.g., Fig. 18 in Rosswog 2015b). Substantially spinning BHs ($\chi \geq 0.8$) are permitted to have larger masses. In any case, the resulting BH-torus system has similar parameters. Single stars have much less of a reason to form BH-torus systems in the suitable parameter range. However, if they really are the causes of long GRBs, they must accrete at rates

[5] For example, Fernández et al. (2019) find Y_e values around 0.12, those of Siegel & Metzger (2018) peak around ∼0.14 while Miller et al. (2020) find a broad distribution between 0.2 and 0.4.

in the range from $\sim 5 \times 10^{-3}$ to $\sim 0.1\, M_\odot\, s^{-1}$ and they could therefore be in a similar parameter range (Siegel et al. 2019). And last, but not least,

(d) they have additional signatures –gamma ray bursts– that are regularly observed.

The progenitor systems of actinide boost material could then be either neutron star binaries that form massive enough accretion disks and black holes, or neutron star black hole systems that form substantial tori (either from low mass black holes or large BH spins) and, potentially, also collapsar accretion disks. There are good reasons to believe that the relativistic jets needed for GRBs are triggered when a black hole forms (McKinney et al. 2013, 2014; Ruiz et al. 2016, 2019; Murguia-Berthier et al. 2017)[6]. If black hole torus systems indeed manage to eject matter with properties similar to what they produce robustly in their inner torus regions, and a black hole is needed to launch an (either long or short) GRB (rather than, say, a magnetized neutron star), then it would be the GRB engines that produce the actinide boost matter. Neutron star mergers, where instead a central stable or meta-stable massive neutron star survives long enough, eject very low Y_e matter in tidal ejecta together with matter that is characterized by a broad range of Y_e conditions due to the exposure to the intense neutrino field. Such remnants may be responsible for the more regular *r*-process enriched stars. In this picture, GW170817 could have produced the early blue component by polar dynamical ejecta together with neutrino-driven winds from initial stages where a massive neutron star was still present. The ensuing collapse would have triggered the GRB launch, the torus would regulate itself to $Y_e \sim 0.1$, eject a fair fraction of this material in the form of actinides which would be consistent with the decay time scales inferred from late time observations of AT2017gfo (Wu et al. 2019; Kasliwal et al. 2022). Opposite to the earlier discussed BH-torus systems (NS-BH mergers, collapsars), here the early phases related to dynamical ejecta and the neutrino-driven wind (during the period when a meta-stable massive neutron star still existed, before turning into a black hole) contribute sizable fractions of the ejecta and lead to a broad range of Y_e-values, less dominated by the narrow interval responsible for an actinide boost.

Thus, after having gone through the options of category III events, which lead to a strong *r*-process, it seems that we found two types of subclasses: category IIIa, probably including neutron star mergers with combined masses which permit the formation of a stable or meta-stable massive neutron star for extended times after the merger and during the matter ejection and neutrino wind phase. In addition, a subdivided subclass of category IIIb events seems to include black hole torus systems (with massive neutron star binaries leading to fast black hole formation, neutron star – black hole mergers, and collapsars or hypernovae from very massive single stars). The latter would tend to be characterized by an actinide boost, while IIIa events would produce a strong *r*-process as well, but no actinide boost.

After this attempt of trying to identify the possible astrophysical sources for the different categories of events, deduced from abundance observations of low metallicity stars, we address more quantitative aspects with respect to linking the here discussed category IIIa and IIIb events to the different subregimes of *r*-process enriched stars of regime 3. This leads to the question of the dominance of the abundances observed in r-I and r-II stars due to category IIIa and IIIb events.

It remains to be seen how the subregimes r-I and r-II of regime 3 stars can be explained with category IIIa and IIIb events. In Fig. 16 we have shown that Th in complete *r*-process stars of regime 3 comes from two distinct event categories which essentially coincide with regime r-I and r-II stars. Figure 19 underlined, in addition, that yet another superposition is necessary to explain the Eu abundances in r-I and r-II stars, and we concluded that the limited-r or weak *r*-process events of category I/II have to contribute as well. In Tables 7 and 8 we attempted to quantify this contribution. While both category IIIa and IIIb events are expected to have either no coproduction of Fe at all or a negligible coproduction (in comparison to solar Fe/Eu), nevertheless, we see a scattered relation between Eu and Fe in r-I and r-II stars (see Fig. 20). The average ratios for Eu/Fe of 3×10^{-7} and 3×10^{-6} determined from the sample of r-I and r-II stars, correspond to a mean [Eu/Fe] value for these subregimes. It is not clear how such ratios could be obtained for example in collapsars and hypernovae, or how such values could be obtained with the Eu input from neutron star mergers. We take these two cases: (i) collapsar input from Siegel et al. (2019), (ii) the average Eu ejecta from neutron star mergers Côté et al. (2017). They are not necessarily accompanied by ejected Fe. We discussed before whether neutron star kicks avoid that the merger ejecta are mixed with the preceding supernova remnants (containing Fe) or the merger takes place within the remnant material, polluted by the Fe ejecta of $0.1\, M_\odot$ from the two preceding core-collapse supernovae (producing the two neutron stars) (Ebinger et al. 2020; Curtis et al. 2019).

The collapsar models of Siegel et al. (2019) predict $>10^{-1}\, M_\odot$ of *r*-process matter and typically about $0.5\, M_\odot$ of ^{56}Ni (decaying to Fe). This leads to about $10^{-4}\, M_\odot$ of Eu, an Eu/Fe mass fraction ratio of 2×10^{-4}, and an abundance ratio of 7.4×10^{-5}. For neutron star mergers the typical Eu ejecta mass is $10^{-5}\, M_\odot$ (Côté et al. 2017). If we would assume that this Eu is ejected into the interstellar matter polluted already with the ejecta of the preceding two supernovae, this would amount to about $0.2\, M_\odot$ of Fe. In the opposite case the ISM, into which the Eu is ejected, would not be polluted by the Fe of the prior supernovae from the preceding binary system, but it could contain Fe from other independent prior supernova events. Let us, for the moment, just assume the mixing with $0.1\, M_\odot$ of Fe from one supernova, independent of its origin, just to get an idea of the Eu/Fe ratio resulting from such an assumption. This leads to an Eu/Fe mass ratio of 10^{-4} or an abundance ratio of 3.7×10^{-5}. If we follow the previous discussion that r-II stars are related to an actinide boost and an actinide boost is related to black hole torus systems, then the r-II observations should be compared to the collapsar case, which leaves the neutron star mergers to be related to r-I stars (but keeping in mind that according to Table 7 category II events, i.e., core-collapse with Fe coproduction contribute as well, and are more frequent than compact binary mergers).

If we take the resulting ratios at face value, the observed ratio of Eu/Fe is 25 times smaller than in the produced ejecta for the collapsar case and 123 times smaller than in the ejecta (if including Fe from one supernova) for the neutron star merger case. Thus, one would need to add additional Fe from other preceding core-collapse supernovae. This would require $n \times 0.1\, M_\odot$ of Fe from additional supernovae to obtain $(0.5 + n \times 0.1) = 25 \times 0.5$ for the collapsar case and $(0.1 + n \times 0.1) = 123 \times 0.1$ for the neutron star merger case. This results in $n_{\rm coll} = 120$ and $n_{\rm NSM} = 122$ times $0.1\, M_\odot$ of additional Fe from preceding core-collapse supernovae in order to arrive at the observed ratios. This would require in both cases the Fe of about 120 additional supernovae.

Turning it around means that on average the ISM, out of which r-I as well as r-II stars formed, experienced 1 category IIIa

[6] But see for example Mösta et al. (2020) for a possible alternative.

Table 10. Observed element ratios versus astrophysical events.

Element ratio	Obs. average r-I	Obs. average r-II	Neutron star mergers (when including Fe from one SN)	Collapsars
Eu/Fe	3×10^{-7}	3×10^{-6}	3.7×10^{-5}	7.4×10^{-5}

Notes. Candidates for category IIIa and IIIb events for complete *r*-process stars of regime 3.

or IIIb event combined with about 120 core-collapse supernova events, producing each 0.1 $M_\odot$ of Fe. This stands for about eight per mil of either category IIIa or IIIb events in comparison to the number of core-collapse supernovae and is nicely consistent with our previous considerations related to Fig. 21. On the one hand the large scatter in the observed ratios of the order 10 to 20, indicates the inhomogeneity of matter in the early galaxy. Nevertheless, the result also shows that at the low metallicities considered here, we apparently do see the imprint of about one category III event mixed into an ISM containing already the pollution of about 120 core-collapse supernovae. When looking at Fig. 2 from Rosswog et al. (2017), the ratio $n_{\rm NSM} = 122$ is consistent with the requirements for dominant *r*-process producing events that eject about $10^{-2}\,M_\odot$ of *r*-process matter per event. On other hand, if one would try to explain the strong *r*-process of solar abundances only by collapsars the ratio of $n_{\rm coll} = 120$ is somewhat on the low side for events which eject about $0.5\,M_\odot$ of *r*-process matter per event. A number of about 500 would be rather required. However, when considering that in total r-enriched stars would result from a combination of compact binary mergers and collapsars, and that the actinide-boost stars (r-II) are only a fraction of all r-enriched stars (≈25%), this would fit perfectly. We should notice that Fig. 2 from Rosswog et al. (2017) looks at the overall statistics in order to explain solar system *r*-process abundances. The attempt of identifying alternatively collapsars with r-I stars and neutron star mergers with r-II stars would lead to numbers which do not necessarily exclude these interpretations, but the taken choice looks more reasonable.

7. Concluding discussion

We have utilized statistical methods (correlations, cluster analysis, and rank tests, see Appendices A–C) for *r*-process elemental abundance patterns in low metallicity stars with [Fe/H] < −2.5. They test the coproduction of elements in nucleosynthesis events, whether certain patterns stem from different types of events, and how many different events contributed to the observed abundances of individual chemical elements. Our initial approach was based on the assumption that at such low metallicities, only the imprint of a single nucleosynthesis event can bee seen, coproducing elements in specific abundance ratios. Such an analysis goes back to findings by Ryan et al. (1996), for example, that already one core-collapse supernova leads to a remnant metallicity of [Fe/H] = −2.7 in a previously pristine interstellar medium. This sets the stage for the first generation of stars, which, if going back to the pollution by the same type of events, would lead to high correlations between element abundances (see Appendix A). If at early stages already several (possibly different) explosive events have enriched the ISM locally, and the ISM is not yet fully mixed, one would see pockets of abundance features, also visible as clusters in abundance patterns (Appendix C). Analyzing such pockets separately permits one to also interpret correlations of two elements as a coproduction. The situation is more complicated when already several explosive events have contributed to the protostellar cloud of a single newborn star, for instance several core-collapse supernovae have enriched the gas, but also an additional *r*-process event. In such situations, the relation between element abundances and their ranks, described in Appendix B, can provide information on the number of contributing sites and their element abundance features. The analysis of observed abundance patterns by means of such statistical tools has led us to suggest four to five different *r*-process sites. In a slightly speculative, but promising, manner we identify these with the following:

1. Category 0 events are regular core-collapse supernovae. They can contribute, with a possible combination of a very weak *r*-process and a *νp*-process, to trans-Fe elements (possibly not much beyond Sr, Y, and Zr, in any case ending with the second *r*-process peak). This follows, for example, from an analysis of Fig. 3 (right panel) in comparison to Fig. 13. In the first case we see for Eu high or relatively high correlations with Fe for [Eu/Fe] values in the range between the stars HD 122563 and HD 115444, which indicates a coproduction of Fe and Eu in specific and special core-collapse supernova events where HD 122563 marks the lowest observed Eu/Fe ratio. Opposite to this behavior, one can notice in Fig. 13 Sr/Fe or Zr/Fe ratios with a high correlation to Fe even below HD 122563, indicating an even weaker *r*-process or alternative events which produce light trans-Fe elements. We identified them with regular core-collapse supernovae, that is category 0 events.
2. Category I events always coproduce Eu together with Fe in an apparently unique way, but under weak *r*-process conditions. Our initial idea was that EC supernovae would be a good candidate, although their occurrence has been put into question (but not definitely ruled out) with recent electron-capture data on ^{20}Ne. However, they have problems in producing sufficient amounts of Eu for realistic $Y_{\rm e}$ values. An alternative site could be QD supernovae, which (if the chosen equation of state properties are realistic) derive from a narrow initial mass region of massive stars and would thus lead to a very narrow range of explosion conditions. This would be consistent with the observed tight correlation between Eu and Fe; for more details, readers can refer to Figs. 8a and 9 (left panel) and the discussions related to Table 9.
3. Category II events stand for another weak or limited *r*-process site. A strong candidate are magnetorotational supernovae which, dependent on precollapse rotation and magnetic fields, can produce quite varying *r*-process abundances, but with average Sr/Eu ratios consistent with weak *r*-process patterns. This would be in line with the observed large scatter in Fig. 9 (right panel) and the rank relation in Fig. 8b. Both category I and category II events are chiefly responsible for limited-r or r-poor stars in regime 1 with [Eu/Fe] < −0.3 and regime 2 with [Eu/Fe] < 0 (see Fig. 3, right panel and the high Sr/Fe ratios in Fig. 2, right panel).
4. Category III events consist of strong *r*-process sites which produce all heavy elements up to the third *r*-process peak and the actinides. Neutron star mergers surely belong to this category. Further options are neutron star – black hole mergers.

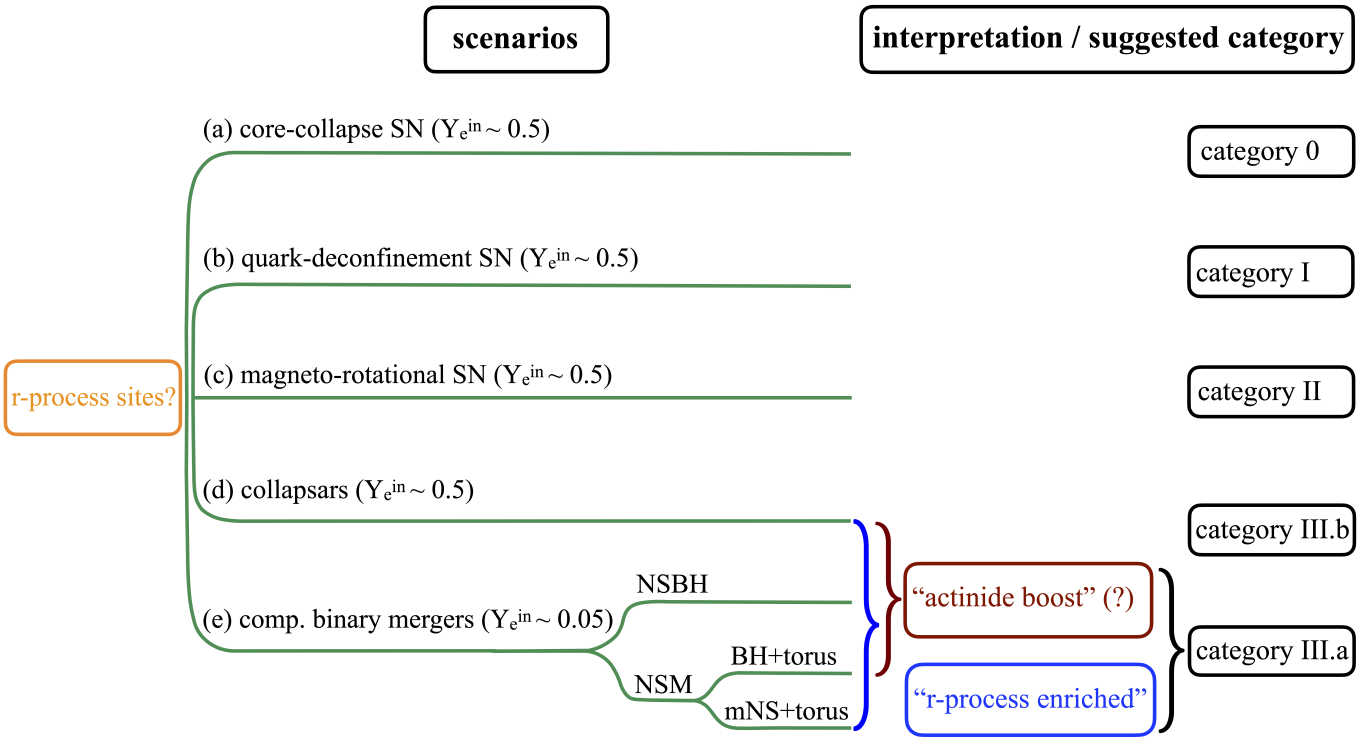

Fig. 25. Linking the star categories to their origins. Suggested event categories which are responsible for the observed limited-r (regime 1 and 2) and *r*-process enriched (regime 3 with subregimes r-I and r-II) stars. There is a close connection to the event categories I, II, and IIIa and IIIb, although there is not a one-to-one connection. This is due to the fact that the observational regimes are determined by [Eu/Fe] intervals (<-0.3, <0, <1, and >1, which are not only determined by the ejecta of event categories, but also due to inhomogeneous ejecta mixing with the ISM in the early Galaxy. While the actinides (e.g., Th) are only found in r-I and r-II stars and only produced in category IIIa and IIIb events, lanthanides and rare earth elements also have various contributions from category I and II events. Among the compact binary mergers, all systems that contain a black hole initially or lead to fast black hole formation with BH accretion tori fall into category IIIb, while those that contain a stable or meta-stable massive neutron star for a long duration fall into category IIIa. The initial Y_e^{in} (before collapse or merger) is indicated as well, but is altered due to weak interactions during the explosive events.

Also, there exists evidence that at low metallicities, a site related to massive single stars contributes as well. We categorize the compact binary options as IIIa and the massive collapsing star option as IIIb. A further question exists as to how actinide boost stars fit into this scheme. Our suggestion is that those sites that quickly lead to a black hole accretion disk system and are not too affected by neutrino winds (increasing Y_e) are the best candidates for actinide boost events which can be largely found in observations of r-II stars. The motivation behind this suggestion is that these events have a good physical reason to preferentially produce matter in the required electron fraction range of $Y_e \approx 0.10$–0.15; readers can refer to the discussion in Sect. 6.3.2 for more details. Such events include collapsars and hypernovae, neutron star – black hole mergers, and also neutron star mergers which lead to an early black hole formation, rather than a stable or meta-stable massive neutron star. The regular neutron star mergers (category IIIa) seem to be dominantly related to r-I-stars, while r-II stars are primarily related to category IIIb events, that is systems with black hole accretion disk tori (see Figs. 15, 16, and Table 6).

We combined all items, given above, in a display of all suggested event categories that can provide an explanation for the observed abundance patterns in low metallicity stars (Fig. 25). This also includes category 0 regular core-collapse supernovae which only contribute Fe and trans-Fe element events, but no heavy *r*-process elements. Besides this attempt to identify the four to five categories 0, I, II, and IIIa and b of stellar explosive events which contribute to weak and strong *r*-process nucleosynthesis, we found further constraints for these events:

- We found two good reasons to move the division between limited-r and r-enriched stars (in our terminology between regime 2 and 3) down from [Eu/Fe] = 0.3 to 0. This is based (a) on the existence of Th in stars with [Eu/Fe] > 0 (see Fig. 11, left panel) and (b) the best reproduction of the Eu versus Fe correlation curve in Fig. 21.
- We also found that the category III strong *r*-process events make up in number for about six per mil of all core-collapse supernovae. This is consistent with findings for the frequency of binary merger events in comparison to CCSNe, based on Fig. 21. A similar result was obtained from Table 10, hinting at the fact that r-I stars are dominated by neutron star merger events, but the ISM out of which the stars formed had already been previously polluted by ≈120 core-collapse category 0 events, that is mergers would amount to an eight per mil contribution.
- In a similar way we analyzed the Eu and Fe contributions to r-II stars and their relation to collapsars, standing for category IIIb. Here we found a similar result of about 120 core-collapse supernova (category 0) contributions to each collapsar event (see also Table 10). This is a bit on the low side to explain solar system r-abundances if such hypernovae, typically ejecting $10^{-1}\,M_\odot$ of *r*-process matter or $10^{-4}\,M_\odot$ of Eu, would be the only source of strong *r*-process

elements (see Rosswog et al. 2017). In that case, a level of about 500 would be needed. However, from our analysis with respect to actinide-normal versus actinide-boost abundance patterns (essentially related to observed r-I and r-II stars), we know that this contribution is not the dominant one in strong *r*-process elements. Therefore, this constraint is not required and the result is consistent with observations.

– Finally we found constraints for the limited-r stars of our regimes 1 and 2 and the connection to category I and II contributions. If one identifies category I events with QD supernovae, which should occur in a very narrow mass range, we find that their ejecta had to mix with those of about 500 prior supernovae in order to explain the very linear, that is to say high correlations of Eu versus Fe in regime 1. If one identifies category II events with highly variable magnetorotational supernova contributions, a mix with as low as ten regular category 0 supernovae could be realistic, which would be consistent with the fraction of magnetars resulting from core-collapse events (see Table 9).

All these conclusions sound reasonable, supporting our "guided speculations" to be quite convincing suggestions for possible, different *r*-process contribution, giving a consistent explanation of existing observations. Nevertheless, an important question has been raised as to how, in low metallicity, star correlations support the interpretation of a coproduction of elements and point to the pollution by a single event. While, based on the early findings of Ryan et al. (1996), a single supernova (our category 0 event) would already lead to an [Fe/H] close to −2.5 to −3 in its remnant (and if a neighboring star forming region is polluted, this would probably lead to an even smaller Fe contribution), the early suggestion was that for these lower metallicities one sees abundance properties for elements X and Y which go back to a single event, where they have been coproduced. Depending on varying degrees of admixtures to new-born stars, the total amounts of X and Y might vary, but the ratios X/Y should stay the same, which can be seen in strong correlations of these elements which point to their coproduction in the same event. We started out with this initial hypothesis (see also Frebel 2018; Yong et al. 2021), but permitted a continuously evolving interpretation during our analysis, based on emerging and more detailed knowledge, when passing through Sects. 2.1, 3.1, 3.3, 3.5, 4.2, and 6. The aspect is important since it provides the major argument for the coproduction of Fe and Eu in specific events (specific types of core-collapse supernovae of category I and II, and probably about one-tenth of the whole population which, via their magneto-rotational origin, leads to magnetars). However, the question of supporting the claim of correlation and coproduction of Fe and Eu needs to be addressed, arguing for these specific events independent of compact binary mergers or other rare events of category III if more than 90% of the Fe originates from regular core-collapse supernovae of category 0 on average. This also relates to another question of whether the occurrence of high correlations in a narrow [Eu/Fe] range between −0.5 and 0−0.3 (see Fig. 3, right panel) is not automatically the result of considering only this small range in [Eu/Fe], leading to very similar Eu/Fe ratios and possibly appearing as a false correlation.

There are a number of arguments which, however, support our claims: (a) with statistical means also the correlation of X versus Y with a small fraction of Y being statistically sound. (b) Following the lines above, Fe from the first regular core-collapse supernovae (category 0) already leads to [Fe/H] close to −3 in the remnant and in polluted nearby star forming regions, possibly admixing 10, 1, or only 0.1%, and can go down to [Fe/H] = −6, actually representing stars with the lowest found metallicity. Then one can expect that close to −3, the Fe content is already an average value due to regular core-collapse supernovae. If an additional weak *r*-process event (rarer by at least a factor of 10 for QD and magneto-rotational supernovae – category I and II – than for regular core-collapse supernovae – category 0) then contributes the first Eu jointly with Fe, this would have a higher impact not only (and clearly) in Eu but also in Fe. (c) The highly different behavior of limited-r stars due to their vastly higher Sr/Fe ratios in comparison to r-I and r-II stars (Fig. 2 , right panel) points, without a doubt, to a clearly different class of sources. (d) This can also be seen in the cluster analysis of Fig. 4 (right panel). (e) And finally, the rank test for Fe (Fig. 7, right panel) shows a close to dominant linear behavior, underlining one major source (core-collapse supernovae, category 0). However, the positive deviation at low Fe ranks points to an additional source with small Fe contributions (magneto-rotational supernovae, our category II, a polluter for limited-r stars). On the side, the positive deviation at high ranks points to a class of heavy Fe polluters (potentially collapsars, our category IIIb), which, due to their high Eu/Fe ratio in comparison to solar values, do nevertheless suppress a correlation of Fe and Eu (as was also found for our categories IIIa – neutron star mergers – as well as IIIb – collapsars). Adding all these points from (a) to (e), we think that they provide strong support for the interpretation we give in the present paper. There is one exception: In the cluster analysis of Fig. 4 (right panel), we could not identify separate clusters among limited-r stars, which would relate to regimes 1 and 2 in Fig. 3 (right panel), which led to our introduction of category I (QD supernovae) and II (magneto-rotational supernovae). Therefore, the division into regimes 1 and 2 might still be preliminary and it has to be explored further.

As opposed to the doubts raised above, which required a more elaborate effort to be eliminated, the interpretation of complete *r*-process stars (our regime 3 with subregimes r-I and r-II) is much easier. First of all, they clearly show no correlation of Fe and Eu (or other *r*-process elements), pointing to sources with no or (negligible) Fe with respect to solar proportions for Fe/Eu, our category III. The introduction of r-I and r-II regimes, initially introduced by observers, is not only a formal division, but it relates to probably two different origins, as supported by the cluster analysis of Fig. 4 (right panel), though it is also due to the rank tests of Figs. 10 (right panel) and 16. There exist a number of investigations which relate an actinide boost to nucleosynthesis conditions with a specific Y_e in the range of 0.1−0.15. These prevail in the outflows of black hole accretion disks, while neutron star mergers (our category IIIa) experience a larger range of variation (including higher Y_e values in the neutrino wind and also lower values in the ejected tails consisting of pristine neutron star matter) providing a different, that is to say normal, pattern. Such black hole accretion disk outflows occur in collapsars (our category IIIb) as well as massive neutron star mergers where a black hole is formed almost instantaneously after the merger, avoiding a long period of a stabilized central massive neutron star (until its cooling and deleptonization). Thus, there is ample evidence that r-I and r-II stars really have a different origin.

These findings provided the motivation for further thorough investigations to test them with model predictions for the nucleosynthesis of such sources in Sects. 6.3.1 and 6.3.2. These tests led to a consistent picture with contributions of those sources

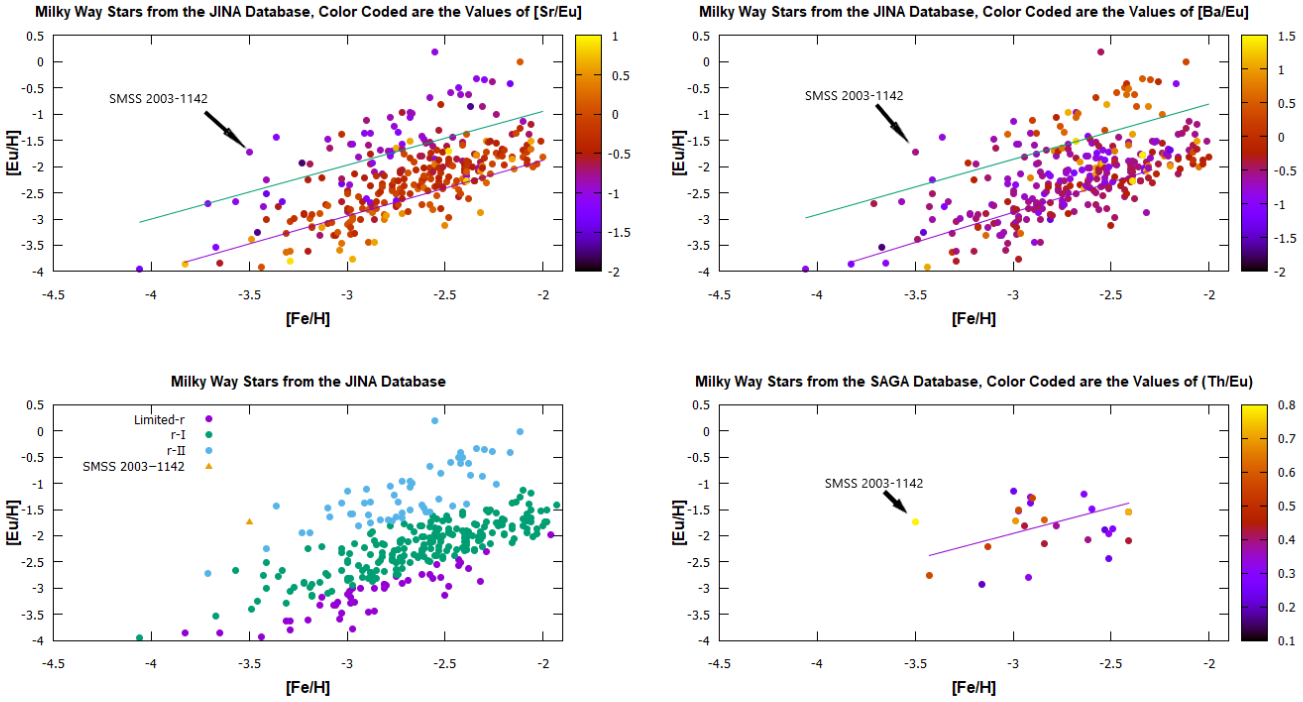

Fig. 26. Properties of low metallicity limited-r, r-I, and r-II stars with [Fe/H] < −2 with respect to [Eu/Fe] versus [Fe/H]. *Bottom left*: division into the three subregimes. *Top left*: color-coded with [Sr/Eu]. *Bottom right*: color-coded with [Th/Eu] (for those stars with detected Th). *Top right*: color-coded with respect to [Ba/Eu]. The recent observation of SMSS J200322.54−114203.3 by Yong et al. (2021) is also included.

discussed in the literature (magnetorotational supernovae, compact binary mergers, and collapsars), while the suggested QD-supernovae might require further tests. Overall, these suggestions are an attempt to bring some structure to the present understanding of the role of different *r*-process sites with the help of statistical methods and observed abundance patterns.

This analysis can be concluded with another interesting graph, supporting our interpretations from Fig. 25. In Fig. 26 we include [Eu/H] versus [Fe/H] plots for low metallicity stars from the SAGA database in the range [Fe/H] < −2, separating the limited-r, r-I, and r-II stars with lines. The bottom left plot shows only the separation into the three categories of stars, with the side effect that apparently the metallicity at the time of first occurrence seems to delay in steps from limited-r to r-I and r-II stars, but it is still unclear whether these regimes are really related to different nucleosynthesis contributing sources or not. The limited-r stars, although showing the lowest (and thus hardest to detect) Eu content, extend to the lowest metallicities, while the higher Eu content baring r-I and r-II stars (which would be easier to detect at lowest metallicities) come in in a delayed fashion. When looking at the Sr/Eu color-coded figure (top left), it indicates that especially the limited-r stars show a highly supersolar Sr/Eu ratio, while the r-II stars show a strongly subsolar ratio and the r-I stars show a close to solar (or moderately subsolar) ratio, permitting the later *s*-process contributions to Sr at higher metallicities to approach the solar ratio. This substantially different behavior (also shown in Fig. 2, right panel, of this paper) points to apparently different stellar nucleosynthesis sources (and not only a formal division in Eu/Fe categories). The bottom right insert displays color-coded Th/Eu ratios in those stars where Th was detected. The supersolar (or actinide-boost) behavior strongly prevails in the r-II stars and the upper end of the r-I stars. This supports our interpretation, based on Table 6, Figs. 15 and 16, and the comparison analysis of different model sources given in Sects. 6.3.1 and 6.3.2. We also added a figure with color-coding of Ba/Eu (top right). As Eu essentially originates from the *r*-process while Ba has a strong *s*-process contribution, solar Ba/Eu contains an $s+r/r$ comparison. In our figure we see, especially above −2.5, an apparently strong Ba contribution, but also to some extent at lower metallicities, which could be interpreted to result from an *s*-process origin. This might be due to primary *s*-process sources of fast rotating and very massive "spin stars" which, due to rotational mixing, produce primary ^{14}N and ^{22}Ne (Frischknecht et al. 2012, 2016; Cescutti et al. 2013; Choplin & Hirschi 2020). Such objects are ideal candidates for collapsars, further supporting our interpretation of r-II stars. This leaves, however, also the interpretation open that Ba here goes back to a strong *r*-process. The transition of *r*-process to the dominant *s*-process contributions from low and intermediate mass stars seems to occur only around [Fe/H] = −1 to −1.5 from the figures in Battistini & Bensby (2016). We also added new observational results of a recent observation by Yong et al. (2021) for SMSS J200322.54−114203.3, which fits perfectly into our interpretation scheme, identifying the *r*-process contribution by a hypernova and collapsar; however, we would interpret the Fe abundance differently, in line with the above discussion.

As a final point, we would like to emphasize that all the effects discussed in the paper can be explained with an early inhomogeneous picture, where abundance patterns of low(est) metallicity stars witness the ejecta composition of individual events (with a scatter dependent on the variation in the ejecta sources). Dependent on the number of different sources, this scatter can be small (e.g., for an alpha element such as Mg, essentially only CCSNe need to be considered; and even when passing through the whole IMF, only a variation by about a factor of 5 applies). This scatter can, on the contrary, also be very

extended (e.g., over two orders of magnitude for *r*-process Eu from specific supernovae to neutron star mergers and collapsars). During the evolution of galaxies, one observes a converging behavior with a strongly decreasing scatter based on values which result from a statistical mix of all combined sites. Only if one site absolutely dominates the production of a specific element is that converged line an extension of the average values for that specific site at low metallicities. In general, this converged line is located at a position determined by the statistical average of all sites. This difference in the behavior of alpha elements and *r*-process elements is discussed in detail in Appendix D.

Acknowledgements. The investigations of this paper would not have been possible without the publicly available observational SAGA and JINA data bases (Suda et al. 2008; Abohalima & Frebel 2018), and we want to express out thanks to the authors of these tremendous research resources. We also thank very many friends and colleagues who have worked with us on interdisciplinary *r*-process research in the past (from nuclear structure, via astrophysical modeling and abundance observations to cosmochemistry), and thus helped to lay out the foundations to the present paper. We thank especially Chiaki Kobayashi, Freeke van de Voort, Marco Pignatari, Chris Fryer, Erika Holmbeck, Enrico Ramirez-Ruiz, and Nikos Prantzos for their helpful and positive comments as well as very constructive interactions after we put our preprint on the arXiv and presented the results at the ECT* workshop "Probing Nuclear Physics with Neutron Star Mergers" and at the Carpathian Summer School of Physics in Sinaia. We thank the referee for his or her very careful reading of the manuscript, for spotting some logical glitches in the original version, and for suggesting a presentation which led to Fig. 26. Furthermore, the COST actions ChETEC (Chemical Elements as Tracers of the Evolution of the Cosmos, CA16117), GWvese (Gravitational waves, black holes and fundamental physics, CA16104), and Pharos (The multi-messenger physics and astrophysics of neutron stars, CA16214) provided an inspiring atmosphere for thoughts along the lines discussed here. S.R. has been supported by the Swedish Research Council (VR) under grant numbers 2016-03657_3 and 2020-05044, by the Swedish National Space Board under grant number Dnr. 107/16, the research environment grant "Gravitational Radiation and Electromagnetic Astrophysical Transients (GREAT)" funded by the Swedish Research council (VR) under Dnr. 2016-06012 and by the Knut and Alice Wallenberg Foundation (KAW 2019.0112).

References

Abbott, B. P., et al. (LIGO Scientific Collaboration and Virgo Collaboration) 2017, Phys. Rev. Lett., 119, 161101
Abbott, B. P., Abbott, R., Abbott, T. D., et al. 2020, ApJ, 892, L3
Abohalima, A., & Frebel, A. 2018, ApJS, 238, 36
Akram, W., Farouqi, K., Hallmann, O., & Kratz, K.-L. 2020, Eur. Phys. J. Web Conf., 227, 01009
Arcones, A., & Montes, F. 2011, ApJ, 731, 5
Arcones, A., & Thielemann, F.-K. 2013, J. Phys. G: Nucl. Part. Phys., 40, 013201
Arlandini, C., Käppeler, F., Wisshak, K., et al. 1999, ApJ, 525, 886
Arnould, M., Goriely, S., & Takahashi, K. 2007, Phys. Rep., 450, 97
Asplund, M., Grevesse, N., Sauval, A. J., & Scott, P. 2009, ARA&A, 47, 481
Audouze, J., & Silk, J. 1995, ApJ, 451, L49
Balbus, S. A., & Hawley, J. F. 1998, Rev. Mod. Phys., 70, 1
Barklem, P. S., Christlieb, N., Beers, T. C., et al. 2005, A&A, 439, 129
Battistini, C., & Bensby, T. 2016, A&A, 586, A49
Bauswein, A., Just, O., Janka, H.-T., & Stergioulas, N. 2017, ApJ, 850, L34
Behroozi, P. S., Ramirez-Ruiz, E., & Fryer, C. L. 2014, ApJ, 792, 123
Beloborodov, A. M. 2003, ApJ, 588, 931
Benacquista, M. J., & Downing, J. M. B. 2013, Liv. Rev. Relativ., 16, 4
Beniamini, P., & Piran, T. 2016, MNRAS, 456, 4089
Beniamini, P., Hotokezaka, K., & Piran, T. 2016, ApJ, 832, 149
Beniamini, P., Hotokezaka, K., van der Horst, A., & Kouveliotou, C. 2019, MNRAS, 487, 1426
Bollig, R., Yadav, N., Kresse, D., et al. 2021, ApJ, 915, 1685
Bonifacio, P., Monai, S., & Beers, T. C. 2000, AJ, 120, 2065
Bugli, M., Guilet, J., Obergaulinger, M., Cerdá-Durán, P., & Aloy, M. A. 2020, MNRAS, 492, 58
Burbidge, E. M., Burbidge, G. R., Fowler, W. A., & Hoyle, F. 1957, Rev. Mod. Phys., 29, 547
Cameron, A. G. W. 1957, Stellar Evolution, Nuclear Astrophysics, and Nucleogenesis (Chalk River: Dover Publications)
Cameron, A. G. W. 2003, ApJ, 587, 327
Cescutti, G., Chiappini, C., Hirschi, R., Meynet, G., & Frischknecht, U. 2013, A&A, 553, A51
Cescutti, G., Romano, D., Matteucci, F., Chiappini, C., & Hirschi, R. 2015, A&A, 577, A139
Chandrasekhar, S. 1960, Proc. Natl. Acad. Sci., 46, 253
Chen, W., & Beloborodov, A. M. 2007, ApJ, 657, 383
Choplin, A., & Hirschi, R. 2020, J. Phys. Conf. Ser., 1668, 012006
Coryell, C. D. 1953, Annu. Rev. Nucl. Part. Sci., 2, 305
Coryell, C. D. 1961, J. Chem. Edu., 38, 67
Côté, B., Belczynski, K., Fryer, C. L., et al. 2017, ApJ, 836, 230
Côté, B., Yagüe, A., Világos, B., & Lugaro, M. 2019, ApJ, 887, 213
Cowan, J. J., & Thielemann, F.-K. 2004, Phys. Today, 57, 47
Cowan, J. J., Thielemann, F.-K., & Truran, J. W. 1991, Phys. Rep., 208, 267
Cowan, J. J., Pfeiffer, B., Kratz, K.-L., et al. 1999, ApJ, 521, 194
Cowan, J. J., Sneden, C., Beers, T. C., et al. 2005, ApJ, 627, 238
Cowan, J. J., Sneden, C., Lawler, J. E., et al. 2021, Rev. Mod. Phys., 93, 015002
Curtis, S., Ebinger, K., Fröhlich, C., et al. 2019, ApJ, 870, 2
Dan, M., Rosswog, S., Guillochon, J., & Ramirez-Ruiz, E. 2011, ApJ, 737, 89
Dan, M., Rosswog, S., Guillochon, J., & Ramirez-Ruiz, E. 2012, MNRAS, 422, 2417
Dessart, L., Ott, C. D., Burrows, A., Rosswog, S., & Livne, E. 2009, ApJ, 690, 1681
Ebinger, K., Curtis, S., Ghosh, S., et al. 2020, ApJ, 888, 91
Eichler, M., Nakamura, K., Takiwaki, T., et al. 2018, J. Phys. G: Nucl. Part. Phys., 45, 014001
Eichler, M., Sayar, W., Arcones, A., & Rauscher, T. 2019, ApJ, 879, 47
Evans, P. A., Cenko, S. B., Kennea, J. A., et al. 2017, Science, 358, 1565
Everitt, B. S., Landau, S., Leese, M., & Stahl, D. 2011, Cluster Analysis, 5th Edition, Wiley Series in Probability and Statistics (New York: Wiley)
Ezzeddine, R., Rasmussen, K., Frebel, A., et al. 2020, ApJ, 898, 150
Farouqi, K., Kratz, K. L., Cowan, J. J., et al. 2008, in First Stars III, eds. B. W. O'Shea, & A. Heger, AIP Conf. Ser., 990, 309
Farouqi, K., Kratz, K. L., & Pfeiffer, B. 2009, PASA, 26, 194
Farouqi, K., Kratz, K., Pfeiffer, B., et al. 2010, ApJ, 712, 1359
Fernández, R., Tchekhovskoy, A., Quataert, E., Foucart, F., & Kasen, D. 2019, MNRAS, 482, 3373
Fischer, T., Guo, G., Dzhioev, A. A., et al. 2020a, Phys. Rev. C, 101, 025804
Fischer, T., Wu, M.-R., Wehmeyer, B., et al. 2020b, ApJ, 894, 9
Foucart, F., O'Connor, E., Roberts, L., et al. 2016, Phys. Rev. D, 94, 123016
François, P., Depagne, E., Hill, V., et al. 2007, A&A, 476, 935
Frebel, A. 2018, Annu. Rev. Nucl. Part. Sci., 68, 237
Frebel, A., & Norris, J. E. 2015, ARA&A, 53, 631
Freiburghaus, C., Rembges, J.-F., Rauscher, T., et al. 1999a, ApJ, 516, 381
Freiburghaus, C., Rosswog, S., & Thielemann, F.-K. 1999b, ApJ, 525, L121
Frischknecht, U., Hirschi, R., & Thielemann, F. K. 2012, A&A, 538, L2
Frischknecht, U., Hirschi, R., Pignatari, M., et al. 2016, MNRAS, 456, 1803
Fröhlich, C., Martínez-Pinedo, G., Liebendörfer, M., et al. 2006, Phys. Rev. Lett., 96, 142502
Ghosh, S., Wolfe, N., & Fröhlich, C. 2022, ApJ, 929, 43
Goldstein, D. A., & Kasen, D. 2018, ApJ, 852, L33
Grichener, A., Kobayashi, C., & Soker, N. 2022, ApJ, 926, L9
Grimmett, J. J., Karakas, A. I., Heger, A., Müller, B., & West, C. 2020, MNRAS, 496, 4987
Halevi, G., & Mösta, P. 2018, MNRAS, 477, 2366
Hansen, C. J., & Primas, F. 2011, A&A, 525, L5
Hansen, C. J., Primas, F., Hartman, H., et al. 2012, A&A, 545, A31
Hansen, C. J., Andersen, A. C., & Christlieb, N. 2014a, A&A, 568, A47
Hansen, C. J., Montes, F., & Arcones, A. 2014b, ApJ, 797, 123
Hansen, T. T., Holmbeck, E. M., Beers, T. C., et al. 2018, ApJ, 858, 92
Hayek, W., Wiesendahl, U., Christlieb, N., et al. 2009, A&A, 504, 511
Haynes, C. J., & Kobayashi, C. 2019, MNRAS, 483, 5123
Hempel, M., & Schaffner-Bielich, J. 2010, Nucl. Phys. A, 837, 210
Hill, V., Plez, B., Cayrel, R., et al. 2002, A&A, 387, 560
Hill, V., Christlieb, N., Beers, T. C., et al. 2017, A&A, 607, A91
Hillebrandt, W. 1978, Space Sci. Rev., 21, 639
Hoffman, R. D., Woosley, S. E., & Qian, Y.-Z. 1997, ApJ, 482, 951
Holmbeck, E. M., Beers, T. C., Roederer, I. U., et al. 2018, ApJ, 859, L24
Holmbeck, E. M., Sprouse, T. M., Mumpower, M. R., et al. 2019, ApJ, 870, 23
Holmbeck, E. M., Hansen, T. T., Beers, T. C., et al. 2020, ApJS, 249, 30
Honda, S., Aoki, W., Ishimaru, Y., Wanajo, S., & Ryan, S. G. 2006, ApJ, 643, 1180
Honda, S., Aoki, W., Ishimaru, Y., & Wanajo, S. 2007, ApJ, 666, 1189
Hotokezaka, K., Piran, T., & Paul, M. 2015, Nat. Phys., 11, 1042
Hüdepohl, L., Müller, B., Janka, H.-T., Marek, A., & Raffelt, G. G. 2010, Phys. Rev. Lett., 104, 251101
Ishimaru, Y., Wanajo, S., & Prantzos, N. 2015, ApJ, 804, L35
Iwamoto, K., Brachwitz, F., Nomoto, K., et al. 1999, ApJS, 125, 439
Ji, A. P., Drout, M. R., & Hansen, T. T. 2019, ApJ, 882, 40

Jones, S., Röpke, F. K., Pakmor, R., et al. 2016, A&A, 593, A72
Just, O., Bauswein, A., Pulpillo, R. A., Goriely, S., & Janka, H.-T. 2015, MNRAS, 448, 541
Käppeler, F., Gallino, R., Bisterzo, S., & Aoki, W. 2011, Rev. Mod. Phys., 83, 157
Kasliwal, M. M., Nakar, E., Singer, L. P., et al. 2017, Science, 358, 1559
Kasliwal, M. M., Kasen, D., Lau, R. M., et al. 2022, MNRAS, 510, L7
Kilpatrick, C. D., Foley, R. J., Kasen, D., et al. 2017, Science, 358, 1583
Kirsebom, O. S., Jones, S., Strömberg, D. F., et al. 2019a, Phys. Rev. Lett., 123, 262701
Kirsebom, O. S., Hukkanen, M., Kankainen, A., et al. 2019b, Phys. Rev. C, 100, 065805
Kiuchi, K., Sekiguchi, Y., Shibata, M., & Taniguchi, K. 2009, Phys. Rev. D, 80, 064037
Kobayashi, C. 2016, in The General Assembly of Galaxy Halos: Structure, Origin and Evolution, eds. A. Bragaglia, M. Arnaboldi, M. Rejkuba, & D. Romano, IAU Symp., 317, 57
Kobayashi, C., Umeda, H., Nomoto, K., Tominaga, N., & Ohkubo, T. 2006, ApJ, 653, 1145
Kobayashi, C., Karakas, A. I., & Lugaro, M. 2020, ApJ, 900, 179
Korobkin, O., Rosswog, S., Arcones, A., & Winteler, C. 2012, MNRAS, 426, 1940
Kratz, K. L. 1988, Rev. Mod. Astron., 1, 184
Kratz, K., Bitouzet, J., Thielemann, F., Moeller, P., & Pfeiffer, B. 1993, ApJ, 403, 216
Kratz, K.-L., Pfeiffer, B., Cowan, J. J., & Sneden, C. 2004, New Astron. Rev., 48, 105
Kratz, K.-L., Farouqi, K., Pfeiffer, B., et al. 2007, ApJ, 662, 39
Kratz, K. L., Farouqi, K., Mashonkina, L. I., & Pfeiffer, B. 2008, New Astron. Rev., 52, 390
Kratz, K.-L., Farouqi, K., & Möller, P. 2014, ApJ, 792, 6
Lattimer, J. M., Mackie, F., Ravenhall, D. G., & Schramm, D. N. 1977, ApJ, 213, 225
Lee, W. H., & Ramirez-Ruiz, E. 2007, New J. Phys., 9, 17
Livio, M., & Mazzali, P. 2018, Phys. Rep., 736, 1
Lodders, K. 2020, The Oxford Research Encyclopedia of Planetary Science (Oxford: Oxford University Press)
Lodders, K., Palme, H., & Gail, H. P. 2009, Solar System, Landolt-Börnstein – Group VI Astronomy and Astrophysics (Berlin, Heidelberg: Springer-Verlag), 712
MacFadyen, A. I., & Woosley, S. E. 1999, ApJ, 524, 262
MacFadyen, A. I., Woosley, S. E., & Heger, A. 2001, ApJ, 550, 410
Macias, P., & Ramirez-Ruiz, E. 2019, ApJ, 877, L24
Maeda, K., Röpke, F. K., Fink, M., et al. 2010, ApJ, 712, 624
Maoz, D., Mannucci, F., & Nelemans, G. 2014, ARA&A, 52, 107
Martin, D., Perego, A., Arcones, A., et al. 2015, ApJ, 813, 2
Martínez-Pinedo, G., Fischer, T., Lohs, A., & Huther, L. 2012, Phys. Rev. Lett., 109, 251104
Martínez-Pinedo, G., Fischer, T., & Huther, L. 2014, J. Phys. G: Nucl. Part. Phys., 41, 044008
Mashonkina, L. I., Vinogradova, A. B., Ptitsyn, D. A., Khokhlova, V. S., & Chernetsova, T. A. 2007, Astron. Rep., 51, 903
Mashonkina, L., Christlieb, N., & Eriksson, K. 2014, A&A, 569, A43
Matteucci, F. 2012, Chemical Evolution of Galaxies, Astronomy and Astrophysics Library (Berlin, Heidelberg: Springer-Verlag)
Matteucci, F., & Greggio, L. 1986, A&A, 154, 279
McKinney, J. C., Tchekhovskoy, A., & Blandford, R. D. 2013, Science, 339, 49
McKinney, J. C., Tchekhovskoy, A., Sadowski, A., & Narayan, R. 2014, MNRAS, 441, 3177
McWilliam, A., Preston, G. W., Sneden, C., & Searle, L. 1995a, AJ, 109, 2757
McWilliam, A., Preston, G. W., Sneden, C., & Shectman, S. 1995b, AJ, 109, 2736
Metzger, B. D. 2019, Liv. Rev. Relativ., 23, 1
Metzger, B. D., Martínez-Pinedo, G., Darbha, S., et al. 2010, MNRAS, 406, 2650
Miller, J. M., Ryan, B. R., Dolence, J. C., et al. 2019, Phys. Rev. D, 100, 023008
Miller, J. M., Sprouse, T. M., Fryer, C. L., et al. 2020, ApJ, 902, 66
Mirizzi, A., Mangano, G., & Saviano, N. 2015, Phys. Rev. D, 92, 021702
Mishenina, T., Pignatari, M., Gorbaneva, T., et al. 2019, MNRAS, 489, 1697
Möller, P., Pfeiffer, B., & Kratz, K.-L. 2003, Phys. Rev. C, 67, 055802
Montes, F., Beers, T. C., Cowan, J., et al. 2007, ApJ, 671, 1685
Montes, G., Ramirez-Ruiz, E., Naiman, J., Shen, S., & Lee, W. H. 2016, ApJ, 830, 12
Mösta, P., Richers, S., Ott, C. D., et al. 2014, ApJ, 785, L29
Mösta, P., Ott, C. D., Radice, D., et al. 2015, Nature, 528, 376
Mösta, P., Roberts, L. F., Halevi, G., et al. 2018, ApJ, 864, 171
Mösta, P., Radice, D., Haas, R., Schnetter, E., & Bernuzzi, S. 2020, ApJ, 901, L37
Murguia-Berthier, A., Ramirez-Ruiz, E., Montes, G., et al. 2017, ApJ, 835, L34
Nishimura, N., Takiwaki, T., & Thielemann, F.-K. 2015, ApJ, 810, 109
Nishimura, N., Sawai, H., Takiwaki, T., Yamada, S., & Thielemann, F.-K. 2017, ApJ, 836, L21
Nomoto, K. 2017, in Nucleosynthesis in Hypernovae Associated with Gamma-Ray Bursts, eds. A. W. Alsabti, & P. Murdin (Springer International Publishing), 1931
Nomoto, K., Tominaga, N., Umeda, H., Kobayashi, C., & Maeda, K. 2006, Nucl. Phys. A, 777, 424
Nomoto, K., Kobayashi, C., & Tominaga, N. 2013, ARA&A, 51, 457
Nordlander, T., Amarsi, A. M., Lind, K., et al. 2017, A&A, 597, A6
Norris, J. E., Christlieb, N., Korn, A. J., et al. 2007, ApJ, 670, 774
Norris, J. E., Christlieb, N., Bessell, M. S., et al. 2012, ApJ, 753, 150
Ojima, T., Ishimaru, Y., Wanajo, S., Prantzos, N., & François, P. 2018, ApJ, 865, 87
Ott, U. 2017, in Isotope Variations in the Solar System: Supernova Fingerprints, eds. A. W. Alsabti, & P. Murdin, 2331
Pellin, M. J., Davis, A. M., Lewis, R. S., Amari, S., & Clayton, R. N. 1999, Lunar and Planetary Science Conference, 1969
Pellin, M. J., Savina, M. R., Calaway, W. F., et al. 2006, in 37th Annual Lunar and Planetary Science Conference, eds. S. Mackwell, & E. Stansbery, Lunar Planet. Sci. Conf., 2041
Perego, A., Rosswog, S., Cabezón, R. M., et al. 2014, MNRAS, 443, 3134
Pfeiffer, B., Kratz, K.-L., Thielemann, F.-K., & Walters, W. B. 2001, Nucl. Phys. A, 693, 282
Pol, N., McLaughlin, M., & Lorimer, D. R. 2020, MNRAS, 4, 22
Prantzos, N., Abia, C., Cristallo, S., Limongi, M., & Chieffi, A. 2020, MNRAS, 491, 1832
Pruet, J., Hoffman, R. D., Woosley, S. E., Janka, H.-T., & Buras, R. 2006, ApJ, 644, 1028
Qian, Y.-Z., & Wasserburg, G. J. 2007, Phys. Rep., 442, 237
Qian, Y.-Z., & Woosley, S. E. 1996, ApJ, 471, 331
Reichert, M., Obergaulinger, M., Eichler, M., Aloy, M. Á., & Arcones, A. 2021, MNRAS, 501, 5733
Rezzolla, L., Baiotti, L., Giacomazzo, B., Link, D., & Font, J. A. 2010, Class. Quant. Grav., 27, 114105
Roberts, L. F., Reddy, S., & Shen, G. 2012, Phys. Rev. C, 86, 065803
Roederer, I. U., Kratz, K.-L., Frebel, A., et al. 2009, ApJ, 698, 1963
Roederer, I. U., Cowan, J. J., Karakas, A. I., et al. 2010, ApJ, 724, 975
Roederer, I. U., Preston, G. W., Thompson, I. B., et al. 2014, AJ, 147, 136
Rosswog, S. 2015a, Int. J. Mod. Phys. D, 24, 1530012
Rosswog, S. 2015b, Liv. Rev. Comput. Astrophys., 1, 1
Rosswog, S., Liebendörfer, M., Thielemann, F.-K., et al. 1999, A&A, 341, 499
Rosswog, S., Piran, T., & Nakar, E. 2013, MNRAS, 430, 2585
Rosswog, S., Feindt, U., Korobkin, O., et al. 2017, Class. Quant. Grav., 34, 104001
Rosswog, S., Sollerman, J., Feindt, U., et al. 2018, A&A, 615, A132
Rozwadowska, K., Vissani, F., & Cappellaro, E. 2021, New Astron., 83, 101498
Ruiz, M., Lang, R. N., Paschalidis, V., & Shapiro, S. L. 2016, ApJ, 824, L6
Ruiz, M., Tsokaros, A., Paschalidis, V., & Shapiro, S. L. 2019, Phys. Rev. D, 99, 084032
Ryan, S. G., Norris, J. E., & Beers, T. C. 1996, ApJ, 471, 254
Sakari, C. M., Placco, V. M., Farrell, E. M., et al. 2018, ApJ, 868, 110
Schatz, H., Toenjes, R., Pfeiffer, B., et al. 2002, ApJ, 579, 626
Seeger, P. A., Fowler, W. A., & Clayton, D. D. 1965, ApJS, 11, 121
Seitenzahl, I., & Townsley, D. 2017, in Nucleosynthesis in Thermonuclear Supernovae, eds. A. W. Alsabti, & P. Murdin (Cham: Springer International Publishing)
Seitenzahl, I. R., Timmes, F. X., & Magkotsios, G. 2014, ApJ, 792, 10
Seitenzahl, I. R., Ghavamian, P., Laming, J. M., & Vogt, F. P. A. 2019, Phys. Rev. Lett., 123, 041101
Sekiguchi, Y., Kiuchi, K., Kyutoku, K., Shibata, M., & Taniguchi, K. 2016, Phys. Rev. D, 93, 124046
Siegel, D. M. 2019, Eur. Phys. J. A, 55, 203
Siegel, D. M., & Metzger, B. D. 2017, Phys. Rev. Lett., 119, 231102
Siegel, D. M., & Metzger, B. D. 2018, ApJ, 858, 52
Siegel, D. M., Barnes, J., & Metzger, B. D. 2019, Nature, 569, 241
Sneden, C., Cowan, J. J., & Gallino, R. 2008, ARA&A, 46, 241
Spiegelhalter, D. 2019, The Art of Statistics (Milton Keynes: Penguin Random House)
Suda, T., Katsuta, Y., Yamada, S., et al. 2008, PASP, 60, 1159
Suess, H. E., & Urey, H. C. 1956, Rev. Mod. Phys., 28, 53
Takahashi, K., Witti, J., & Janka, H.-T. 1994, A&A, 286, 857
Tamhane, A., & Dunlop, D. 2000, Statistics and Data Analysis (Upper Saddle River: Prentice-Hall)
Tauris, T. M., Kramer, M., Freire, P. C. C., et al. 2017, ApJ, 846, 170
Thielemann, F. K., Nomoto, K., & Yokoi, K. 1986, A&A, 158, 17
Thielemann, F.-K., Arcones, A., Käppeli, R., et al. 2011, Prog. Part. Nucl. Phys., 66, 346

Thielemann, F.-K., Eichler, M., Panov, I. V., & Wehmeyer, B. 2017, Annu. Rev. Nucl. Part. Sci., 67, 253
Thielemann, F.-K. Farouqi, K., Rosswog, S., & Kratz, K.-L. 2022, Eur. Phys. J. Web Conf., 260, 09002
Timmes, F. X., Woosley, S. E., & Weaver, T. A. 1995, ApJS, 98, 617
Ting, Y.-S., Freeman, K. C., Kobayashi, C., De Silva, G. M., & Bland-Hawthorn, J. 2012, MNRAS, 421, 1231
Travaglio, C., Gallino, R., Arnone, E., et al. 2004, ApJ, 601, 864
Tsujimoto, T., & Nishimura, N. 2018, ApJ, 863, L27
van de Voort, F., Pakmor, R., Grand, R. J. J., et al. 2020, MNRAS, 494, 4867
van de Voort, F., Pakmor, R., Bieri, R., et al. 2022, MNRAS, 512, 5258
Villar, V. A., Guillochon, J., Berger, E., et al. 2017, ApJ, 851, L21
Vlasov, A. D., Metzger, B. D., Lippuner, J., Roberts, L. F., & Thompson, T. A. 2017, MNRAS, 468, 1522
Wallner, A., Faestermann, T., Feige, J., et al. 2015, Nat. Commun., 6, 5956
Wanajo, S. 2013, ApJ, 770, L22
Wanajo, S., Janka, H.-T., & Müller, B. 2011, ApJ, 726, L15
Wanajo, S., Sekiguchi, Y., Nishimura, N., et al. 2014, ApJ, 789, L39
Wanajo, S., Müller, B., Janka, H.-T., & Heger, A. 2018, ApJ, 852, 40
Watson, D., Hansen, C. J., Selsing, J., et al. 2019, Nature, 574, 497
Wehmeyer, B., Pignatari, M., & Thielemann, F.-K. 2015, MNRAS, 452, 1970
Wehmeyer, B., Fröhlich, C., Côté, B., Pignatari, M., & Thielemann, F. K. 2019, MNRAS, 487, 1745
Winteler, C., Käppeli, R., Perego, A., et al. 2012, ApJ, 750, L22
Woosley, S. E. 1993, ApJ, 405, 273
Woosley, S. E., Wilson, J. R., Mathews, G. J., Hoffman, R. D., & Meyer, B. S. 1994, ApJ, 433, 229
Wu, M.-R., Fischer, T., Huther, L., Martínez-Pinedo, G., & Qian, Y.-Z. 2014, Phys. Rev. D, 89, 061303
Wu, M.-R., Fernández, R., Martínez-Pinedo, G., & Metzger, B. D. 2016, MNRAS, 463, 2323
Wu, M.-R., Barnes, J., Martínez-Pinedo, G., & Metzger, B. D. 2019, Phys. Rev. Lett., 122, 062701
Ye, L. S., Fong, W.-F., Kremer, K., et al. 2020, ApJ, 888, L10
Yong, D., Kobayashi, C., Da Costa, G. S., et al. 2021, Nature, 595, 223
Zhu, Y., Wollaeger, R. T., Vassh, N., et al. 2018, ApJ, 863, L23

Appendix A: The Pearson and Spearman correlation coefficients

We summarize here briefly concepts that we are applying frequently throughout this paper. None of these concepts are our original work, for more information we refer to statistics text books (Tamhane & Dunlop 2000; Spiegelhalter 2019).

A.1. Pearson product moment correlation

Assume that we have two random variables X and Y that can have discrete values $\{x_i\}$ and $\{y_j\}$. If the value x_i is found with probability p_i, the expectation value is

$$\mu_X \equiv \sum_i p_i x_i \equiv E(X). \tag{A.1}$$

The fluctuations around the mean value are characterized by the variance

$$\sigma_X^2 \equiv \sum_i p_i (x_i - \mu_X)^2 \equiv VAR(X). \tag{A.2}$$

Obviously, $VAR(X)$ carries the dimension of X^2 and it may be more convenient to deal with a quantity of the same dimension as X which leads to the standard deviation

$$\sigma_X = \sqrt{\sum_i p_i (x_i - \mu_X)^2}. \tag{A.3}$$

The notion of variance can straight forwardly be generalized to the covariance of two variables X and Y

$$\sigma_{XY} \equiv \sum_i p_{XY,i}\ (x_i - \mu_X)(y_i - \mu_Y) \equiv \mathrm{COV(X, Y)}, \tag{A.4}$$

where $p_{XY,i}$ is the probability that x_i and y_i occur together. A positive value indicates the tendency of one variable to increase when the other variable does so, a negative value indicates that one variable decreases when the other increases, therefore the name co-variance. Obviously, $VAR(X) = COV(X, X)$. From its definition, Eq. (A.4), one can straight forwardly show that

$$COV(X, Y) = E(XY) - \mu_X \mu_Y \tag{A.5}$$

and this implies that the covariance vanishes for independent variables, that is for the case that $E(XY) = E(X)E(Y)$. Since the covariance vanishes when the variables are independent of each other, it obviously describes how they are correlated. The dimension of $COV(X, Y)$ is the same as the one of XY and one may prefer to work with a dimensionless quantity. One can straightforwardly obtain a dimensionless version of the covariance by normalizing it with σ_X and σ_Y

$$\begin{aligned} \mathcal{P}_{XY} &\equiv \frac{COV(X, Y)}{\sigma_X\ \sigma_Y} = \frac{\sigma_{XY}}{\sigma_X\ \sigma_Y} \\ &= \frac{\sum_i p_i (x_i - \mu_X)(y_i - \mu_Y)}{\sqrt{\sum_j p_j (x_j - \mu_X)^2}\ \sqrt{\sum_k p_k (y_k - \mu_Y)^2}}, \end{aligned} \tag{A.6}$$

which, for the case of equal probabilities, becomes the *Pearson correlation coefficient* (PCC)

$$r_{XY} \equiv \frac{\sum_i (x_i - \mu_X)(y_i - \mu_Y)}{\sqrt{\sum_j (x_j - \mu_X)^2}\ \sqrt{\sum_k (y_k - \mu_Y)^2}}. \tag{A.7}$$

Table A.1. Guidelines for interpreting the Pearson Correlation Coefficient r.

Strength of Association	PCC
Very weak	$0.0 \leq \lvert r\rvert < 0.2$
Weak	$0.2 \leq \lvert r\rvert < 0.4$
Moderate	$0.4 \leq \lvert r\rvert < 0.6$
Strong	$0.6 \leq \lvert r\rvert < 0.8$
Very strong	$0.8 \leq \lvert r\rvert \leq 1.0$

Apart from de-dimensionalizing the covariance, the division by $\sigma_X\ \sigma_Y$ in Eq. (A.6) has the additional consequence of restricting the range of the Pearson correlation coefficient to values $-1 \leq r \leq 1$.

Some commonly used guidelines for the interpretation of numerical values of r_{XY} are summarized in Table A.1. It is worth stressing under which conditions the PCC should be applied: a) the data sets should approximate normal distributions, b) the errors should be similar for different values of the independent variable (so-called homoscedascity), c) the data should be related linearly and d) it should be continuous within the considered interval and e) no outliers should be present in the data set. In general, a data point that is more than ± 3.29 standard deviations away, is considered an outlier. Scatter plots are a reasonable first step to inspect how well the assumptions are fulfilled.

A.2. Linear regression and the coefficient of determination

There is a close relation to linear regression, that is to fit the data by a straight line, $\tilde{y}(x) = ax + b$, that is optimal in a least squares sense. If one adopts as the error measure

$$\chi^2 \equiv \sum_i e_i^2 = \sum_i \left[y_i - \tilde{y}(x_i)\right]^2, \tag{A.8}$$

where the e_i are the residuals between the data, y_i, and the linear model values $\tilde{y}(x_i)$, and minimizes it with respect to a and b, $\partial\chi^2/\partial a = 0 = \partial\chi^2/\partial b$, one finds

$$a = \frac{COV(X, Y)}{VAR(X)} \quad \text{and} \quad b = \mu_y - a\mu_x, \tag{A.9}$$

that is the least squares estimators are simple functions of the means, variances and covariances. Straight forward algebra shows that the slope can also be expressed in terms of the Pearson correlation coefficient r_{XY} as

$$a = r_{XY} \sqrt{\frac{VAR(Y)}{VAR(X)}}, \tag{A.10}$$

which leads to the interpretation of the square of the correlation coefficient. If one uses the properties of the variance and covariance, one finds that the variance of the deviation of the linear model from the data is

$$\begin{aligned} VAR(e) &= VAR(y - (ax + b)) = (1 - r_{XY}^2) VAR(Y) \\ &= VAR(Y) - r_{XY}^2 VAR(Y), \end{aligned} \tag{A.11}$$

or, turned around, we have

$$r_{XY}^2 = 1 - \frac{VAR(e)}{VAR(Y)}. \tag{A.12}$$

In other words, the square of the Pearson correlation coefficient measures which proportion of the total variance of Y can be explained by the linear regression. The quantity r_{XY}^2 is often called the coefficient of determination. For a correlation coefficient of $r_{XY} = \pm 1$, the variance of the residuals vanishes. That is the linear model is a perfect fit to the data.

A.3. Spearman rank-order correlation

At the end of section A1 we had summarized the conditions under which Pearson's correlation coefficient should be applied. If one of the conditions should be violated, in particular if the relation is nonlinear, one can still apply the Spearman rank correlation coefficient (SCC). The idea is to rank the variables (i.e., sort them according to size and assign them the integer of their position in the sorted list; use (noninteger) averages in the case of ties) and apply Pearson's formula, Eq. (A.7), to the ranks $\mathcal{R}(x_i)$ and $\mathcal{R}(y_i)$ (rather than the data values)

$$\rho_{XY} \equiv \frac{\sum_i (\mathcal{R}(x_i) - \mu_{\mathcal{R}(X)})(\mathcal{R}(y_i) - \mu_{\mathcal{R}(Y)})}{\sqrt{\sum_j (\mathcal{R}(x_j) - \mu_{\mathcal{R}(X)})^2}\,\sqrt{\sum_k (\mathcal{R}(y_k) - \mu_{\mathcal{R}(Y)})^2}}. \tag{A.13}$$

For a perfectly monotonic relation one obtains a value of +1 (highest value of X is associated with highest value of Y etc. down to lowest values) or -1 (highest X-value associated with lowest Y-value etc.). If high X values are not preferentially related to high (or low) Y-values and instead the ranks are not correlated, the contributions approximately cancel and one obtains a value $\rho_{XY} \approx 0$. If $\mathcal{R}(x_i)$ and $\mathcal{R}(y_i)$ are integers, the Spearman rank correlation can also conveniently be expressed as

$$\rho_{XY} = 1 - \frac{6 \sum_{i=1}^{N} [\mathcal{R}(x_i) - \mathcal{R}(x_i)]^2}{N(N^2 - 1)}. \tag{A.14}$$

Apart from requiring fewer assumptions, the major difference to the PCC is that the SCC measures the strength of a monotonic association while the PCC measures the strength of a linear association.

Appendix B: Relationship between a variable and its rank

We can order continuous variables according to either rising or decreasing values. If we list them in such an ordered sequence and define the integer number in the list as its rank, this variable can be plotted as a function of its rank. If one throws a dice for a sufficient number of times (i.e., sufficient statistics), one will find all numbers from one to six resulting for an equal amount of times, and plotted as a function of their ranks, a step function will result (in this case of an integer random variable). Switching over to a random number generator for continuous variables, a linear relationship results between the variable and its rank, which is identical with the averaged straight line through the step function for an integer variable.

In an astrophysical environment of stars being formed from the local interstellar medium (ISM), the pollution with a single element X from an (explosive) astrophysical site depends on the question how much the ejecta of this event were mixed into the gas cloud from which the star was formed. We can think of the extreme case of no pollution in the early galaxy if no such nearby event took place, yet, and otherwise of a strong pollution, if the proto-stellar cloud was fully mixed with the ejecta of such an event. The amount of the contribution of element X from one type of event can thus be represented by a random number generator from zero to a maximum, which would be observed as a linear relation between abundance and the related rank. Therefore, a linear relationship between an abundance X and its rank is expected if one type of an astrophysical source contributes.

If another astrophysical source contributes to the same element X, this can be represented by a random number generator as well for the amount of element X mixed into the protostellar cloud by this second type of event. If we add these contributions for each random event of type A and type B, we can - for the extremes - have cases from negligible contributions of both types of events to maximum contributions from both types of events, and in general also many cases with varying and different contributions from each event type. When ordering these summed abundances according to their ranks, a different pattern appears, and the linear relationship between the values and their ranks is destroyed. We show this behavior in Fig. B.1 with two random variables X and Y, where X is generated by only one and $Y = X_1 + X_2$ by two random number generators.

As discussed above, the relationship between X and its rank is perfectly linear, whereas Y, a superposition of two random variables does not show this linearity. In the case displayed in Fig. B.1 both variables lie in the interval [0,1], if the variables in the superposition are of different size (or even a further source is added), a deviation from a straight line will remain, but it can experience further distortions.

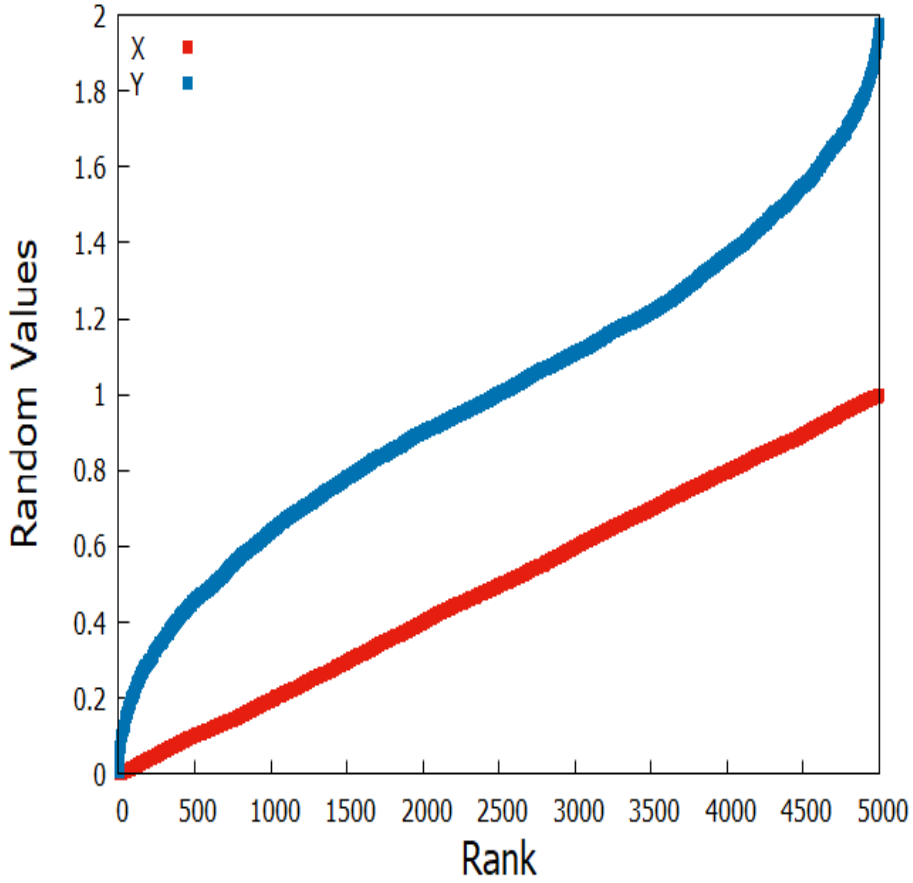

Fig. B.1. Linear value-rank-trend as a fingerprint of a single astrophysical source. Randomly generated variables X and Y. X is generated by a single random generator in the interval [0,1] and $Y = X_1 + X_2$ by two random generators. Rank 1 indicates the smallest abundance in the whole data. We see an overall nonlinear behavior for Y.

Appendix C: Cluster analysis

Cluster analysis, or clustering for short, is a method of unsupervised learning where the aim is to identify patterns in data without any predetermination. It is frequently used for statistical data analysis in a variety of fields (see e.g., Everitt et al. 2011). It allows one to identify groups of similar objects (clusters) that are more related to each other than to objects in other groups. Clustering algorithms can also provide valuable insights for the interpretation of our data by identifying groups in our data points.

Several dozens of clustering algorithms have been published, they can generally be divided into the following categories:

- connectivity-based clustering: it is based on the idea of objects (with their parameters) being more related to objects with similar or close-by parameter values than to objects with more different parameter sets.
- centroid-based clustering: a central vector represents the average properties of the whole cluster, which is with its parameters not necessarily identical to a single member of the data set.
- distribution-based clustering: clusters can be defined as objects belonging most likely to the same distribution.
- density-based clustering: clusters are defined as areas of higher density in the data space than surrounding regions of the data set.
- grid-based clustering: it is used for multidimensional data set.

In this paper we used the probably best-known clustering algorithm, k-means, which is centroid-based. It has the advantage that it is algorithmically simple and computationally fast. k-means is often referred to as Lloyd's algorithm and it contains three basic steps. One begins by choosing a predefined number of initial guesses for the centroid positions and then iterates over the remaining two steps:

- assign each sample to its nearest centroid
- update the centroid positions based on the mean value of the samples assigned to the previous centroid

until convergence. The procedure is considered converged once the distances between two subsequent updates drop below a predefined tolerance, that is once the centroid positions have stopped moving. k-means has the advantage of being computationally efficient, as all necessary steps consist of computing the distances between points and group centers. But it has the disadvantage that one needs to preselect the number of cluster divisions in the data beforehand. This is not always trivial as ideally a clustering algorithm should also provide the appropriate number of clusters in order to gain insight from the dataset.

Appendix D: The difference between the alpha and r-process elements in the early galactic evolution

As mentioned before, in early galactic evolution Fe is dominantly made in regular core-collapse supernovae that coproduce all alpha elements such as O, Ne, Mg, Si, S, Ar, Ca, Ti as well. While, dependent on the initial stellar mass, the yields of alpha-elements differ to some extend (especially for those originating largely in outer zones related to hydrostatic burning phases, such as O, Ne, Mg), these variations are limited, and the alpha/Fe ratio is very similar in all core-collapse supernova ejecta. As pointed out earlier in section 2.1, values of [Fe/H]=-2.7 will result in a supernova remnant when polluting typically the ISM of about 7×10^4 $M_\odot$. This points to the fact that at very low metallicities the surface abundance of stars, which reflect the composition in the pre-stellar cloud, can have been affected by the pollution of a single event. The maximum [Fe/H] for such interpretation is given by this limit. But as also already pointed out in section 2.1, it is highly possible that a pre-stellar cloud consists not entirely of the gas of a single remnant, one could have just a 10, 1, or even 0.1% pollution of a nearby supernova, leading then to [Fe/H] values of -4, -5, or even -6 (as observed). Thus, observations in this metallicity range up to about [Fe/H]=-2.5 can be interpreted either (a) as contributions mixed in by one single supernova with [Fe/H] varying dependent of the pollution percentage (with supernova-related coproduction of other ejected elements) or (b) a superposition of the imprint of several supernovae, adding up to that total metallicity. As long as the contributions come only from a single or several single-type of event(s), which always eject an abundance pattern with (close to) similar element ratios, one will find close to constant element ratios in these low metallicity stars. This will be underlined by a high correlation of two coproduced elements (a correlation of 1 stands for a constant ratio of two abundances in all the stars considered) and clearly indicates the coproduction in this one type of events, contributing to the observed star(s). For all alpha-elements this is the case, resulting in a high correlation of alpha versus Fe. While one will find initially also a slight scatter because supernovae with different progenitor masses lead to different alpha/Fe ratios (with Mg being a typical alpha element), the final averaged behavior consists only of the statistical average of one single class of nucleosynthesis events. Thus, one finds, as long as no other events, such as type Ia supernovae, contribute for [Fe/H]<-1, an almost identical behavior for [alpha/Fe] with a slightly increasing scatter toward lower metallicities, but with overall the same average ratio. This dependence of [alpha/Fe] versus [Fe/H] can be mirrored with [alpha/H] bersus [Fe/H], for instance as an example [Mg/H] versus [Fe/H], showing an increasing linear relation rather than a constant as in [alpha/Fe] versus [Fe/H].

The question of how this is different for r-process elements and their relation to Fe, is well justified and needs to be addressed. As mentioned above, Fe originates from regular core-collapse supernovae and (as we concluded in section 3) from specific supernovae which coproduce Fe and Eu in a weak r-process (our categories I and II). Core-collapse supernovae occur with a high event rate and specific supernova events, such as magneto-rotational supernovae (which coproduce a weak r-process), probably with an event rate reduced by a factor of about 10 (therefore still relatively high). Both aspects lead to a continuous enrichment in Fe. On the other hand, the rare events of category III (a and b, i.e., compact binary mergers and collapsars or hypernovae) produce no (or in comparison to solar ratios) negligible amounts of Fe, but large amounts of r-process elements (especially also strong r-process elements up to the third abundance peak as well as actinides). As discussed in sections 6.3.1 and 6.3.2, for the Eu ejecta in categories II, IIIa and IIIb this relates to a stepwise increase by about a factor of 10 between these three cases (different from Mg in regular CCSNe with similar Mg ejecta and a similar Mg/Fe ratio). These events add their r-process ejecta (such as Eu) on a floor of the frequent Fe contributions by regular core-collapse supernovae (and also the special supernovae coproducing Fe). Figure 26 (bottom left) shows how such events start to make their imprint in a sequence according to their event rate from [Fe/H]≈-4 to about -3.5 in limited-r, r-I, and r-II stars. r-I and r-II stars (with [Eu/Fe]>0-0.3 and their r-process contributions being dominated by category III (a and b) events, with no or negligible Fe coproduction) show no correlation between Eu and Fe as seen in Fig. 3. Contrary to that, limited-r stars (dominated by category I and II events with Fe and Eu coproduction) show a correlation between Fe and Eu. These contributions from regular core-collapse supernovae and special supernovae explain limited-r stars, leading during the evolving [Fe/H] in a [Eu/H] versus [Fe/H] evolution with a small scatter (see the magenta dots for limited-r stars in Fig. 26 in the lower left panel). The rarer categories III (a and b) of strong r-process events enter at slightly higher metallicity (see the green and light blue dots in the lower left panel), responsible for r-I and r-II stars. They form two separate regimes, which show, as additional effects, much smaller Sr/Eu ratios than limited-r stars and the highest Th/Eu for r-II stars (see also Fig. 26). Once there exist enough events to average over all these categories for [Fe/H]>-2, a merged average behavior develops, which is not identical with the continuation of any of the three regimes but results from an average of all these inputs with their statistical weights. While r-I and r-II stars might amount to a small percentage of all stars containing r-process elements, they contain r-process matter up to a factor of 100 higher than limited-r stars. Therefore, they are nevertheless, the dominant source for the solar r-process contribution, while, however, the weak r-process sources might still contribute 20% to Eu (see our table 7), and, when considering uncertainties, even somewhat higher contributions. The amount of ejecta multiplied with the frequency of events is what counts here. Our statistical analysis of observational data for low-metallicity stars, up to section 5, provided the motivation for this framework and the basis to apply this scheme with existing model predictions of ejecta compositions for the different suggested category sites in section 6. This led to a consistent picture as shown in tables 9 and 10. Category II events (magneto-rotational supernovae) make up about 10% of all core-collapse supernovae, and category III (a and b) events (neutron star mergers and collapsars) about six per mil of all core-collapse supernovae (a full proof for the existence of the highly equation of state dependent category I, quark-deconfinement supernovae, is still missing). This consistency between present-day model predictions for different r-process sites and observations, based on the statistical analysis of the abundances of low-metallicity stars, confirms an emerging picture how the early chemical evolution of r-process elements in galaxies can be explained.